Doctoral Dissertation
博士論文

Photoelectron–ion correlation created by photoionization of H_2 and correlated molecule–photon dynamics in a cavity
(H_2の光イオン化によって生成する
光電子–イオン相関と
共振器中の分子–光子の相関動力学)

Department of Chemistry, Graduate School of Science,
The University of Tokyo
東京大学大学院理学系研究科化学専攻

Takanori Nishi

西　孝哲

Abstract

Quantum mechanics forbids us to describe a particle, once it correlates with another, as an individual physical object whose complete set of properties can be solely determined. Such correlations play one of the most important roles in understanding quantum phenomena such as non-adiabatic transitions in molecular dissociation, quantum teleportation, and Bose–Einstein condensate.

This dissertation theoretically explores several phenomena to reveal the role of quantum correlations in molecular systems. Specifically, it studies the photoionization of H_2 and unambiguously evaluates the correlation between the photoelectron and H_2^+ in terms of entanglement between the two particles. The correlation among the vibrational states of H_2^+ is evaluated in terms of coherence and the relation with entanglement is studied. The ultrafast vibrational motion of H_2^+ and its dependence on the photoelectron is analysed and the origin of this correlation is ascribed to the non-locality of the wave function. Moreover, the experimental scheme to extract the correlation effect from the vibrational motion of H_2^+ using the sequence of ultrashort laser pulses is proposed. The correlation between a molecule and photons in a plasmonic nanocavity is also studied. This system has been attracting attention due to its potential use in quantum information and in the control of chemical reactions, and the analytical and numerical methods for describing the molecular dynamics in such a system are formulated.

Acknowledgments

I would like to express my gratitude to my primary supervisor Professor Kaoru Yamanouchi and co-supervisor Professor Erik Lötstedt for their support. I am grateful to Professor Yamanouchi for giving me invaluable comments and advice during our scientific discussions, teaching me the way to present scientific contents to broad audiences, encouraging me to attend various conferences, and giving me an opportunity to study at Aarhus University. I owe my deepest gratitude to Erik, who taught me the theoretical treatment of molecular dynamics interacting with ultrafast and intense laser pulses, helped me whenever I got stuck on the numerical calculation and the physical interpretation, and gave insightful suggestions during our discussions. I also would like to thank Professor Tsuyoshi Kato for his perceptive comments and discussions and informing me of papers relevant to my work. I would like to thank everyone at the Yamanouchi Laboratory.

I acknowledge Dr. Toshihiko Sasaki (Photon Science Center, The University of Tokyo) for his valuable comments on the validity of the mapping from the indistinguishable picture to the distinguishable picture. For the study on the phase of the reduced density matrix, I acknowledge Dr. Yasuo Nabekawa (RIKEN) for providing his experimental data and for the comments on the experimental realizability of the pump–probe scheme to determine the phase. I would also like to express my gratitude to Professor Katsumi Midorikawa for his insightful discussion on this topic. For the study on a molecular polariton, I would like to express my deepest appreciation to Professor Klaus Mølmer (Aarhus University) and Professor Lars Bojer Madsen (Aarhus University) and to everyone at Aarhus University for their friendliness and hospitality. Finally, a special thanks goes to my parents for their support through my PhD life.

Publications

This thesis is based on the following papers:

  I. Takanori Nishi, Erik Lötstedt, and Kaoru Yamanouchi. Entanglement and coherence in photoionization of H_2 by an ultrashort XUV laser pulse. *Physical Review A*, 100(1):013421, jul 2019.

 II. Takanori Nishi, Erik Lötstedt, and Kaoru Yamanouchi. Time delay in the coherent vibrational motion of H_2^+ created by ionization of H_2. *Physical Review A (Rapid Communication)*, 102(5):051101, nov 2020.

The thesis also includes an unpublished work:

III. Takanori Nishi, Lars Bojer Madsen, and Klaus Mølmer. Effective operator method for a molecule in a plasmonic nanocavity. (in preparation)

Contents

Chapter 1

General introduction

In the first chapter, the background of the discussions in Chapter 2-4 is given. Fundamental formalism of bipartite entanglement is given in the first section based on Ref. [1], a short review on observation of coherent motion is given in the second section, and finally the molecule–cavity system is introduced and the theoretical method to describe such a system is explained.

1.1 Entanglement and coherence

1.1.1 Bipartite system

When a pair of particles is measured, the outcome of the measurement can be correlated, e.g., when a ball collides with the other at rest and consequently their momenta are measured, the measurement results p_1 and p_2 should correlate with each other so that they satisfy the conservation rule. If the initial momentum is prepared as P_j with a certain probability c_j so that $p_{1,j} \neq p_{1,k}$ and $p_{2,j} \neq p_{2,k}$ for $j \neq k$ are satisfied, the measurement of p_1 gives a concrete prediction for the measurement of p_2. In this case, the measurement of a ball does not affect the other because each ball has its own momentum regardless of whether it is measured or not.

Such "classical correlation" exists also in quantum mechanics. If we have a generator of a pair of particles, which prepares them, for simplicity, in the same state $|\psi_j\rangle$ but the probability distribution c_j is completely random, i.e., c_j is same for all j, the two-particle system can be expressed by a density matrix

$$\rho = \frac{1}{d} \sum_{j=1}^{d} |\psi_j \psi_j\rangle \langle \psi_j \psi_j| = \frac{1}{d} \sum_{j=1}^{d} |\psi_j\rangle_1 \otimes |\psi_j\rangle_2 \langle \psi_j|_1 \otimes \langle \psi_j|_2$$

$$= \frac{1}{d} \sum_{j=1}^{d} |\psi_j\rangle_1 \langle \psi_j|_1 \otimes |\psi_j\rangle_2 \langle \psi_j|_2 , \tag{1.1}$$

where $\{|\psi_j\rangle , \, j \in [1, d]\}$ is a complete orthonormal basis set and the ket (bra) on the left of $\otimes$ corresponds to the first subsystem while the one on the right to the second. If a projective measurement on the first subsystem yields k, the total system becomes

$$\frac{\Pi_{1,k} \rho \Pi_{1,k}}{\mathrm{Tr}[\rho \Pi_{1,k}]} = \frac{1}{1/d} |\psi_k\rangle_1 \langle \psi_k|_1 \left\{ \frac{1}{d} \sum_{j=1}^{d} |\psi_j\rangle_1 \langle \psi_j|_1 \otimes |\psi_j\rangle_2 \langle \psi_j|_2 \right\} |\psi_k\rangle_1 \langle \psi_k|_1$$

$$= |\psi_k\rangle_1 \langle \psi_k|_1 \otimes |\psi_k\rangle_2 \langle \psi_k|_2 , \tag{1.2}$$

where $\Pi_{1,k} = |\psi_k\rangle_1 \langle \psi_k|_1$, and therefore, the measurement on the second subsystem will also give k.

The difference between quantum and classical mechanics becomes clear when we perform the measurement using a new orthogonal basis, e.g., defined as

$$|\chi_m\rangle = \sum_{j=1}^{d} \langle \psi_j|\chi_m\rangle |\psi_j\rangle . \tag{1.3}$$

If the projection of the first subsystem on the new basis results in m, the total system becomes

$$\frac{\Pi'_{1,m} \rho \Pi'_{1,m}}{\mathrm{Tr}[\rho \Pi'_{1,m}]} = |\chi_m\rangle_1 \langle \chi_m|_1 \otimes \left\{ \sum_{j=1}^{d} |\langle \psi_j|\chi_m\rangle|^2 |\psi_j\rangle_2 \langle \psi_j|_2 \right\} , \tag{1.4}$$

the second subsystem is still in a mixed state unlike Eq. (1.2). On the other hand, when the total system is a pure state $\rho = |\Psi\rangle \langle \Psi|$, where the state vector is

$$|\Psi\rangle = \frac{1}{\sqrt{d}} \sum_{j=1}^{d} |\psi_j\rangle_1 \otimes |\psi_j\rangle_2, \tag{1.5}$$

and if the projection of the first subsystem on the $|\psi\rangle$ basis gives k, the total system becomes

$$\frac{\Pi_{1,k}\rho\Pi_{1,k}}{\mathrm{Tr}[\rho\Pi_{1,k}]} = |\psi_k\rangle_1 \langle\psi_k|_1 \otimes |\psi_k\rangle_2 \langle\psi_k|_2, \tag{1.6}$$

while if the projection on the $|\chi\rangle$ basis gives m, the total system becomes

$$\frac{\Pi'_{1,m}\rho\Pi'_{1,m}}{\mathrm{Tr}[\rho\Pi'_{1,m}]} = |\chi_m\rangle_1 \langle\chi_m|_1 \otimes \sum_{j=1}^{d} \langle\chi_m|\psi_j\rangle |\psi_j\rangle_2 \sum_{j'=1}^{d} \langle\psi_{j'}|\chi_m\rangle \langle\psi_{j'}|_2$$

$$\equiv |\chi_m\rangle_1 \langle\chi_m|_1 \otimes |\tilde{\chi}_m\rangle_2 \langle\tilde{\chi}_m|_2. \tag{1.7}$$

The significance here is the fact that $|\tilde{\chi}_m\rangle$ also constitutes a new orthonormal set

$$\langle\tilde{\chi}_n|\tilde{\chi}_m\rangle = \sum_{j,j'=1}^{d} \langle\psi_{j'}|\chi_n\rangle \langle\psi_{j'}|\psi_j\rangle \langle\chi_m|\psi_j\rangle$$

$$= \sum_{j=1}^{d} \langle\chi_m|\psi_j\rangle \langle\psi_j|\chi_n\rangle = \delta_{nm}. \tag{1.8}$$

Therefore, only by projecting the first subsystem on $|\chi_m\rangle$ basis, the result of the projection of the second subsystem on the $|\tilde{\chi}_m\rangle$ basis can be predicted. This is distinct from the classical correlation given by Eq. (1.4), where the projection on the new basis set is no more able to give a prediction for the measurement of the second subsystem.

1.1.2 Bipartite entanglement

As shown above, the one-to-one correspondence between two measurement results is not a unique nature of quantum mechanics but if such a correspondence exists regardless of the measurement basis, we can ascribe it to quantum correlation. Such quantum correlation between two or more subsystems is the manifestation of a quantum nature called entanglement. In order to unambiguously define entanglement in a bipartite system, we consider the reduced density matrices defined as

$$\rho_1 = \mathrm{Tr}_2[\rho], \ \rho_2 = \mathrm{Tr}_1[\rho], \tag{1.9}$$

where the partial trace is taken as

$$\mathrm{Tr}_1[\rho] = \sum_{j=1}^{d} \langle\psi_j|_1 \, \rho \, |\psi_j\rangle_1. \tag{1.10}$$

When the total system can be described by a product state

$$|\Phi\rangle = |\phi\rangle_1 \otimes |\chi\rangle_2, \tag{1.11}$$

the measurement on one subsystem has no effect on the other because each subsystem is completely described by its state vector and therefore, such a state should be regarded as non-entangled state and is called separable. The reduced density matrices for the separable state Eq. (1.11) can be written as

$$\rho_1 = |\phi\rangle_1 \langle\phi|_1, \ \rho_2 = |\chi\rangle_2 \langle\chi|_2, \tag{1.12}$$

and the density matrix of the total system can be decomposed into a product of the reduced density matrices as

$$\rho = \rho_1 \otimes \rho_2. \tag{1.13}$$

If we have a statistical mixture of separable states

$$\rho = \sum_j p_j \rho_{1,j} \otimes \rho_{2,j}, \tag{1.14}$$

the correlation between measurement results on two subsystems can be ascribed to the probabilities p_j like we have already seen for Eq. (1.1), and therefore, Eq. (1.14) is also regarded as separable.

On the other hand, the total system which cannot be written as a product state Eq. (1.11) or its statistical mixture Eq. (1.14) is called entangled. A general entangled state can be written as

$$|\Psi\rangle = \sum_{jk} c_{jk} |\psi_j\rangle_1 \otimes |\chi_k\rangle_2, \tag{1.15}$$

where $c_{jk} \neq c_j c_k$, otherwise it reduces to a product state. As we have seen for Eq. (1.5), the entangled state should have correlation between two subsystems in any basis set and therefore, it is unclear how to evaluate the amount of entanglement only from a specific basis set as in Eq. (1.15). Therefore, we should define a certain basis set, with which we can unambiguously evaluate the amount of entanglement. In the case of the pure bipartite system, such basis set can be defined by the Schmidt decomposition

$$|\Psi\rangle = \sum_{j=1}^{s} \sqrt{\lambda_j} |\tilde{\phi}_j\rangle_1 \otimes |\tilde{\chi}_j\rangle_2, \tag{1.16}$$

which contains only one summation index in contrast to Eq. (1.15). The Schmidt bases are the eigenstates of the reduced density matrices

$$\rho_1 = \sum_{j=1}^{s} \lambda_j |\tilde{\phi}_j\rangle_1 \langle\tilde{\phi}_j|_1, \ \rho_2 = \sum_{j=1}^{s} \lambda_j |\tilde{\chi}_j\rangle_2 \langle\tilde{\chi}_j|_2 \tag{1.17}$$

where their eigenvalues λ_j ($1 \geq \lambda_1 \geq \lambda_2 \geq \cdots \geq \lambda_s \geq 0$) are called the Schmidt coefficients and the number of terms in the summation, s, is called the Schmidt rank. Because

$\text{Tr}[\rho] = 1$ for any normalized state ρ, $\sum_j^s \lambda_j = 1$ always holds. If we have only one term in the Schmidt decomposition, i.e., $\lambda_1 = 1$, $\lambda_j = 0$ $(j \geq 2)$, the total system is separable. If $\lambda = 1 - \delta$ $(\delta \ll 1)$ and $\sum_{j=2}^s \lambda_j = \delta$, the total system is entangled but the amount entanglement is small because the measurement on one subsystem carries small amount of information about the other subsystem on average. Specifically, the measurement on the first subsystem most likely gives $|\tilde{\phi}_1\rangle_1$ but we obtain small amount of information from this result because we can expect the measurement on the second subsystem gives $|\tilde{\chi}_1\rangle_2$ even before the measurement. If the measurement on the first subsystem gives other results like $|\tilde{\phi}_2\rangle_1$, the measurement on the second subsystem will give $|\tilde{\chi}_2\rangle_2$, which is valuable information because, without the measurement on the first subsystem, we can hardly predict when the second subsystem results in $|\tilde{\chi}_2\rangle_2$. However, such events seldom occurs since $\lambda_2 \ll 1$. Therefore, the amount of correlation between two measurement results on average, i.e., entanglement, is small. From these examples, we can expect the entanglement increases as the number of λ_j non-negligibly contributing to the Schmidt decomposition increases. Actually, the maximally entangled state is written as

$$|\Psi\rangle = \frac{1}{\sqrt{N}} \sum_{j=1}^N |\tilde{\phi}_j\rangle_1 \otimes |\tilde{\chi}_j\rangle_2, \tag{1.18}$$

where $N = \min[d_1, d_2]$ is the smaller one of the dimensions of the Hilbert spaces $\mathcal{H}_{1,2}$ for the first and the second subsystems, $d_1 = \dim[\mathcal{H}_1]$ and $d_2 = \dim[\mathcal{H}_2]$, respectively. Namely, the maximally entangled state contains the pairs of Schmidt bases $|\tilde{\phi}_j\rangle_1 \otimes |\tilde{\chi}_j\rangle_2$ with the equal weight.

The purity of the reduced density matrix defined as

$$P = \text{Tr}_2[\rho_1^2] = \text{Tr}_1[\rho_2^2] = \sum_{j=1}^s \lambda_j^2, \tag{1.19}$$

is an unambiguous quantifier of entanglement. For the separable state $P = 1$ while for the maximally entangled state $P = \sum_j^N 1/N^2 = 1/N$. As entanglement of the total system increases, the subsystems become mixed more, i.e., P decreases.

1.1.3 Entanglement in atoms and molecules

In recent years, the interparticle correlation in atoms and molecules has been related to entanglement [1]. For example, the electron–proton correlation in a hydrogen atom in the ground state [2] as well as in one-photon [3] and strong-field ionization were characterized by using the entanglement between two particles. For molecular systems, the electron–nuclear correlation as well as the electron–electron correlation characterized by the entanglement can give a new insight into the molecular physics. For example, the electron–nuclear correlation in the stationary state has been well described using the Born–Oppenheimer (BO) approximation

$$\Psi(r, R) = \psi(r; R)\chi(R), \tag{1.20}$$

where $\psi(r; R)$ is the electronic wave function depending parametrically on the internuclear distance R and $\chi(R)$ is the nuclear wave function. Although Eq. (1.20) is written as a

product of two wave functions, it isn't separable because $\psi(r; R)$ is already an entangled state of the electronic and the nuclear coordinates. A separable state can be given by the crude BO approximation, i.e.,

$$\Psi_C(r, R) = \psi(r; R_0)\tilde{\chi}(R), \qquad (1.21)$$

where the internuclear distance specifying the electronic wave function is fixed at R_0. The entanglement expressed by the BO approximation corresponds to the amount of difference between Ψ and Ψ_C. In the vicinity of the avoided crossing, the electronic states cannot be described by a single wave function any more and the BO approximation becomes invalid. This break down of the approximation is often explained that the BO wave function underestimates the electron–nuclear correlation. Izmaylov *et al.* [4] showed, however, that the amount of entanglement and the validity of the BO approximation are not strictly correlated so that the BO approximation can be valid even when the entanglement is large while it can be invalid for an almost separable state.

In the case of photoionization of H_2, the final state described as

$$|\Psi\rangle = \sum_{vk} a_{vk} |\chi_v\rangle \otimes |\phi_k\rangle, \qquad (1.22)$$

where $|\chi_v\rangle$ and $|\phi_k\rangle$ are the vibrational eigenstate of H_2^+ and the energy eigenstate of the photoelectron, respectively, can be regarded as the bipartite entangled state. The reduced density matrix defined by Eq. (1.9) for H_2^+ is obtained as

$$\rho_{\text{vib}} = \text{Tr}_{\text{e}}[|\Psi\rangle \langle\Psi|] = \sum_{vv'} \sum_k a_{vk} a_{vk}^* |\chi_v\rangle \langle\chi_{v'}|. \qquad (1.23)$$
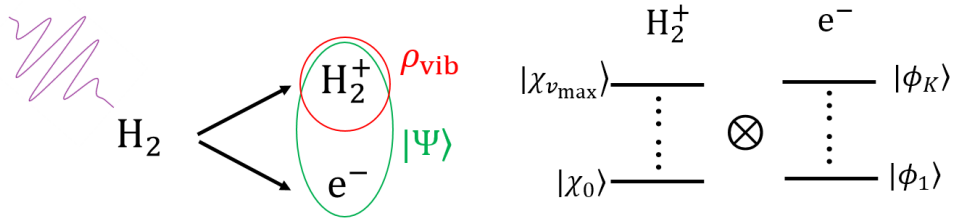

Figure 1.1: The entangled state generated by the photoionization of H_2. The Hilbert space for the total wave function $|\Psi\rangle$ is composed of the tensor product of Hilbert spaces for the subsystems as depicted in the right figure.

1.2 Ultrafast coherent motion

1.2.1 Coherent motion of ions

By attosecond time-resolved spectroscopy, we are able to characterize the coherent internal motion in an atomic or molecular ion created by photoionization [5, 6] as well as in a neutral atom or molecule [7–10]. Because the photoelectron and the ion are generally entangled, the ion should be described by the reduced density matrix ρ_{ion} by tracing out the photoelectron from the total density matrix as introduced in Eq. (1.9). The reduced density matrix has been determined by the measurements of transient absorption [5, 11, 12] and by the streaking of photoelectrons [13, 14]. For example, if the ionization occurs at $t = 0$ by the irradiation of the pump laser pulse, the reduced density matrix of a two-level ion is written as

$$\rho_{\mathrm{ion}}(t) = |\rho_{\mathrm{gg}}|^2 \, |\mathrm{g}\rangle \, \langle \mathrm{g}| + |\rho_{\mathrm{ee}}|^2 \, |\mathrm{e}\rangle \, \langle \mathrm{e}| + \rho_{\mathrm{ge}} e^{-\mathrm{i}\omega_{\mathrm{ge}}t} \, |\mathrm{g}\rangle \, \langle \mathrm{e}| + \rho_{\mathrm{eg}} e^{-\mathrm{i}\omega_{\mathrm{eg}}t} \, |\mathrm{e}\rangle \, \langle \mathrm{g}| \,, \qquad (1.24)$$

where the first two terms are the population of the ground and the excited states, respectively, and the remaining two terms are the coherence between the two states. When the ion is further irradiated with a probe laser pulse and the absorption spectra is recorded as a function of the pump–probe time delay, the oscillation of the absorption intensity at the frequency ω_{ge} can be seen as long as the coherence terms $|\rho_{\mathrm{ge}}|$ and $|\rho_{\mathrm{eg}}|$ are large enough. We call such time dependent dynamics ascribed to the oscillation of the coherence terms the coherent motion.

Considering the complex phase of the coherence in Eq. (1.24), the coherent motion can be shifted in time as

$$\rho_{\mathrm{ge}} e^{-\mathrm{i}\omega_{\mathrm{ge}}t} = |\rho_{\mathrm{ge}}| e^{-\mathrm{i}\omega_{\mathrm{ge}}(t-\tau_{\mathrm{ge}})}, \qquad (1.25)$$

$$\tau_{\mathrm{ge}} = \frac{\arg[\rho_{\mathrm{ge}}]}{\omega_{\mathrm{ge}}}. \qquad (1.26)$$

The origin of such time shift, which we call the time delay, has been ascribed to the property of the laser pulse. For example, Goulielmakis *et al.* [5] ionized Kr by a few-cycle intense near-IR (NIR) laser pulse and recorded the transient absorption spectra of Kr^+ using an attosecond XUV pulse, from which they derived experimentally the phase of the reduced density-matrix elements of Kr^+, $\arg[(\rho_{\mathrm{ion}})_{ij}]$, for the ith and jth levels and they ascribed the phase to the waveform of the NIR laser pulse. Here, we can consider a question, "can we completely explain the time delay in the coherent motion if we can precisely characterize the waveform of the laser pulse?", and the answer will be given in Chapter 3 by investigating the photoionization of H_2.

In characterizing the coherent vibrational motion of H_2^+ described by the reduced density matrix ρ_{vib}, we irradiate H_2^+ with a probe pulse so that it dissociates through the $2\mathrm{p}\sigma_{\mathrm{u}}$ potential energy surface and we measure the kinetic energy of H^+, called the kinetic energy release (KER). In thus obtained spectrogram called the delay–KER spectrogram, the signal intensity of H^+ oscillates as a function of the pump–probe time delay τ reflecting the time dependent factor of the coherence, $e^{-\mathrm{i}(\omega_v - \omega_{v'})\tau}$, where v and v' are the vibrational quantum numbers. An example of the delay–KER spectrogram is shown in Fig. 1.3. As shown in Chapter 3, the delay–KER spectrogram can be shifted in time due to the phase of $(\rho_{\mathrm{vib}})_{vv'}$, which originates from the photoelectron–ion correlation.
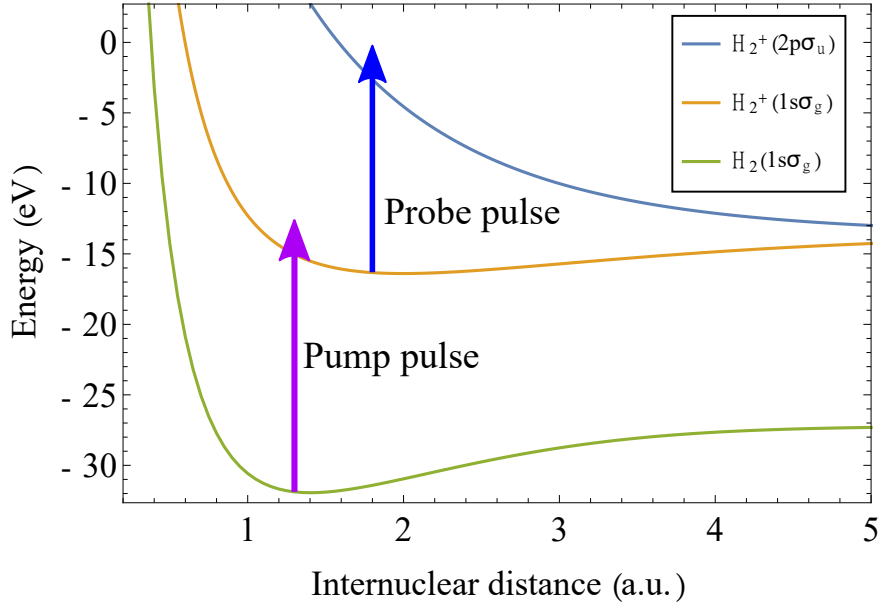
Figure 1.2: Potential energy curves relevant for the pump–probe scheme for H_2.
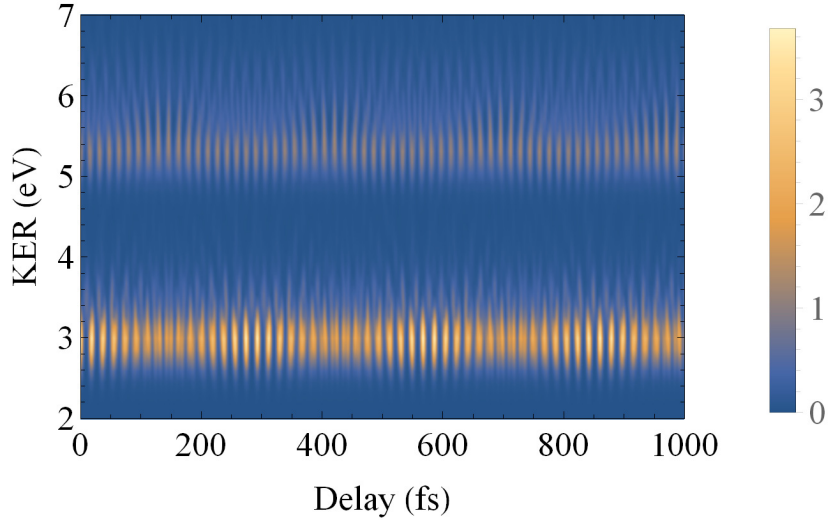
Figure 1.3: Simulated delay–KER spectrogram of H^+ produced through (i) the ionization of H_2 by an attosecond pulse train (APT) (ii) and the dissociation of H_2^+ by 3rd and 5th order harmonics of the APT. The mathematical expression for the spectrogram will be given by Eq. (3.16) in Chapter 3.

1.2.2   Wigner delay

On the other hand, the coherent motion of the photoelectron has been investigated in terms of the Wigner delay [15–18]. For simplicity, consider a separable state $|\Psi\rangle$ composed of an ionic state and the superposition of eigenstates of the momentum $\boldsymbol{k}_e$ of the photoelectron as

$$|\Psi\rangle = |\chi_{\mathrm{ion}}\rangle \otimes \int d\boldsymbol{k}_e a_{\boldsymbol{k}_e} |\psi_{\boldsymbol{k}_e}\rangle , \tag{1.27}$$

where $a_{\boldsymbol{k}_e}$ is the transition amplitude from the initial neutral state to the final state $|\Psi\rangle$. The Wigner delay [15, 16] is defined as the derivative of the phase of the transition amplitude $a_{\boldsymbol{k}_e}$ with respect to the energy of the photoelectron

$$\tau_W(\boldsymbol{k}_e) = \frac{d \arg[a_{\boldsymbol{k}_e}]}{d\omega_{k_e}}, \; \omega_{k_e} = \frac{k_e^2}{2}, \tag{1.28}$$

and can be interpreted as the group delay of the photoelectron wave packet escaping from the short-range potential created around the ion core [17]. Because the Wigner delay originates from the interaction between the photoelectron and the ion, it depends on the ionic state $|\chi_{\mathrm{ion}}\rangle$ of atoms and molecules. Indeed, by attosecond (as) streaking spectroscopy, it was revealed that the photoemission associated with the ionization of He [$\mathrm{He}^+(n=1) + \mathrm{e}^-$] is delayed by 12.6 as from the photoemission associated with the simultaneous excitation of the He^+ ion [$\mathrm{He}^+(n=2) + \mathrm{e}^-$] and that the photoemission delay can be ascribed to the difference in the Coulombic interaction in $\mathrm{He}^+(n=1)$ and that in $\mathrm{He}^+(n=2)$ [19]. For the dissociative ionization of H_2, by measuring the momentum of the proton combined with the measurement of the photoemission time delay, the Wigner delay was shown to vary depending on the internuclear distance of H_2^+ [20].

1.3 Molecule in a cavity

Recent experimental developments enable us to make nanoscale cavities [21–25] by placing a nanoparticle on metal surface, which confines the electromagnetic field in the gap between the nanoparticle and the metal surface. Moreover, by employing a host–guest chemistry, only a few or even a single molecule can be placed in the gap so that we can couple the cavity photon with a molecule [21]. When the molecule in an excited state is placed in the cavity, whose cavity mode is resonant to the decay of the excited state, the spontaneous emission can be enhanced, and therefore, the molecular dynamics in the excited state can be modified by the cavity. In order to simulate such a dissipative open quantum system, the master equation should be solved but its computational demand can be mitigated by employing a stochastic equation.
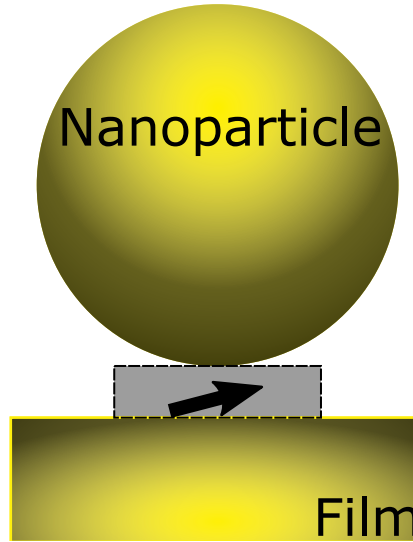
Figure 1.4: The schematic of the nanocavity realized in the gap between the nanoparticle and the metal surface. The arrow represents the transition dipole moment of the dye molecule. The dye molecule is placed in a cylindrical molecule (gray) whose height determines the gap between the nanoparticle and the film, i.e., the size of the nanocavity. In Ref. [21], the height was about 0.9 nm. The surface plasmon–polariton (SPP) is induced by shining the laser light to the nanoparticle, SPP is localized in the gap, and then the confined electromagnetic field interacts with the dye molecule.

1.3.1 Purcell effect

A quantum emitter placed in an optical cavity resonant to the transition frequency experiences the enhancement of spontaneous emission called the Purcell enhancement due to the increase of the density of states of the electromagnetic field. The Purcell factor P is the ratio of the spontaneous emission rate in the cavity to that in the vacuum and it is proportional to the cavity quality factor Q (a measure of photon storage time in the

cavity) and the inverse of the mode volume V as [26]

$$P \equiv \frac{\gamma_{\text{sp,cav}}}{\gamma_{\text{sp,vac}}} = \frac{3\lambda^3}{4\pi^2}\frac{Q}{V}, \tag{1.29}$$

where λ is the wavelength of the cavity mode. Because Q is related to the cavity decay rate γ_c as $Q = \omega_c/\gamma_c$ one can make it large by either reducing the loss of photons (i.e., making γ_c small and Q large) or reducing the cavity volume. In Ref. [21], even though the Q is as small as 15.9, it has been shown that the cavity volume achieves less than $40\,\text{nm}^3$ and the Purcell factor for a dye molecule is as high as 10^6.

1.3.2 Monte Carlo wave packet method

The open system interacting with the environment can be described by the master equation, e.g., an emitter having only one decay path can be described by

$$\dot{\rho} = -\mathrm{i}[H, \rho] - \frac{1}{2}\left(L^\dagger L\rho + \rho L^\dagger L\right) + L\rho L^\dagger, \quad L = \sqrt{\gamma}a, \tag{1.30}$$

where a is the annihilation operator, $\sqrt{\gamma}$ is the decay rate of the excited state, and L is called the Lindblad operator. The system is described by a density matrix ρ, the second and the third terms of the right hand side represent the relaxation process. In solving the master equation for the N dimensional system, the size of the memory for ρ scales as N^2 and consequently the computational cost increases more rapidly than the wave packet simulation.

The Monte Carlo wave packet method [27] is a useful method to reduce the computational cost in solving the master equation, in which the wave packet instead of the density matrix is used. First, the wave packet $|\psi\rangle$ is propagated under the non-Hermitian Hamiltonian $H_{\text{NH}} = H - \mathrm{i}L^\dagger L/2$ as

$$|\tilde{\psi}(t+dt)\rangle = e^{-\mathrm{i}H_{\text{NH}}dt}|\psi(t)\rangle \simeq (1 - \mathrm{i}dtH - \frac{dt}{2}L^\dagger L)|\psi(t)\rangle, \tag{1.31}$$

and then, the decrease of the norm is calculated as

$$dp = 1 - \langle\tilde{\psi}(t+dt)|\tilde{\psi}(t+dt)\rangle = dt\,\langle\psi(t)|L^\dagger L|\psi(t)\rangle. \tag{1.32}$$

Since $\langle\psi(t)|L^\dagger L|\psi(t)\rangle$ is the population of the decaying state, dp is the decay probability between t and $t+dt$. In order to mimic the randomness of the quantum jump, a random number ϵ $(0 \le \epsilon \le 1)$ is compared with dp at each time step and finally, the time evolution from t to $t+dt$ is completed by the following step

$$|\psi(t+dt)\rangle = \begin{cases} \frac{1}{\sqrt{1-dp}}|\tilde{\psi}(t+dt)\rangle, & \epsilon > dp \\ \frac{L}{\sqrt{dp/dt}}|\psi(t)\rangle, & \epsilon \le dp \end{cases}. \tag{1.33}$$

The time evolution of the wave packet $|\psi\rangle$ depends on the time series of the random number $\epsilon(t)$ and the wave packet obtained with the jth run of the calculation is called

the quantum trajectory denoted as $|\psi_j\rangle$. The wave packet calculation is repeated many times until the convergence is achieved for the averaged density matrix defined as

$$\rho = \sum_j |\psi_j\rangle \langle \psi_j| . \tag{1.34}$$

We can show that thus-obtained density matrix is equivalent to the solution of the master equation (1.30). Consider the time evolution from t to $t + dt$ for a given trajectory $|\psi(t)\rangle$. Because the probability of the relation $\epsilon > dp$ holds is $1 - dp$ while that for $\epsilon \leq dp$ is dp, the average of the density matrix at $t + dt$ can be obtained from the density matrix $\sigma(t) = |\psi(t)\rangle \langle \psi(t)|$ as

$$\bar{\sigma}(t + dt) = (1 - dp)\frac{1}{1 - dp} |\tilde{\psi}(t + dt)\rangle \langle \tilde{\psi}(t + dt)| + dp\frac{1}{dp/dt} L |\psi(t)\rangle \langle \psi(t)| L^\dagger$$

$$\simeq \sigma(t) - \mathrm{i}dt[H, \sigma(t)] - \frac{dt}{2}(L^\dagger L \sigma(t) + \sigma(t)L^\dagger L) + dt L \sigma(t) L^\dagger. \tag{1.35}$$

By averaging over different random issues for the trajectory $|\psi(t)\rangle$, $\sigma(t)$ becomes identical to $\rho(t)$ defined by Eq. (1.34) and consequently, the average of $\bar{\sigma}(t + dt)$ becomes identical to $\rho(t + dt)$. Therefore, the averaged density matrix Eq. (1.34) obeys the following

$$\frac{d\rho}{dt} = -\mathrm{i}[H, \rho] - \frac{1}{2}\left(L^\dagger L \rho + \rho L^\dagger L\right) + L\rho L^\dagger, \tag{1.36}$$

which is identical to the master equation (1.30).

1.4   This thesis

1.4.1   Entanglement and coherence

In Chapter 2, I present a work on the photoionization of a hydrogen molecule discussing entanglement between the ion and the photoelectron and the coherence in the ion, based on Ref. [28]. I theoretically investigate photoionization of an H_2 molecule, induced by the irradiation of an ultrashort extreme ultraviolet (XUV) laser pulse. I consider a system composed of a photoelectron ejected from H_2 and the resultant H_2^+ as a bipartite system. In order to clarify how the interparticle correlations among two electrons and two protons in H_2 are reflected to the bipartite system, I examine the entanglement between the photoelectron and the vibrational states of H_2^+ as well as the coherence in the vibrational states of H_2^+ by simulating the photoionization process of one-dimensional H_2. In the simulation, I solve a time-dependent Schrödinger equation using a symmetry-adapted grid method. On the basis of the simulations with ten different sets of three parameters characterizing an ultrashort XUV laser pulse, i.e., the pulse duration, the wavelength, and the peak intensity, we show that the extent of the entanglement depends sensitively on the coherence in the vibrational states of H_2^+.

1.4.2   Time delay in the coherent motion of H_2^+

In Chapter 3, I present a work on how the time delay in the coherent motion of H_2^+ created by photoionization of H_2 is ascribed to the correlation between H_2^+ and the photoelectron, based on Ref. [29]. The photoionization of H_2 by an attosecond pulse train is formulated using reduced density matrices, whose complex phase is related to the time delay in the coherent vibrational motion of H_2^+. The relation between the time delay in the vibrational motion and the Wigner delay of the photoelectron is also discussed. I show that, even when the ionization laser pulse is Fourier limited, the reduced density matrix of H_2^+ contains an intrinsic phase ascribed to the phase of the photoelectron wave function and that the intrinsic phase can be extracted by pump–probe measurements as long as the pump–probe time delay is measured with precision of the order of tens of attoseconds.

1.4.3   Molecule in a plasmonic nanocavity

In Chapter 4, I present an unpublished work on the simulation of molecular dynamics coupled to photons in a nanocavity. I derive the effective operators describing the slow dynamics of the molecule in the plasmonic nanocavity and give an analytical expression for the rate of photon emission by eliminating a fast-evolving state. We solve the master equation by the Monte Carlo wave packet (MCWP) method to examine the validity of the effective operators and reveal the relation between the rate of photon emission from the cavity and the vibrational motion of the molecule.

Chapter 2

Entanglement and coherence created by photoionization of H_2

Entanglement and coherence are the quantities characteristic to quantum mechanics and the former represents the correlation among some particles while the latter among the internal states within a single particle. Recent studies have adopted entanglement to quantify the amount of correlation and given better understandings of fundamental physics, for instance, steady state wave functions, validity of the adiabatic approximation, and dynamics of an atom under intense laser field.

On the other hand, coherence is related with a fundamental quantum phenomena, the superposition principle, which allows two or more states to exist at the same time, and the coherence quantifies how clearly we can see the superposition. Because the ionization results in an ejection of a photoelectron leaving an ion behind, two particles are spatially separated but still correlated. Such a distant correlation is the most striking difference between quantum and classical mechanics and so the ionization is well suited for studying quantum correlation. For the ionization of a hydrogen molecule I will show how the entanglement between two particles and the coherence in the molecular ion are related and how they can be controlled by changing the properties of the laser pulse.

2.1 Entanglement and coherence

2.1.1 Entanglement and coherence in atoms and molecules

Properties of atomic and molecular systems composed of particles such as electrons and nuclei are characterized by the correlations among the constituent particles. For example, the configuration interaction in quantum chemical calculations [30] and the correlation energy functional in the density functional theory [31] originate from the electron–electron correlation, and the nonadiabatic transitions among potential energy surfaces of molecules [32, 33] originate from the electron–nuclear correlation.

In recent years, the interparticle correlation in atoms and molecules has been related to entanglement [1], which was originally introduced by Schrödinger [34]. Especially, the entanglement in a bipartite system, which has been investigated intensively in quantum information science during the past three decades [35–39], is now being introduced into atomic and molecular science to explore the interparticle correlation.

Using entanglement, we can quantify the correlation between two degrees of freedom in a bipartite system. Indeed, the correlation between an electron and a proton in the ground state of a hydrogen atom was investigated in terms of entanglement [2] by the density matrix formalism developed in quantum information theory [40]. For a hydrogen atom, the entanglement in one-photon ionization [3] and that in strong-field ionization [41] were investigated. Entanglement was also used for characterizing the correlation in molecular systems. It was shown that the electron–electron correlation in an H_2 molecule, quantified using entanglement as a function of internuclear distance, exhibits a different behavior from the correlation energy, which is supposed to represent the extent of the electron–electron correlation [42, 43]. The correlation between the electronic and the vibrational degrees of freedom in molecules is also evaluated by using entanglement [4, 44, 45] The intramolecular vibrational energy redistribution in H_2O originating from the correlation between the vibrational modes was also discussed in terms of entanglement [46].

Coherence is another kind of quantum correlation used in describing correlation in atomic and molecular systems, which describes the amount of superposition. The recent development of subfemtosecond laser pulses has enabled us to create a highly coherent superposition of electronic states of rare gas atom ions [5]. For example, a method of controlling the coherence in two-level atomic ions created by ionization of Ne and Xe with an intense IR pulse was proposed theoretically [47] and such control of the coherence was demonstrated by transient absorption spectroscopy of Kr, which is ionized by an intense few-cycle near-IR pulse and probed by an XUV pulse whose duration is 150 as [5]. More recently, it was revealed theoretically that the extent of coherence in a two-level atomic ion can be enhanced when the bandwidth of the XUV pulse inducing photoionization becomes comparable with the energy separation between the two levels or when the XUV pulse is composed of two colors whose frequency difference is the same as the energy separation between the two levels of the atomic ion [48].

Considering that both of the two properties, i.e., entanglement and coherence, represent the correlation among the constituent particles of the system, it would be meaningful to clarify the difference between these two properties. The best system with which we could learn how entanglement and coherence are related to each other is a bipartite system because entanglement is a property of the total system while coherence is a property

of each of the subsystems. In a recent theoretical study on the excitation of Cs_2 by a sequence of chirped laser pulses, it was shown that the time evolution of the entanglement between the electronic part and the vibrational part of the vibronic wave packet can be characterized by the coherence in the electronic part [49, 50].

In this chapter, we investigate theoretically the photoionization of H_2 creating a bipartite system composed of an entangled pair of a photoelectron and an H_2^+ ion together with a coherent superposition of the vibrational states of H_2^+. We solve the time-dependent Schrödinger equation (TDSE) numerically for photoionization of H_2, and evaluate the degree of entanglement between a photoelectron and H_2^+ as well as the coherence in the vibrational states of H_2^+, and examine how the entanglement and the coherence describe the interparticle correlations in the system differently. We also show how the entanglement and the coherence vary depending on the laser parameters such as the wavelength, the peak intensity, and the pulse duration of the ionization laser pulse. Finally, we propose an experimental pump–probe scheme by which we can extract the entanglement and the coherence in photoionization of a molecular system. Throughout this chapter, atomic units (a.u.) are used unless otherwise indicated.

2.1.2 Entanglement between H_2^+ and e^-

We consider a system composed of a photoelectron and H_2^+ prepared in the electronic ground state, which are produced from one-dimensional H_2 in the electronic and vibrational ground state upon photoionization. We assume that two protons and two electrons move along the one-dimensional axis in response to a laser pulse whose polarization is along this axis. Then, as long as we assume that the electron spin state is singlet, a wave function of the composite system of $H_2^+ + e^-$ is written as

$$|\Psi\rangle = \sum_{hlk} c_{hlk} |\zeta_h\rangle \otimes \frac{1}{2} \mathcal{A} \left\{ |\eta_l, \alpha\rangle_1 \otimes |\phi_k, \beta\rangle_2 - |\eta_l, \beta\rangle_1 \otimes |\phi_k, \alpha\rangle_2 \right\}, \tag{2.1}$$

where $|\zeta_h\rangle$ is the basis for the nuclear vibration, $|\eta_l\rangle$ is the basis for the bound electron in H_2^+, $|\phi_k\rangle$ is the basis for the photoelectron interacting with the H_2^+ ionic core, α and β are the spin functions, and $\mathcal{A}$ is the antisymmetrizer of the spatial and the spin coordinates. The antisymmetrizer is defined using the identity operator I_{12} and the exchange operator E_{12} as $\mathcal{A} = I_{12} - E_{12}$, which exchanges the spatial and the spin coordinates of two electrons.

In general, when two distinguishable particles are described by a product state, $|\varphi\rangle_1 \otimes |\chi\rangle_2$, two particles are regarded as non-entangled, while they are regarded as entangled when no product state can be assigned to them. When the system is composed of indistinguishable particles, the same entanglement criteria used for distinguishable particles cannot be applied. Various entanglement criteria for the system of indistinguishable particles have been proposed [51–54], but these criteria have been developed for the system composed of one kind of indistinguishable particle, e.g. the system composed of electrons exclusively. In contrast, the system we treat is composed of two kinds of indistinguishable particles, i.e. two electrons and two protons. When the indistinguishable particles are spatially separated so that they can be measured separately, the indistinguishable particles can be treated as distinguishable particles [55] and the measure of entanglement, which has been developed in the investigation of distinguishable particles, can be applied.

The existence of the bijection between the indistinguishable-particle picture and the distinguishable-particle picture for both of bipartite fermions and bipartite bosons was proved in Refs. [55, 56]. We apply this bijection to the system of $H_2^+ + e^-$ because the photoelectron is spatially separated from the other electron contained in H_2^+. A generalized bijection between two pictures for multipartite systems including the effect of measurement setups was given in Ref. [57].

Because of the spatial separation of two electrons, we can introduce a localized wave packet, $|\phi_k\rangle$, representing an ejected photoelectron whose distance from the rest of the system, H_2^+, is sufficiently large so that they fulfill the orthogonality, $\langle \eta_l | \phi_k \rangle = 0$. Then, we define two projection operators

$$\mathcal{P}_1 = \sum_l |\eta_l\rangle_{1\,1} \langle \eta_l|, \quad \mathcal{Q}_2 = \sum_k |\phi_k\rangle_{2\,2} \langle \phi_k|, \tag{2.2}$$

and by using a map defined as

$$\sqrt{2}\mathcal{P}_1 \otimes \mathcal{Q}_2, \tag{2.3}$$

we can map $|\Psi\rangle$ onto the distinguishable-particle picture [56] as

$$\begin{aligned}
|\Phi\rangle &\equiv \sqrt{2}\mathcal{P}_1 \otimes \mathcal{Q}_2 |\Psi\rangle \\
&= \sum_{hlk} c_{hlk} |\zeta_h\rangle \otimes \frac{1}{\sqrt{2}} \left\{ |\eta_l, \alpha\rangle_1 \otimes |\phi_k, \beta\rangle_2 - |\eta_l, \beta\rangle_1 \otimes |\phi_k, \alpha\rangle_2 \right\}.
\end{aligned} \tag{2.4}$$

Then, we perform the basis transformation from the set of $\{|\zeta_h\rangle, |\eta_l\rangle\}$ to the vibrational eigenstate of H_2^+, $\{|\chi_v\rangle\}$, as

$$|\Phi\rangle = \sum_{vk} a_{vk} \frac{1}{2} \left\{ |\chi_v, \alpha\rangle_1 \otimes |\phi_k, \beta\rangle_2 - |\chi_v, \beta\rangle_1 \otimes |\phi_k, \alpha\rangle_2 \right\}, \tag{2.5}$$

where v is the vibrational quantum number. We note that $|\chi_v\rangle$ includes spatial part of the remaining electron. Now we can treat $|\Phi\rangle$ as a bipartite system composed of two distinguishable particles, a photoelectron and H_2^+.

Because we use the dipole approximation for the light–matter interaction, the spin state does not change during and after the light–matter interaction, and consequently, the spin entanglement is invariant. Therefore, in order to evaluate the laser parameter dependence of the entanglement, we only need the density matrix for the spatial part, which we can obtain by taking the trace over the spin coordinates, σ_1 and σ_2, as

$$\rho \equiv \mathrm{Tr}_{\sigma_1, \sigma_2} \left[|\Psi\rangle \langle \Psi| \right] = \sum_{vv', kk'} a_{vk} a_{v'k'}^* \left\{ |\chi_v\rangle \langle \chi_{v'}| \otimes |\phi_k\rangle \langle \phi_{k'}| \right\}. \tag{2.6}$$

Without loss of generality, we can neglect the spin part and concentrate on the spatial part of the state,

$$|\Phi_{\mathrm{S}}\rangle = \sum_{vk} a_{vk} |\chi_v\rangle \otimes |\phi_k\rangle, \tag{2.7}$$

because $|\Phi_S\rangle \langle \Phi_S|$ gives the same density matrix as Eq. (2.6). Therefore, we will use the spatial part $|\Phi_S\rangle$, instead of $|\Phi\rangle$ given by Eq. (2.5), in the following discussion.

The entanglement of the bipartite system can be evaluated by the reduced density matrix of either one of two subsystems. The reduced density matrix of the vibrational state of H_2^+ is obtained by taking the trace over the photoelectron coordinate as

$$\rho_{\text{vib}} = \text{Tr}_{\text{e}}[\rho] = \sum_{v,v'=0}^{v_{\max}} \sum_{k=1}^{k_{\max}} a_{vk} a_{v'k}^* \, |\chi_v\rangle \langle \chi_{v'}| , \tag{2.8}$$

and that for the spatial part of the photoelectron is obtained as

$$\rho_{\text{e}} = \text{Tr}_{\text{vib}}[\rho] = \sum_{k,k'=1}^{k_{\max}} \sum_{v=0}^{v_{\max}} a_{vk} a_{vk'}^* \, |\phi_k\rangle \langle \phi_{k'}| . \tag{2.9}$$

As a quantitative measure of the extent of entanglement [1, 58, 59], quantifiers such as purity [60], von Neumann entropy [61], and measurement-induced disturbance [62] have been proposed. Among these quantifiers, we choose purity of the reduced density matrix because it is directly related to the coherence of the subsystem as shown below. The purity P of ρ_{vib} is defined as the trace of ρ_{vib}^2,

$$P \equiv \text{Tr}(\rho_{\text{vib}}^2) = \sum_{v,v'=0}^{v_{\max}} \left| \sum_{k=1}^{k_{\max}} a_{vk} a_{v'k}^* \right|^2 . \tag{2.10}$$

When H_2^+ and e^- are non-entangled, $P = 1$ while it decreases as the extent of entanglement between H_2^+ and e^- increases, and the minimum of the purity $P_{\min}$ is equal to $P_{\min} = 1/N$, where $N = \min[v_{\max} + 1, k_{\max}]$. We take N as $N = v_{\max} + 1$ because the number of the vibrational states is much smaller than the number of the basis functions needed for expanding the spatial part of the photoelectron. The purity can also be calculated by the reduced density matrix of the spatial part of the photoelectron in the same manner as in Eq. (2.10) as

$$P = \text{Tr}(\rho_{\text{e}}^2). \tag{2.11}$$

Off-diagonal elements of the reduced density matrix are called the coherence while the diagonal elements are called the population. Equation (2.10) can be decomposed into two, that is, the first term defined as the sum of the squared modulus of the populations and the second term defined as the sum of the squared modulus of the coherences, as

$$P = \sum_{v=0}^{v_{\max}} |(\rho_{\text{vib}})_{vv}|^2 + \sum_{v \neq v'}^{v_{\max}} |(\rho_{\text{vib}})_{vv'}|^2 \equiv P_1 + P_2. \tag{2.12}$$

2.1.3 Coherence in the vibrational state

In order to evaluate the correlation between two vibrational states, we introduce the degree of coherence [5, 48] defined as

$$(\tilde{\rho}_{\text{vib}})_{vv'} \equiv \frac{|(\rho_{\text{vib}})_{vv'}|}{\sqrt{(\rho_{\text{vib}})_{vv}(\rho_{\text{vib}})_{v'v'}}} \quad \text{or} \quad 0, \tag{2.13}$$

which satisfies $0 \leq (\tilde{\rho}_{\text{vib}})_{vv'} \leq 1$. In Eq. (2.13), we define $(\tilde{\rho}_{\text{vib}})_{vv'} = 0$ when $(\rho_{\text{vib}})_{vv} = 0$ or $(\rho_{\text{vib}})_{v'v'} = 0$ because $a_{vk} = 0$, $\forall k$ should hold if $(\rho_{\text{vib}})_{vv} = \sum_{k=1}^{k_{\max}} |a_{vk}|^2 = 0$ is satisfied, and consequently, $(\rho_{\text{vib}})_{vv'} = \sum_{k=1}^{k_{\max}} a_{vk} a_{v'k}^* = 0$ is also satisfied.

From Eqs. (2.12) and (2.13), the purity can be related to the degree of coherence as

$$P = \sum_{v=0}^{v_{\max}} |(\rho_{\text{vib}})_{vv}|^2 + \sum_{v \neq v'}^{v_{\max}} (\tilde{\rho}_{\text{vib}})_{vv'}^2 (\rho_{\text{vib}})_{vv} (\rho_{\text{vib}})_{v'v'}. \qquad (2.14)$$

When the population is equally distributed, i.e., $(\rho_{\text{vib}})_{vv} = 1/v_{\max}$ for all v, the purity takes the minimum value of $P_{\min} = 1/v_{\max}$ and the degree of coherence is zero. If the degree of coherence takes its maximum value, i.e., $(\tilde{\rho}_{\text{vib}})_{vv'} = 1$ for all v and v', the purity becomes unity as

$$\begin{aligned} P &= \sum_{v=0}^{v_{\max}} |(\rho_{\text{vib}})_{vv}|^2 + \sum_{v \neq v'}^{v_{\max}} (\rho_{\text{vib}})_{vv} (\rho_{\text{vib}})_{v'v'} \\ &= \left| \sum_{v=0}^{v_{\max}} (\rho_{\text{vib}})_{vv} \right|^2 = 1, \end{aligned} \qquad (2.15)$$

meaning that the total system is nonentangled.

2.2 Numerical procedure

2.2.1 One-dimensional model

After separating out the motion of the center of mass, the Hamiltonian of H_2 interacting with a light field within the dipole approximation is expressed as

$$H = T_0 + V = T_e + T_N + V_{eN} + V_{ee} + V_{NN} + V_{int}, \tag{2.16}$$

where V_{int} is

$$V_{int} = \mu E(t), \tag{2.17}$$

T_e is the kinetic energy operator of two electrons, T_N is the kinetic energy operator of two nuclei, V_{eN} is the Coulomb attraction between two electrons and two protons, V_{NN} is the Coulomb repulsion between two protons, μ is the electric dipole, and $E(t)$ is the linearly polarized electric field of light whose polarization direction is along the one-dimensional axis.

The explicit form of the operators is expressed as

$$T_e + T_N = -\frac{1}{2\mu_e} \left(\frac{\partial^2}{\partial x^2} + \frac{\partial^2}{\partial y^2} \right) - \frac{1}{M} \frac{\partial^2}{\partial R^2}, \tag{2.18a}$$

$$V_{eN} = -\frac{1}{\sqrt{(x - \frac{R}{2})^2 + \alpha(R)}} - \frac{1}{\sqrt{(x + \frac{R}{2})^2 + \alpha(R)}}$$
$$- \frac{1}{\sqrt{(y - \frac{R}{2})^2 + \alpha(R)}} - \frac{1}{\sqrt{(y + \frac{R}{2})^2 + \alpha(R)}}, \tag{2.18b}$$

$$V_{ee} = \frac{1}{\sqrt{(x - y)^2 + \beta}}, \tag{2.18c}$$

$$V_{NN} = \frac{1}{R}, \tag{2.18d}$$

where x and y are the coordinates of the two electrons whose origin is located at the center of mass of the nuclei, R is the internuclear distance, $M = 1.836 \times 10^3$ a.u. is the mass of a proton, and $\mu_e = 2M/(2M + 1)$ is the reduced mass of an electron. The dipole operator μ is defined as $\mu = x + y$. The soft-core potential [63] is applied for V_{eN} and V_{ee}, in which the Coulomb singularities are eliminated by the softening parameters, $\alpha(R)$ and β. The parameter $\alpha(R)$ is determined so that the $1s\sigma_g$ potential energy curve of H_2^+ [64] is reproduced. On the other hand, β is determined so that the equilibrium internuclear distance of H_2 in the electronic ground state, $R_{eq}^{ref.} = 1.401$ a.u. [64], is reproduced. We solve the TDSE numerically with a grid method called the symmetry-adapted grid method that we have developed to efficiently calculate single-ionization processes in atoms and molecules as we explain in the next subsection.

In the present model, Ψ_S is a function of (x, y, R), ϕ_k is a function of x, and χ_v is a function of (y, R). Because we can adopt any type of complete orthonormal basis to describe a photoelectron in the calculation of ρ_{vib} as long as the basis has a vanishing overlap with the basis set describing the other electron bound to the H_2^+ core, we adopt

the grid basis as a complete orthonormal basis with which we describe the subsystem of a photoelectron, and rewrite Eq. (2.7) as

$$|\Phi_S\rangle = \sum_{v=0}^{v_{\max}} \sum_{k=1}^{d_e} \tilde{a}_{vk} |\chi_v\rangle \otimes |x_k\rangle, \tag{2.19}$$

where d_e is the number of grid points along the x axis. The grid basis $\{|x_k\rangle\}$ satisfies

$$\langle y, R | \langle x_k | \Phi_S\rangle = \Phi_S(x_k, y, R)\Delta_x^{1/2}, \tag{2.20}$$

where $\Delta_x^{1/2}$ is the grid spacing along the x axis. The reduced density matrix is expressed as

$$\rho_{\text{vib}} = \text{Tr}_e\left(|\Phi_S\rangle \langle \Phi_S|\right) = \sum_{v,v'=0}^{v_{\max}} \sum_{k=1}^{d_e} \tilde{a}_{vk}\tilde{a}_{v'k}^* |\chi_v\rangle \langle \chi_{v'}|. \tag{2.21}$$

2.2.2 Symmetry adapted grid method

First, we propagate the electronic and vibrational ground state of H_2, $|\Phi_0^{H_2}\rangle$, in the light field as

$$|\Phi(t)\rangle = U(t) |\Phi_0^{H_2}\rangle, \tag{2.22}$$

where $U(t)$ is the propagator corresponding to the time-dependent Hamiltonian, Eq. (2.16), and project out the initial state as

$$|\Phi'(t)\rangle = \left(1 - |\Phi_0^{H_2}\rangle \langle \Phi_0^{H_2}|\right) |\Phi(t)\rangle. \tag{2.23}$$

We obtain the wave packet corresponding to the single ionization by extracting the part of $|\Phi'(t)\rangle$ in the domain S_1 or S_2 in Fig. 2.1 at certain time T, which is denoted as $|\Phi_{S_1,S_2}(T)\rangle$. The domains S_1 and S_2 in which one of the electrons is emitted are defined by $|x| > 30$ a.u. and $|y| < 30$ a.u., while the domain B in which both electrons are bound is defined by $|x| < 30$ a.u. and $|y| < 30$ a.u. In order to analyze $|\Phi_{S_1,S_2}(t)\rangle$, we wait until T when the singly ionized wave packet can be described well by the product of the eigenstate of H_2^+ and $|x_k\rangle$.

It should be noted that the wave packet $|\Phi_{S_1,S_2}(T)\rangle$ is composed of (i) a photoelectron and a bound state of $H_2^+(1s\sigma_g)$ and (ii) a photoelectron with the dissociating H_2^+ through the continuum state of $H_2^+(1s\sigma_g)$ above the dissociation threshold or through the continuum state in an electronically excited state of H_2^+ like $2p\sigma_u$. Considering that the scalar product of $|\chi_v\rangle$ and the dissociating states of H_2^+ included in $|\Phi_{S_1,S_2}(T)\rangle$ vanish, the projection of $|\Phi_{S_1,S_2}(T)\rangle$ on $|\chi_v\rangle \otimes |x_k\rangle$ yields $\tilde{a}_{vk}$, that is,

$$\tilde{a}_{vk} = \langle \chi_v | \langle x_k | \Phi_{S_1,S_2}(T)\rangle. \tag{2.24}$$

By using the property of the grid basis expressed in Eq. (2.20), we can simplify Eq. (2.24) as

$$
\begin{aligned}
\tilde{a}_{vk} &= \langle \chi_v | \Phi_{S_1,S_2}(x_k, T) \rangle \, \Delta_x^{1/2} \\
&= \sum_{l,m} \langle \chi_v | y_l, R_m \rangle \, \langle y_l, R_m | \Phi_{S_1,S_2}(x_k, T) \rangle \, \Delta_x^{1/2} \\
&= \sum_{l,m} \chi_v^*(y_l, R_m) \Phi_{S_1,S_2}(x_k, y_l, R_m, T) \Delta_y \Delta_R \Delta_x^{1/2},
\end{aligned}
\tag{2.25}
$$

where $|y_l\rangle$ and $|R_m\rangle$ are the grid bases for the respective coordinates. From Eqs. (2.21) and (2.25), we can obtain the reduced density matrix from which the purity and the degree of coherence are calculated.

We integrate the time-dependent Schrödinger equation numerically by adopting the grid method. We perform the time propagation using the split-operator method expressed as

$$
U(t) = \exp\left[-i\frac{\Delta t}{2}V\left(t + \frac{\Delta t}{2}\right)\right] \exp\left(-i\Delta t T_0\right) \exp\left[-i\frac{\Delta t}{2}V\left(t + \frac{\Delta t}{2}\right)\right],
\tag{2.26}
$$

where $V(t)$ is the potential including the laser–matter interaction and T_0 is the kinetic energy operator [Eq. (2.16)]. For the numerical differentiation, we employ the fast Fourier transform (FFT).

Because we neglect the double ionization, the grid space can be reduced significantly. By following the scheme introduced by Rapp and Bauer [65], we developed a symmetry adapted grid (SAG) method by which we propagate the wave packet described in the two-dimensional grid space [Fig. 2.1(b)] by making full use of the symmetry property of the electronic wave function. In Fig. 2.1(a), the domain B represents H_2 in which both electrons are bound, the domain S represents the single ionization, and the domain D represents the double ionization. Because the spatial wave function of the electronic ground singlet state is symmetric under the exchange of the two electron coordinates, the two domains, S_1 and S_1', are equivalent; so are the two domains, S_2 and S_2'. In the SAG method, we can reduce the computational cost significantly. Indeed, the wave packet propagation only in the domains B, S_1, and S_2 [Fig. 2.1(b)] is sufficient for describing the wave packet corresponding to the single ionization.

In order to avoid the spurious reflection at the edge of the grid space, a complex absorbing potential (CAP) [66] is applied to the red peripheral region in Fig. 2.1. Because the wave packet being propagated from the domain S into D should be absorbed in the SAG method, the CAP is applied to the red-colored upper and lower boundary regions in Fig. 2.1(b).

Because the wave packet going into the domain S_1' from B should not be absorbed, the CAP cannot be applied in the blue-colored upper and lower regions in Fig. 2.1(b). However, if there is no CAP there, a spurious reflection could occur. We can solve this problem by utilizing the symmetry of the wave function and the symmetry of the Hamiltonian under the exchange of two electronic coordinates.

By denoting the wave function after the operation of the first term of the propagator
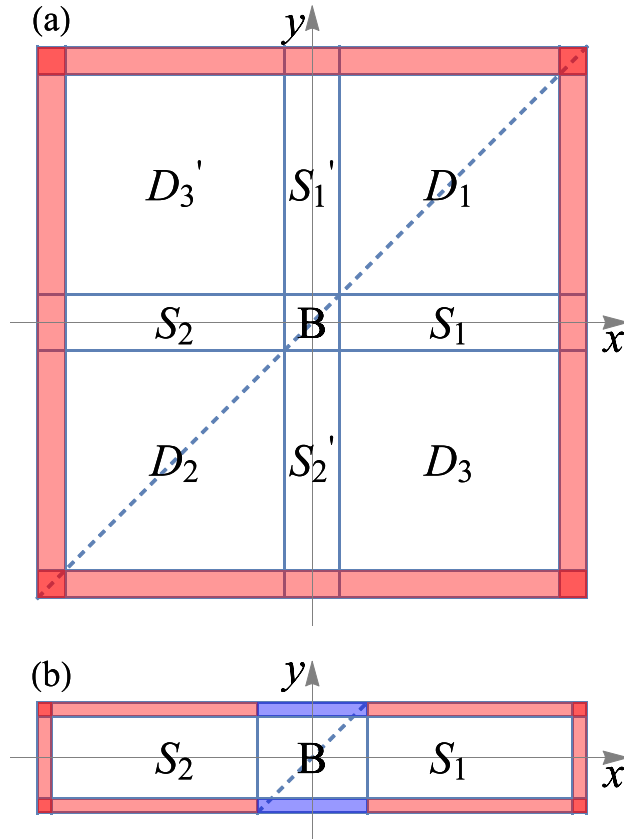
Figure 2.1: (a) The grid space in the conventional grid method. In domain B both electrons are bound. The domain S represents single ionization and the domain D represents double ionization. (b) The grid space in the SAG method. The red peripheral region represents the CAP. In the peripheral region (in blue color) above and below the domain B, the reflection is avoided without using the CAP.

in Eq. (2.26) as

$$|\Phi'\rangle \equiv \exp\left\{-\mathrm{i}\frac{\Delta t}{2}V\left(t+\frac{\Delta t}{2}\right)\right\}, \tag{2.27}$$

the operation of the second term in the propagator on the wave function reads

$$\exp(-\mathrm{i}\Delta t T_0)|\Phi'\rangle = \exp\left\{-\mathrm{i}\Delta t\frac{1}{M}\frac{\partial^2}{\partial R^2}\right\}\exp\left\{-\mathrm{i}\Delta t\frac{1}{2\mu_e}\frac{\partial^2}{\partial x^2}\right\}$$
$$\times \exp\left\{-\mathrm{i}\Delta t\frac{1}{2\mu_e}\frac{\partial^2}{\partial y^2}\right\}|\Phi'\rangle. \tag{2.28}$$

In the SAG method, the differentiation along y is rewritten by utilizing the symmetry of the wave function and the kinetic energy operator as

$$\exp\left\{-\mathrm{i}\Delta t\frac{1}{2\mu_e}\frac{\partial^2}{\partial y^2}\right\}|\Phi'\rangle$$
$$\longrightarrow P_{xy}Q_{\mathrm{B}}\left[\exp\left\{-\mathrm{i}\Delta t\frac{1}{2\mu_e}\frac{\partial^2}{\partial x^2}\right\}|\Phi'\rangle\right] + Q_{\mathrm{S}}\left[\exp\left\{-\mathrm{i}\Delta t\frac{1}{2\mu_e}\frac{\partial^2}{\partial y^2}\right\}|\Phi'\rangle\right], \tag{2.29}$$

where $P_{x}y$ exchanges x and y, and Q_{B} and Q_{S} extract the wave packets in the domains B and S, respectively. The second term represents the differentiation along y in the domain S.

We note here that we can apply the SAG method to the triplet state by modifying Eq. (2.29) as

$$\exp\left\{-\mathrm{i}\Delta t\frac{1}{2\mu_e}\frac{\partial^2}{\partial y^2}\right\}|\Phi'\rangle$$
$$\longrightarrow P_{xy}Q_{\mathrm{B}}\left[-\exp\left\{-\mathrm{i}\Delta t\frac{1}{2\mu_e}\frac{\partial^2}{\partial x^2}\right\}|\Phi'\rangle\right] + Q_{\mathrm{S}}\left[\exp\left\{-\mathrm{i}\Delta t\frac{1}{2\mu_e}\frac{\partial^2}{\partial y^2}\right\}|\Phi'\rangle\right], \tag{2.30}$$

by taking into account the fact that the spatial wave function of a triplet state is anti-symmetric.

In order to examine the accuracy of the SAG method, we performed test calculations with the nuclei fixed at the equilibrium distance of H_2. The electronic ground state of H_2 is obtained by imaginary-time propagation. We stop the wave-packet propagation 7.257 fs after the interaction with the laser pulse (40 nm, 20 cycles, and $1.0 \times 10^{15}\,\mathrm{W\,cm^{-2}}$). The spatial distributions of the wave packet along the x direction, ρ_x, and y direction, ρ_y, defined as

$$\rho_x = \int dy\, |\Phi(x,y)|^2, \rho_y = \int dx\, |\Phi(x,y)|^2, \tag{2.31}$$

are shown in Fig. 2.2. In this test calculation, the grid space for the conventional grid method is defined as $|x|$, $|y| \leq 500\,\mathrm{a.u.}$, and for the SAG method as $|x| \leq 500\,\mathrm{a.u.}$, $|y| \leq 30\,\mathrm{a.u.}$; i.e., the grid space is reduced by about $500/30 \simeq 17$ times. For the longer time propagation, the grid space needs to be enlarged. When the size of the two-dimensional

24
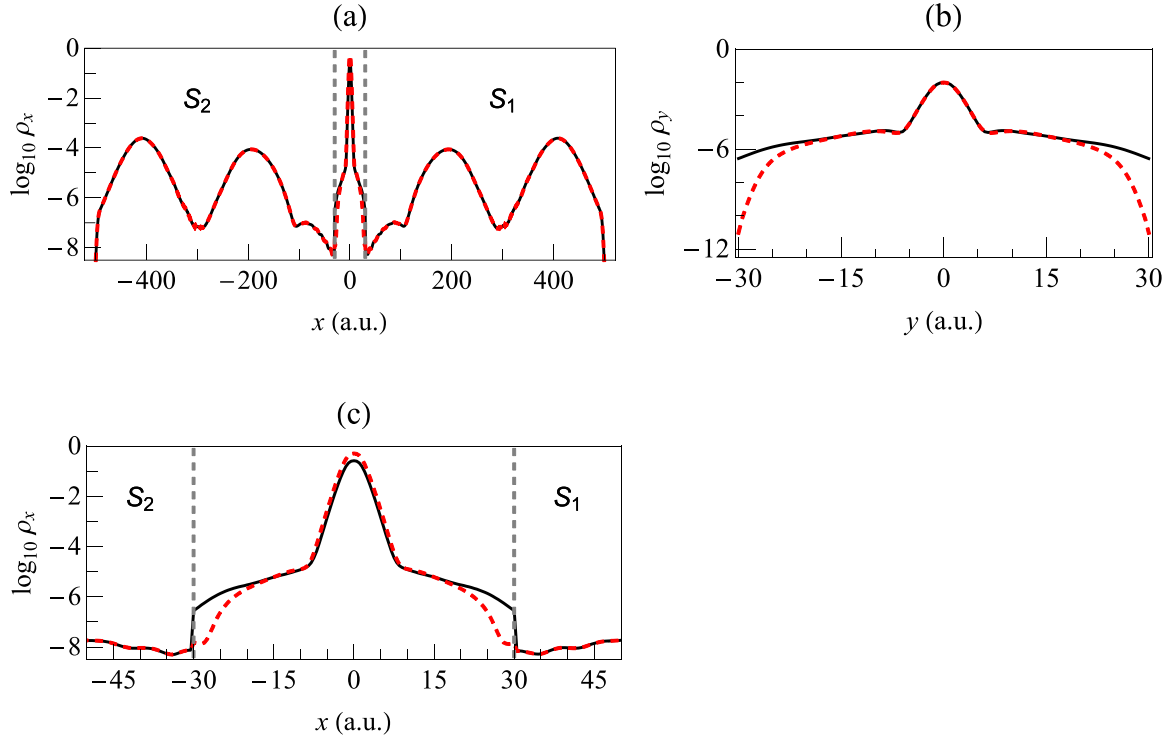
Figure 2.2: Spatial distributions of the wave packet along (a) the x direction and (b) the y direction obtained by the SAG method (red dashed curve) and those obtained by the conventional grid method (black solid curve) at the propagation time of 7.257 fs after the interaction with the laser pulse. The enlarged view of (a) is shown in (c). In (a),(c), the boundaries between domain B and domains S_1 and S_2 are indicated by the vertical dashed lines at $x = \pm 30$ a.u.

grid space is as $L \times L$, the required memory size is proportional to L in the SAG method while it is proportional to L^2 in the conventional method.

In Figs. 2.2 and 2.3, the black curves show the results with the conventional grid method, while the red ones show the results with the SAG method. In Fig. 2.2(a) the relative error is smaller than 2% in the domains S_1 and S_2, where the red and the black curves overlap each other almost completely. In Fig. 2.3(a), the photoelectron spectra obtained by the Fourier transform of the wave packet in the domains S_1 and S_2 are normalized by their own maxima, where the red and the black curves overlap each other almost completely. There are two peaks at 0.66 and at 0.13 a.u. By comparing the photon energy, 1.139 a.u., with the energy gap between the initial state and $1s\sigma_g$ of H_2^+, 0.482 a.u., and with the energy gap between the initial state and $2p\sigma_u$ of H_2^+, 1.006 a.u., the higher energy peak corresponds to the direct ionization to $1s\sigma_g$ while the lower energy peak corresponds to the ionization to $2p\sigma_u$, which is called a shakeup process. In Fig. 2.3(b), the difference between the two spectra calculated by subtracting the amplitude obtained by the conventional method from that obtained by the SAG method is plotted. As shown in this figure, the absolute values of the difference are smaller than 0.00132 even in the photoelectron kinetic energy regions of $0.05 - 0.30$ a.u. and $0.57 - 0.80$ a.u.
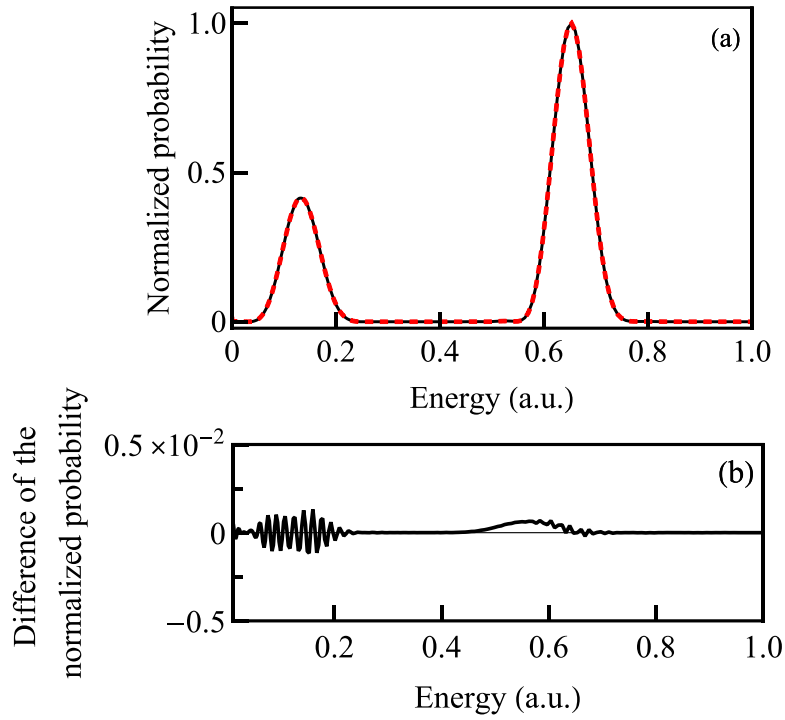
Figure 2.3: (a) Photoelectron energy distributions obtained by the SAG method (red dashed curve) and those obtained by the conventional grid method (black solid curve). (b) Magnified difference defined as "the red curve" and "the black curve" in (a).

As mentioned in the paragraph before Eq. (2.24), the wave packet $|\Phi_{S_1,S_2}(T)\rangle$ has the contribution from the electronically excited states of H_2^+ like $2p\sigma_u$. However, we eliminate the contribution from such electronic states by projecting $|\Phi_{S_1,S_2}(T)\rangle$ on the

electronic ground state of H_2^+, by which we can calculate the reduced density matrix of the vibrational states in the electronic ground state.

2.2.3   Time propagation
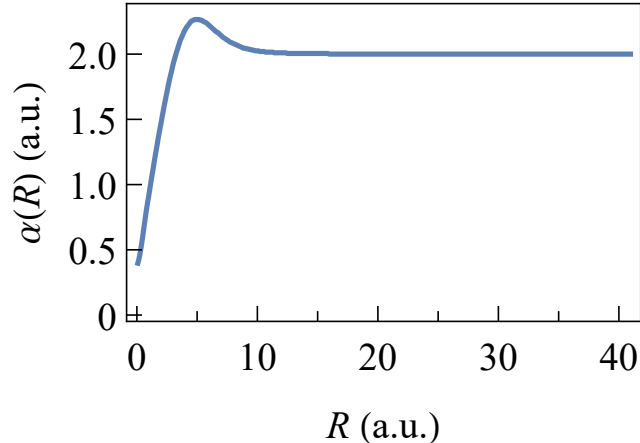
Figure 2.4: The softening parameter $\alpha(R)$ in Eq. (2.18b) as a function of the internuclear distance.

We obtain first the initial state by the imaginary-time propagation [67]. As the grid spacing, we adopt $\Delta_x = \Delta_y = 0.50$ a.u. and $\Delta_R = 0.08$ a.u. The grid size is $|x| \le 500$ a.u., $|y| \le 30$ a.u., and 0.08 a.u. $\le R \le 40.96$ a.u. The softening parameter for the electron-nuclear attraction $\alpha(R)$ is shown in Fig. 2.4 and that for the electron-electron repulsion is $\beta = 0.35$. In the time propagation by the split-operator method, we adopt FFT [68–70]. The time step for the imaginary-time propagation, $\Delta\tau$, is $\Delta\tau = 0.05$ a.u. for H_2^+ and that for H_2 is $\Delta\tau = 0.10$ a.u. In order to resolve the small energy difference among the vibrationally highly excited states of H_2^+, we adopt the smaller time step for H_2^+.

We calculate the energy and the equilibrium internuclear distance of H_2 in the electronic ground state to be $E_0^{1D} = -1.036$ a.u. and $R_{eq}^{1D} = 1.397$ a.u., respectively, which are in good agreement with the reference values of $E_0^{ref.} = -1.165$ a.u. and $R_{eq}^{ref.} = 1.401$ a.u., obtained by solving the time-independent Schrödinger equation with the exact potential energy curve [64].

The functional form of the complex absorbing potential (CAP) is

$$V_{CAP}^{\xi} = \begin{cases} -i\eta_\xi(|\xi| - \xi_{CAP})^2, & |\xi| \ge \xi_{CAP} \\ 0, & \text{elsewhere} \end{cases}, \tag{2.32}$$

where $\xi = x, y$, and R. We adopt $\eta_x = \eta_y = 0.05$, $x_{CAP} = 450$ a.u., $y_{CAP} = 25$ a.u., $\eta_R = 0.01$, and $R_{CAP} = 32.96$ a.u. We consider that a hydrogen molecule in the ground state is exposed to a Fourier-limited laser pulse having a cosine-squared envelope,

$$E(t) = \begin{cases} E_0 \cos^2\left(\frac{\pi}{T_{pulse}} t\right)\cos(\omega t), & |t| \le T_{pulse}/2 \\ 0, & \text{otherwise} \end{cases}, \tag{2.33}$$

where T_{pulse} defined as

$$T_{\text{pulse}} = N\frac{2\pi}{\omega} \tag{2.34}$$

is referred to as the pulse duration and N is the number of optical cycles. The light-field intensity is in the range of $I = 5 \times 10^{12} - 10^{16}\,\text{W\,cm}^{-2}$ and the central wavelength of the light field is in the range of $\lambda = 20 - 90\text{nm}$. The time step is $\Delta t = 0.1\,\text{a.u.}$ After the light field vanishes, the field-free propagation proceeds until certain time T. The reduced density matrix is calculated and renormalized so that $\text{Tr}(\rho_{\text{vib}}) = 1$ is satisfied.

2.3 Results and discussion

2.3.1 Entanglement and coherence: Pulse duration dependence and wavelength dependence

Table 2.1: The ten sets of the laser parameters.

	Wavelength (nm)	Number of cycles	T_{pulse} (fs)	Intensity (W cm^{-2})	Keldysh parameter
1				5×10^{12}	39
2	90	20	6.0	10^{13}	28
3				10^{15}	2.8
4		3	0.9	10^{13}	28
5				10^{13}	63
6	40	20	2.7	10^{15}	
7		3	0.4	10^{15}	6.3
8		40	2.7	10^{15}	
9	20			10^{15}	12
10		20	1.3	10^{16}	3.9

The purity and the degree of coherence are calculated using the ten different sets of laser parameters listed in Table 2.1. The laser parameters are chosen so that the Keldysh parameter $\gamma \equiv \sqrt{I_P/2U_P}$ satisfies $\gamma > 2$, which means that the contribution from the tunnel ionization can be neglected. Here, $I_P = 0.4387$ a.u. is the ionization potential of the H$_2$ ground state and $U_P = E_0^2/4\omega^2$ is the ponderomotive energy. The definition of T_{pulse} is given by Eq. (2.34).

As shown in Fig. 2.5, the purity increases as the pulse duration decreases, or equivalently, as the spectral bandwidth increases, reflecting the fact that it becomes difficult to specify which one of the vibrational states is prepared only by projecting the photoelectron on its energy eigenstate.

In Fig. 2.6, we show the degree of coherence between the vibrational ground state and the vth vibrational state, $(\tilde{\rho}_{\text{vib}})_{v,0}$, as a function of the vibrational quantum number v. It can be seen that the degree of coherence decreases as the vibrational quantum number increases. It can also be seen in Fig. 2.6 that the degree of coherence decreases as the pulse duration increases for the same v.

When the bandwidth of the laser pulse is smaller than the energy gap between the ground and the vth state, it becomes less probable for the pair of vibrational states to be populated coherently. Therefore, the degree of coherence decreases when the bandwidth decreases by increasing the pulse duration or when the energy gap between the vth level and the ground vibrational state increases by increasing the vibrational quantum number. When the bandwidth becomes extremely small so that the respective vibrational states are exclusively assigned to the specific kinetic energies of the photoelectron, that is, when $a_{vk}a_{v'k}^* \propto \delta_{vv'}$ is satisfied, $(\rho_{\text{vib}})_{vv'} \propto \delta_{vv'}$ holds from Eq. (2.8), representing that the degree of coherence is zero.

In Fig. 2.5, in the case of $\lambda = 40$ nm and $N = 20$ cycles (set 6: open circle) and in the case of $\lambda = 20$ nm and $N = 40$ cycles (set 8: open triangle), the purities are 0.795 and 0.825, respectively. As shown in Fig. 2.6, because the degrees of coherence of these

two cases are almost the same, reflecting the fact that their pulse durations are the same, the small difference in their purities can be ascribed to the difference in the populations. The dependence of the degree of coherence on the pulse duration is consistent with the previous study on the ionization of Xe [48], in which the degree of coherence between two levels of Xe$^+$ was shown to decrease as the pulse duration increases.
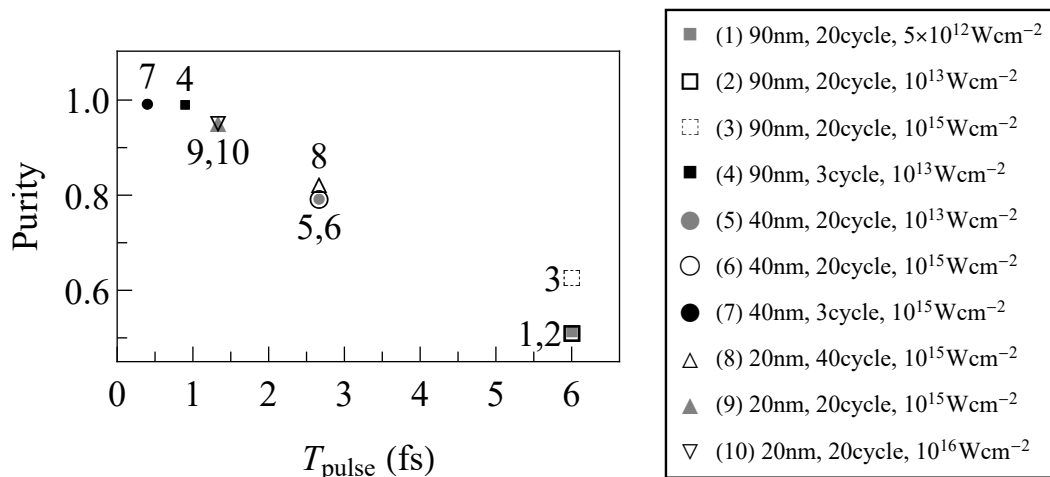
Figure 2.5: The purity as a function of the pulse duration for the ten different sets of laser parameters. In the linear regime, the purity is insensitive to the light-field intensity; e.g., in the case of ($\lambda = 20$ nm, $N = 20$ cycles), the purity at 10^{15} W cm^{-2} (set 9: filled triangle) and the purity at 10^{16} W cm^{-2} (set 10: open triangle) take the same values of 0.954. Similarly, in the case of ($\lambda = 40$ nm, $N = 20$ cycles), the purity at 10^{13} W cm^{-2} (set 5: filled circle, P = 0.796) and the purity at 10^{15} W cm^{-2} (set 6: open circle, P = 0.795) are very close to each other.

2.3.2 Entanglement and coherence: Intensity dependence

a.   Linear regime

We investigate the light-field intensity dependence of the purity and the degree of coherence in the cases of set 1 and set 2 with $\lambda = 90$ nm and $N = 20$ cycles. As shown in Fig. 2.6, the degree of coherence at the light-field intensity of 10^{13} W cm^{-2} (set 2: open square) exhibits almost the same dependence on the vibrational quantum number as the degree of coherence at the light-field intensity of 5×10^{12} W cm^{-2} (set 1: filled square), reflecting the fact that their pulse durations are the same. Because their purities are almost the same as shown in Fig. 2.5, the populations in sets 1 and 2 are expected to be almost the same, which means that the light-field intensities are in the linear regime; that is, the loss of the population in the ground state of H$_2$ as well as the populations in the vibrationally excited states of H$_2^+$ increase linearly in this intensity range by a process corresponding to a one-photon absorption. Indeed, we have confirmed that the loss of the population in the ground state of H$_2$ defined as $1 - \langle \Phi_0^{H_2} | \Phi(T) \rangle$ is 0.033 and 0.016 at 10^{13} W cm^{-2} and 5×10^{12} W cm^{-2}, respectively.
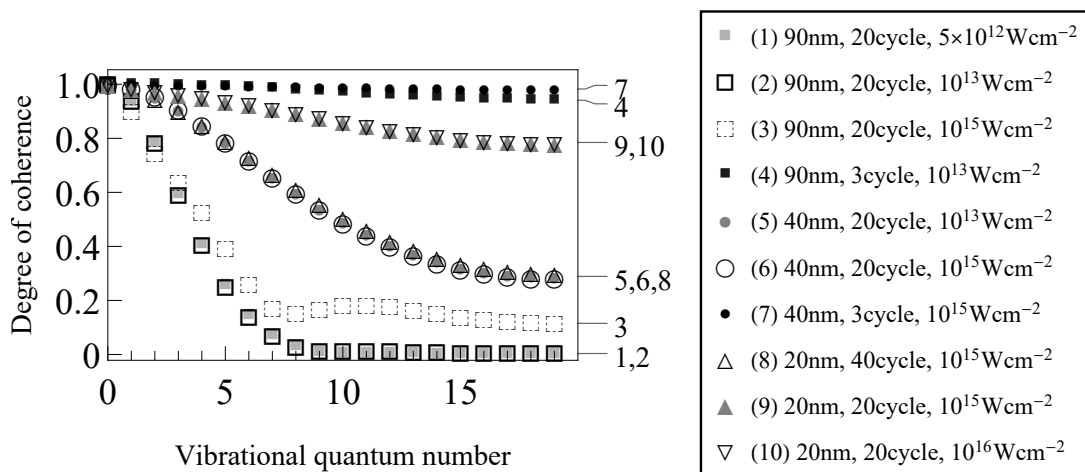
Figure 2.6: The degree of coherence $(\tilde{\rho}_{\mathrm{vib}})_{v,0}$ as a function of the vibrational quantum number and the pulse duration for ten different laser parameters. In the linear regime, the degree of coherence is insensitive to the light-field intensity, e.g., in the case of ($\lambda = 20$ nm, $N = 20$ cycles), the degree of coherence at 10^{15} W cm^{-2} (set 9: filled triangle) is in good agreement with the degree of coherence at 10^{16} W cm^{-2} (set 10: open triangle). Similarly, in the case of ($\lambda = 40$ nm, $N = 20$ cycles), the degree of coherence at 10^{13} W cm^{-2} (set 5: filled circle) is in good agreement with the degree of coherence at 10^{15} W cm^{-2} (set 6: open circle).

We can also see in Figs. 2.5 and 2.6 that, when the light-field intensity is in the linear regime, the purity and the degree of coherence obtained using two different sets of the wavelength and the number of cycles, i.e., (i) set 9 and set 10 ($\lambda = 20$ nm, $N = 20$ cycles) and (ii) set 5 and set 6 ($\lambda = 40$ nm, $N = 20$ cycles), do not vary sensitively on the light-field intensity.

b.   Nonlinear regime

As shown in Fig. 2.6, in the case of $\lambda = 90$ nm and $N = 20$ cycles, the degree of coherence at 10^{15} W cm^{-2} (set 3:open dashed square) deviates largely from the other two cases at 5×10^{12} W cm^{-2} (set 1) and 10^{13} W cm^{-2} (set 2). At 10^{15} W cm^{-2}, the $(\tilde{\rho}_{\mathrm{vib}})_{v,0}$ values for $v = 1$ and 2 are almost the same as the corresponding values for the weaker two cases, but, as the vibrational quantum number increases further, for $v \geq 3$, the $(\tilde{\rho}_{\mathrm{vib}})_{v,0}$ value at 10^{15} W cm^{-2} becomes larger than the corresponding values at 5×10^{12} W cm^{-2} and 10^{13} W cm^{-2}, and the deviation becomes maximum when the vibrational quantum number is $v \sim 11$. This deviation can be ascribed to the second- or higher-order interaction with the light field as described below.

The loss of the ground state of H$_2$ at 10^{15} W cm^{-2} (set 3) is 0.94, which is much larger than the loss of the ground state at 5×10^{12} W cm^{-2} (set 1) and that at 10^{13} W cm^{-2} (set 2), showing that the light-field intensity of 10^{15} W cm^{-2} is no longer in the linear regime. The Keldysh parameter, $\gamma = 2.8$ (see Table 2.1), for set 3 indicates that the photoionization proceeds through the multiphoton process.

Because the transition moment between the ground state of H_2 and the final state composed of the photoelectron and the vibrational state of H_2^+ ($1s\sigma_g$) decreases as the photoelectron energy increases, the ionization probability at 90 nm is larger than the ionization probabilities at the other shorter wavelengths as long as the number of cycles and the intensity are the same. Therefore, at a 90-nm laser pulse, the second or higher-order interaction can no longer be neglected at the intensity reaching $10^{15}\,\mathrm{W\,cm^{-2}}$.

At $10^{15}\,\mathrm{W\,cm^{-2}}$, the second-order interaction with the light field, corresponding to the two-photon process, results in a broader energy distribution of photoelectrons than that of photoelectrons produced from a one-photon process. Therefore, it is expected that the second-order interaction increases the coherence among the vibrational states of H_2^+. On the other hand, the third-order interaction with the light field, corresponding to a three-photon process, increases the coherence not only by creating the photoelectron with a broader energy distribution but also by inducing one-photon ionization followed by Raman-type vibrational excitations.

For instance, if the ionization results in the formation of $|\chi_v\rangle\,|\phi_k\rangle$, a Raman-type transition from $|\chi_v\rangle\,|\phi_k\rangle$ to $|\chi'_v\rangle\,|\phi_k\rangle$ can occur. Consequently, it becomes more probable that the vth and the v'th states are assigned to the same kinetic energy of the photoelectron; therefore, $a_{vk}a^*_{v'k}$ holds in the wider range of k than in the case of the weaker intensities, resulting in the higher coherence.

2.3.3 Purity, coherence, and population

As shown in Fig. 2.5, when $\lambda = 90$ nm and $N = 20$ cycles, the purity at $10^{15}\,\mathrm{W\,cm^{-2}}$ (set 3,$P = 0.626$) is larger by 0.115-0.116 than the purities at $5 \times 10^{12}\,\mathrm{W\,cm^{-2}}$ (set 1, $P = 0.511$) and $10^{13}\,\mathrm{W\,cm^{-2}}$ (set 2, P = 0.510). At $10^{15}\,\mathrm{W\,cm^{-2}}$, because of the transitions among the vibrational states induced by the light field, not only the coherence but also the population can be different from the weaker cases. In order to evaluate the contribution from the population and that from the coherence to the purity, we use the sum of the squared modulus of the population P_1 and the sum of the squared modulus of the coherence P_2 defined in Eq. (2.12).

As shown in Fig. 2.7, the P_2 value at $10^{15}\,\mathrm{W\,cm^{-2}}$ (set 3) is larger than the P_2 values at $5 \times 10^{12}\,\mathrm{W\,cm^{-2}}$ (set 1) and $10^{13}\,\mathrm{W\,cm^{-2}}$ (set 2), which is consistent with the above explanation about the increase in the degree of coherence. On the other hand, the contribution from the P_1 value at $10^{15}\,\mathrm{W\,cm^{-2}}$ is smaller than the P_1 values at $5 \times 10^{12}\,\mathrm{W\,cm^{-2}}$ and $10^{13}\,\mathrm{W\,cm^{-2}}$. The smaller value of P_1 means that the population is more equally distributed associated with the Raman-type transitions among the vibrational states. Because the amount of decrease in P_1 is much smaller than the amount of increase in P_2, the purity defined as the sum of P_1 and P_2 becomes larger at $10^{15}\,\mathrm{W\,cm^{-2}}$ than those at $5 \times 10^{12}\,\mathrm{W\,cm^{-2}}$ and $10^{13}\,\mathrm{W\,cm^{-2}}$.

As shown in Fig. 2.7, the contribution from P_2 is much larger than that from P_1 in all the ten cases of the laser parameters. Because the pulse durations considered here are all short enough, the bandwidths of the laser are wider than the energy gaps among the vibrational states of H_2^+, which results in the large coherence. When the pulse duration becomes longer so that the bandwidth becomes comparable with or smaller than the energy gaps among the vibrational states, the contribution from P_1 to the purity
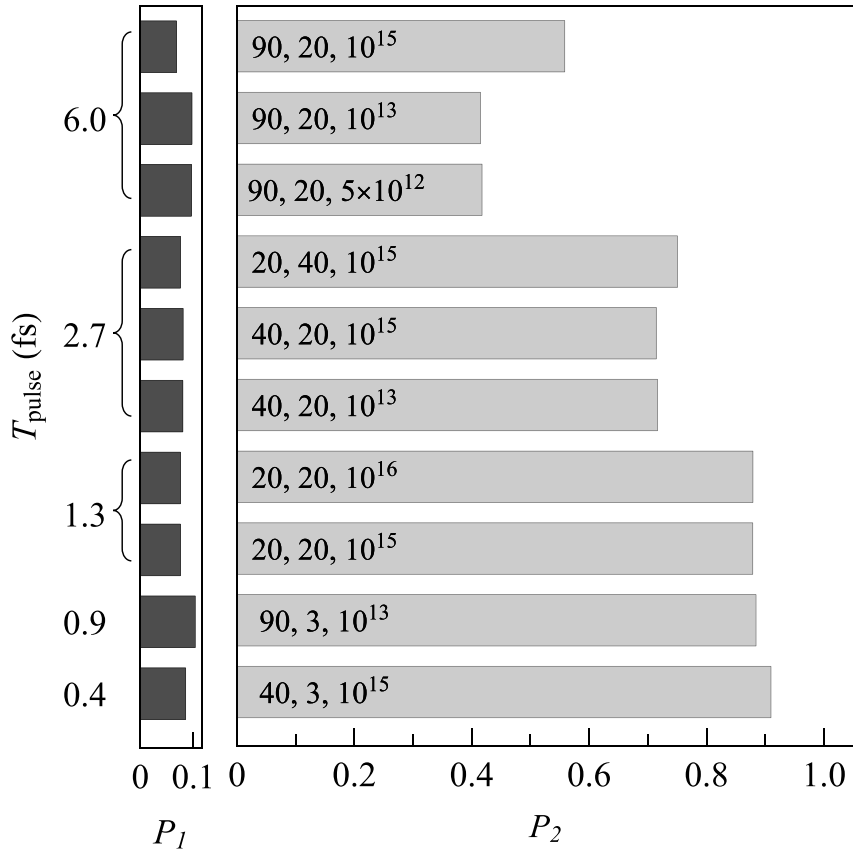
Figure 2.7: The two contributions to the purity, the population P_1 and the coherence P_2, for the ten different laser parameters. The number inside the bar indicates the laser parameters, e.g., the set of "40, 3, and 10^{15}" represents the pulse characterized by the parameters of 40 nm, 3 cycles, and $10^{15}\,\mathrm{W\,cm^{-2}}$.

becomes larger. In an extreme case of the infinitely long pulse duration, corresponding to a continuous wave (cw) laser, the coherence P_2 between vibrational states vanishes, and consequently, the purity is represented by the population P_1 exclusively.

2.3.4 Experimental scheme for determining the reduced density matrix

The reduced density matrix of the vibrational states can be determined by the pump–probe experiment as proposed in Ref. [71]. First, H_2 is ionized by the pump pulse and the resultant vibrational state of H_2^+ is described using ρ_{vib} as in Eq. (2.8). After a certain time delay τ, the probe VUV pulse excites H_2^+ to the $2p\sigma_{\text{u}}$ state and the photofragment, H^+, is produced via the dissociation. We set the origin of time, $t = 0$, at the peak position of the temporal shape of the pump pulse and set the peak position of the probe pulse at $t = \tau$.

By assuming that the electric field of the probe pulse E_{probe} satisfies $E_{\text{probe}}(t - \tau) \neq 0$ during $t \in [t_0, t_f]$, the free propagation until the system is excited by the probe pulse is expressed by

$$U_{\text{free}}(\tau) = \exp\left[-iH_0\left(\tau - \frac{T_{\text{pulse}} + t_f - t_0}{2}\right)\right], \tag{2.35}$$

where H_0 is the field-free Hamiltonian for H_2^+ and T_{pulse} is the duration of the pump pulse defined in Eq. (2.34). The interaction with the probe pulse is expressed in the first order perturbation theory as

$$U_{\text{probe}}(t) = \left[e^{-iH_0(t-t_0)} - i\int_{t_0}^{t} dt_1 e^{-iH_0(t-t_1)}V_{\text{int}}(t_1)e^{-iH_0(t_1-t_0)}\right], \tag{2.36}$$

with

$$V_{\text{int}}(t_1) = \mu E_{\text{probe}}(t_1 - \tau), \tag{2.37}$$

where the probe pulse $E_{\text{probe}}(t_1 - \tau)$ starts interacting with H_2^+ at $t_1 = t_0$ and ends interacting at $t_1 = t_f$.

The observation of $|\chi^u(\omega^u)\rangle$, which is the dissociating eigenstate of $2p\sigma_u$ having the kinetic energy release (KER), ω^u, is expressed using the projection operator $\Pi_u \equiv |\chi^u(\omega^u)\rangle \langle \chi^u(\omega^u)|$ as

$$\Pi_u U_{\text{probe}} U_{\text{free}} \rho_{\text{vib}} U_{\text{free}}^\dagger U_{\text{probe}}^\dagger \Pi_u$$

$$= |\chi^u\rangle \sum_{v,v'=0}^{v_{\text{max}}} (\rho_{\text{vib}})_{vv'} e^{-i(\omega_v - \omega_{v'})(\tau - \frac{T_{\text{pulse}}+t_f-t_0}{2})}$$

$$\times \langle \chi^u| U_{\text{probe}} |\chi_v\rangle \langle \chi^{v'}| U_{\text{probe}}^\dagger |\chi_u\rangle \langle \chi^u|,$$

$$= |\chi^u\rangle \sum_{v,v'=0}^{v_{\text{max}}} (\rho_{\text{vib}})_{vv'} e^{-i(\omega_v - \omega_{v'})(\tau - \frac{T_{\text{pulse}}+t_f-t_0}{2})}$$

$$\times p_v(\omega^u) p_{v'}^*(\omega^u) \langle \chi^u|, \tag{2.38}$$

where ω_v is the eigenenergy of the vth vibrational state and $p_v(\omega^u)$ is the transition amplitude from χ_v to χ^u defined as

$$p_v(\omega^u) = -\mathrm{i}M_v(\omega^u)e^{-\mathrm{i}\omega^u t}e^{\mathrm{i}\omega_v t_0}\int_{t_0}^{t}dt_1 E_{\mathrm{probe}}(t_1 - \tau)e^{\mathrm{i}(\omega^u - \omega_v)t_1}, \tag{2.39}$$

using the transition moment,

$$M_v(\omega^u) \equiv \langle\chi^u|\,\mu\,|\chi_v\rangle. \tag{2.40}$$

The probability of finding $|\chi^u\rangle$ by the detector is a function of the time delay τ and the KER, ω^u, expressed as

$$I(\tau;\omega^u) \equiv \sum_{v,v'=0}^{v_{\mathrm{max}}}(\rho_{\mathrm{vib}})_{vv'}e^{-\mathrm{i}\omega_{vv'}(\tau-\frac{T_{\mathrm{pulse}}+t_f-t_0}{2})}p_v(\omega^u)p_{v'}^*(\omega^u), \tag{2.41}$$

where we defined $\omega_{vv'} \equiv \omega_v - \omega_{v'}$. This probability corresponds to the delay–KER spectrogram defined in Ref. [71]. Because the pulse duration of the probe pulse is short enough so that $E_{\mathrm{probe}}(t_1 - \tau) = 0$ is satisfied when $t_1 < t_0$ or $t_1 > t_f$, the time integral in Eq. (2.39) becomes the Fourier transform of the probe pulse represented as

$$\begin{aligned}
p_v(\omega^u) &= -\mathrm{i}M_v(\omega^u)e^{-\mathrm{i}\omega^u t}e^{\mathrm{i}\omega_v t_0}e^{\mathrm{i}(\omega^u-\omega_v)\tau}\int_{t_0-\tau}^{t-\tau}dt' E_{\mathrm{probe}}(t')e^{\mathrm{i}(\omega^u-\omega_v)t'} \\
&= -\mathrm{i}M_v(\omega^u)e^{-\mathrm{i}\omega^u(t-\tau)}e^{-\mathrm{i}\omega_v(\tau-t_0)}\int_{-\infty}^{\infty}dt' E_{\mathrm{probe}}(t')e^{\mathrm{i}(\omega^u-\omega_v)t'} \\
&= -\mathrm{i}M_v(\omega^u)e^{-\mathrm{i}\omega^u(t-\tau)}e^{-\mathrm{i}\omega_v\frac{t_f-t_0}{2}}\tilde{E}(\omega^u - \omega_v),
\end{aligned} \tag{2.42}$$

where $\tilde{E}(\Omega)$ is the Fourier amplitude of the probe pulse.

By representing $p_v(\omega^u)$ and $p_{v'}^*(\omega^u)$ in Eq. (2.41) by Eq. (2.42), the delay–KER spectrogram is given as

$$\begin{aligned}
I(\tau;\omega^u) \equiv \sum_{v,v'=0}^{v_{\mathrm{max}}}(\rho_{\mathrm{vib}})_{vv'}&e^{-\mathrm{i}\omega_{vv'}(\tau-\frac{T_{\mathrm{pulse}}}{2})} \\
&\times M_v(\omega^u)M_{v'}^*(\omega^u)\tilde{E}(\omega^u-\omega_v)\tilde{E}^*(\omega^u-\omega_{v'}),
\end{aligned} \tag{2.43}$$

By performing the Fourier transform with respect to τ, we obtain the frequency–KER spectrogram as

$$\begin{aligned}
\tilde{I}(\Omega;\omega^u) = \sum_{v=0}^{v_{\mathrm{max}}}(\rho_{\mathrm{vib}})_{vv}&\left|M_v(\omega^u)\tilde{E}(\omega^u-\omega_v)\right|^2\delta(\Omega) \\
&+ \sum_{v,v'=0}^{v_{\mathrm{max}}}\left\{\tilde{I}_{vv'}(\Omega;\omega^u) + \tilde{I}_{vv'}(-\Omega;\omega^u)\right\},
\end{aligned} \tag{2.44}$$

where $\tilde{I}_{vv'}(\Omega;\omega^u)$ is defined as

$$\begin{aligned}
\tilde{I}_{vv'}(\Omega;\omega^u) = (\rho_{\mathrm{vib}})_{vv'}&e^{\mathrm{i}\omega_{vv'}T_{\mathrm{pulse}}/2}M_v(\omega^u)M_{v'}^*(\omega^u) \\
&\times \tilde{E}(\omega^u-\omega_v)\tilde{E}^*(\omega^u-\omega_{v'})\delta(\Omega-\omega_v+\omega_{v'}).
\end{aligned} \tag{2.45}$$

The left-hand side of Eq. (2.45) above, $\tilde{I}_{vv'}(\Omega; \omega^u)$, gives the nonzero complex amplitude only when $\Omega = \omega_{vv'}$, $\omega^u \simeq \omega_p + \omega_v$, and $\omega \simeq \omega_p + \omega_{v'}$ are satisfied, where ω_p represents the frequency component of the probe pulse. Because $\tilde{E}(\omega^u - \omega_v)$ and $\tilde{E}^*(\omega^u - \omega_{v'})$ in Eq. (2.45), varying as a function of ω^u, have the same width, the peak in $\tilde{I}_{vv'}(\Omega; \omega^u)$ at the beat frequency of $\omega_{vv'}$ is spread along the ω^u axis with the width of the product of $\tilde{E}(\omega^u - \omega_v)\tilde{E}^*(\omega^u - \omega_{v'})$. Therefore, in order to obtain the reduced density matrix element, $(\rho_{\mathrm{vib}})_{vv'}$, from the frequency–KER spectrogram, the bandwidth of the probe pulse should be larger than $\omega_{vv'}$. In other words, the pulse duration of the probe pulse should be shorter than the beat period defined as $2\pi/\omega_{vv'}$ in the time domain. This means that, in order to obtain the entire matrix element of the reduced density matrix, the pulse duration of the probe laser pulse needs to be shorter than the shortest beat period of $2\pi/\omega_{0,v_{\max}} = 1.5\,\mathrm{fs}$.

In the frequency–KER spectrogram, there are peaks at the zero frequency $\Omega = 0$ and at the beat frequencies $\Omega = \omega_{vv'}$ as can be seen from Eq. (2.44). As long as the Fourier amplitude of the probe pulse $\tilde{E}(\omega)$ is known, the diagonal elements, $(\rho_{\mathrm{vib}})_{vv'}$, and the off-diagonal elements, $(\rho_{\mathrm{vib}})_{vv'}$, of the reduced density matrix are determined using the transition amplitude $M_v(\omega^u)$, which can be evaluated numerically from the first and second terms in Eq. (2.44), respectively. The purity and the degree of coherence can be calculated from Eqs. (2.10) and (2.13), respectively, using the reduced density matrix. We note that, even if the Fourier transform of the probe pulse is not known in advance, the matrix elements of the reduced density matrix can be determined from the frequency–KER spectrogram using the iterative method proposed in Refs. [71, 72].

As described above, we can extract the purity and the degree of coherence experimentally in the following steps. First, we ionize H_2 by the irradiation of an ultrashort XUV pulse, dissociate the resultant H_2^+ by the irradiation of a subsequent probe VUV pulse, and record the KER distribution of the photofragment, H^+. Then, by performing the Fourier transform of the delay–KER spectrum, we obtain a frequency–KER spectrogram and extract the matrix elements of the reduced density matrix of ρ_{vib} from Eq. (2.44). Finally, we calculate the purity and the degree of coherence from Eqs. (2.10) and (2.13), respectively.

2.4 Conclusion

We have investigated theoretically the photoionization process of H_2 induced by the irradiation of an ultrashort XUV laser pulse by regarding H_2^+ and a photoelectron as a bipartite system, and have analyzed the relation between the purity, which quantifies the entanglement between H_2^+ and the photoelectron, and the coherence in the vibrational states of H_2^+.

We perform one-dimensional propagation of the wave packet represented by the grid basis to describe the ionization of H_2^+ and demonstrate how the purity and the coherence depend on the laser parameters in the range of I (peak field intensity) $= 5 \times 10^{12} - 10^{16}\,W\,cm^{-2}$, λ (the central wavelength) $= 20 - 90$ nm, and T_{pulse} (the pulse duration) $= 0.4 - 6.0\,fs$.

(i) As the pulse duration increases the degree of coherence decreases, reflecting the fact that it becomes less probable for the two states to be coherently populated. The degree of coherence also decreases as the energy gap between the two vibrational states increases by the same reason.

(ii) As long as the laser intensity is weak enough so that the loss of the population in the ground state of H_2 depends linearly on the laser intensity, the purity and the coherence are insensitive to the peak intensity of the laser pulse. On the other hand, when the laser intensity becomes so strong that the Raman-type transitions among the vibrational states of H_2^+ cannot be neglected, the purity and the degree of coherence vary depending on the laser intensity. In the case of $\lambda = 90$ nm and $N = 20$ cycles, both the degree of coherence and the purity increase when the laser intensity is raised to $I = 10^{15}\,W\,cm^{-2}$ from $5 \times 10^{12}\,W\,cm^{-2}$ and $10^{13}\,W\,cm^{-2}$.

(iii) When the pulse duration is short enough so that the bandwidth of the pulse is comparable to or larger than the energy gaps between the vibrational states of H_2^+, the coherence makes the dominant contribution to the purity while the population makes the minor contribution. Because the extent of the entanglement increases when the purity decreases, the extent of the entanglement between the vibrational states of H_2^+ and the photoelectron increases as the coherence among the vibrational states decreases as long as the pulse duration is short enough so that the bandwidth is comparable to or larger than the energy gaps between the vibrational states.

(iv) The procedure for deriving the purity and the degree of coherence from experimental data is proposed. Once the experimental delay–KER spectrogram is recorded by pump–probe measurements, the frequency–KER spectrogram is obtained by the Fourier transform, from which the reduced density matrix is obtained. Then, the purity and the degree of coherence are calculated from the matrix elements of the reduced density matrix.

Chapter 3

Time delay in the coherent vibrational motion of H_2^+ created by photoionization of H_2

Ionization creates a high amount of quantum correlation between internal states, called coherence, in a photoelectron as well as in an ion. It has been known that the coherence in the photoelectron created through the photoionization can be affected by the presence of the ion, partly because of the Coulomb interaction between them. On the other hand, even though the coherence in the ion can also be precisely characterized using ultrashort laser pulses, less attention has been payed to how the photoelectron affects the coherence in the ion.

For the photoionization of a hydrogen molecule, Nabekawa *et al.* [71] has experimentally observed a clue of the effect of photoelectron on the vibrational motion of the hydrogen molecular ion but its interpretation has remained difficult. I will show that the correlation between the photoelectron and the molecular ion was not appropriately treated in Ref. [71], and revealed that the photoelectron affects the coherence in the vibrational motion of the molecule not through the direct Coulomb interaction between them but due to the nonlocal nature of the wave function of the total system composed of the photoelectron and the ion.

3.1 Coherent motion of ions and photoelectrons

3.1.1 Characterization of coherent motion of ions

By attosecond time-resolved spectroscopy, we are able to characterize the coherent internal motion in an atomic or molecular ion created by photoionization [5,6] as well as in a neutral atom or molecule [7–10]. It has been known that the coherent internal motion created in the ion is described by the reduced density matrix $\rho_{\rm ion}$, which can be derived by the measurements of transient absorption [5, 11, 12] and by the streaking of photoelectrons [13,14]. Goulielmakis *et al.* [5] ionized Kr by a few-cycle intense near-IR (NIR) laser pulse and recorded the transient absorption spectra of Kr^+ using an attosecond XUV pulse, from which they derived experimentally the phase of the reduced density-matrix elements of Kr^+, $\arg[(\rho_{\rm ion})_{ij}]$, for the ith and jth levels. They showed that the amplitude of the reduced density matrix $|(\rho_{\rm ion})_{ij}|$ was in good agreement with the theoretical calculation.

When we treat the reduced density matrix $\rho_{\rm ion}$, we also need to take into account the phase originating from the photoelectron. This is because the phase of the reduced density matrix is composed not only of the phase of the NIR pulse and the dynamical phase $\omega_{ij}\tau$, defined as a product of ω_{ij} (the beat frequency between the ith and the jth levels) and τ (the pump–probe time delay), but also of the complex phase originating from the photoelectron represented as a complex momentum eigenfunction [73]. However, to the best of our knowledge, the phase of the photoelectron wave function has not been explicitly considered in the determination of the reduced density matrix in the previous studies [5, 11–14, 74, 75].

3.1.2 Coherent motion of photoelectrons and the Wigner delay

On the other hand, the phase of the photoelectron has been intensively investigated in terms of the Wigner delay [15–18], which is defined as the derivative of the phase of the transition amplitude with respect to the energy of the photoelectron and can be interpreted as the group delay of the photoelectron wave packet escaping from the short-range potential created around the ion core [17]. The Wigner delay has been experimentally evaluated by the methods of attosecond streaking [17,19,76] and the reconstruction of attosecond beating by interference of two-photon transitions (RABBITT) [18,77–79]. The photoemission delay [19], which can be determined experimentally, is composed of the Wigner delay, the delay induced by the long-range part of the Coulombic potential, and the delay originating from the interaction with the probe laser field.

Because the Wigner delay originates from the interaction between the photoelectron and the ion, it depends on the ionic state of atoms and molecules. Indeed, by attosecond (as) streaking spectroscopy, it was revealed by Ossiander *et al.* [19] that the photoemission associated with the ionization of He $[He^+(n = 1) + e^-]$ is delayed by 12.6 as from the photoemission associated with the shake-up ionization of He $[He^+(n = 2) + e^-]$ and that the photoemission delay can be ascribed to the difference in the Coulombic interaction in $He^+(n = 1)$ and that in $He^+(n = 2)$. By cold target recoil ion momentum spectroscopy combined with the RABBIT measurements, Cattaneo *et al.* [20] revealed that the Wigner delay varies depending on the internuclear distance of H_2^+ in the course of the dissociative ionization of H_2.

In the following, by describing the light–matter interaction using the first-order perturbation theory with the dipole approximation, we show that the phase of the reduced density matrix appears as an additional time delay intrinsic to each vibrational state of H_2^+ and that, if the photoelectron and H_2^+ are detected in coincidence by the pump–probe method, we can interpret clearly the origin of the phase of the reduced density matrix. Although it has been known that the phase of the reduced density matrix appears as a time delay in the pump–probe signals [5], the effect of the phase of the photoelectron wave function still needs to be explored. Our theoretical study demonstrates that the phase of the reduced density matrix H_2^+ can be obtained experimentally by the pump–probe measurements of H_2 if the pump–probe time delay is measured with sufficiently high precision of the order of tens of attoseconds. Atomic units (a.u.) are adopted throughout this chapter otherwise indicated.

3.2 Coherent nuclear motion created by ionization

We consider a pump–probe scheme to investigate the vibrational states of H_2^+ created by the one-photon ionization of H_2. By the irradiation of a pump XUV pulse, H_2 in the vibrational and electronic ground state is ionized so that H_2^+ in the electronic ground state $(1s\sigma_g)$ and a photoelectron are produced. We adopt the Born–Oppenheimer approximation and neglect the molecular rotation. We assume that the laser polarization direction is parallel to the internuclear axis and adopt the dipole approximation for the light–matter interaction.

3.2.1 Two-center Coulomb wave function

Because the spin state does not change during and after the light–matter interaction within the dipole approximation, we can neglect the spin part as shown in Eq. (2.7) and concentrate on the spatial part of the total system of $H_2^+ + e^-$ represented as

$$|\Phi_S\rangle = \int d\boldsymbol{k}_e \sum_v a_{v\boldsymbol{k}_e} |\chi_v \phi_{1s}\rangle \otimes |\psi_{\boldsymbol{k}_e}\rangle, \tag{3.1}$$

where $|\chi_v \phi_{1s}\rangle = |\chi_v\rangle \otimes |\phi_{1s}\rangle$, $|\chi_v\rangle$ is a vibrational eigenfunction of H_2^+, v is the vibrational quantum number, $|\phi_{1s}\rangle$ is the electronic eigenfunction of the $1s\sigma_g$ state, $|\psi_{\boldsymbol{k}_e}\rangle$ is a two-center Coulomb wave function with the incoming boundary condition adopted in Ref. [80], and $\boldsymbol{k}_e$ is the wave vector of the photoelectron.

We define the z axis as the molecular axis on which two protons are located and set the origin of the z coordinate at the center of two protons. When the two charges Z_a and Z_b are separated by a distance R, the two-center Coulomb wave function [80] is given as

$$\psi_{\boldsymbol{k}_e}(\boldsymbol{r}; R) = (2\pi)^{-3/2} 4\pi \sum_{l=0}^{\infty} \sum_{m=-l}^{l} i^l e^{-i\delta_{lm}}$$
$$\times \Upsilon_{lm}^*(c_e, \theta_e, \varphi_e) \Upsilon_{lm}(c_e, \theta, \varphi) T_{lm}(c_e, \xi; R), \tag{3.2}$$

$$\Upsilon_{lm}(c_e, \theta, \varphi) = S_{lm}(c_e, \cos\theta) \frac{\exp(im\varphi)}{\sqrt{2\pi}}, \tag{3.3}$$

where $\boldsymbol{r} = (r, \theta, \varphi)$, $\boldsymbol{k}_e = (k_e, \theta_e, \varphi_e)$, $c_e = k_e R/2$, and l is the quasiorbital angular momentum quantum number. Because the laser polarization is linear and parallel to the internuclear axis, only odd l's in Eq. (3.2) have finite contributions to the transition amplitude and $m = 0$ is conserved throughout the ionization process under the dipole approximation. We assume $Z_a = Z_b = 0.5$ a.u. because the total charge of H_2^+ is 1 a.u. We can derive the angular part $S_{lm}(c_e, \eta)$ and the radial part $T_{lm}(c_e, \xi)$ by solving the Schrödinger equation in the prolate spheroidal coordinate system, $\xi = (|\boldsymbol{r} - \boldsymbol{R}/2| + |\boldsymbol{r} + \boldsymbol{R}/2|)/R \in [1, \infty)$, $\eta = (|\boldsymbol{r} - \boldsymbol{R}/2| - |\boldsymbol{r} + \boldsymbol{R}/2|)/R \in [-1, 1]$, and $\varphi \in [0, 2\pi]$. We determine the phase shift $\delta_{lm} = \delta_{lm}(k_e, R)$ of the radial function T_{lm} from the asymptotic behavior of T_{lm} at $\xi \to \infty$. In addition, we have confirmed that the intrinsic phase, which we introduce in Eq. (3.9), converges when $l = 1, 3$, and 5 are included, which can be rationalized by the low kinetic energy $(< 1\,\text{a.u.})$ of photoelectrons considered in the present study. The detail of the numerical procedure for calculating the two-center Coulomb wave function is given in Appendix A.

3.2.2 Pump process

In the first-order perturbation theory, the transition amplitude from the ground state of H_2, $|\chi_0^{H_2}\phi_g\rangle$, to the final state $|\chi_v\phi_{1s}\psi_{\boldsymbol{k}_e}\rangle$ at a certain time t after the electric field of the pump pulse vanishes reads

$$a_{v\boldsymbol{k}_e} = -iM_{v\boldsymbol{k}_e}e^{-i(\omega_v+\omega_{\boldsymbol{k}_e})t}\tilde{E}_1(\omega_v + \omega_{\boldsymbol{k}_e} - \omega_g), \tag{3.4}$$

where $\tilde{E}_1$ is the Fourier transform of the pump pulse, ω_v, $\omega_{\boldsymbol{k}_e}$, and ω_g are the eigenenergies of $|\chi_v\phi_{1s}\rangle$, $|\psi_{\boldsymbol{k}_e}\rangle$, and $|\chi_0^{H_2}\phi_g\rangle$, respectively, and we define the transition moment as

$$M_{v\boldsymbol{k}_e} \equiv \int dR\chi_v(R)\chi_0^{H_2}(R)\mu_{\boldsymbol{k}_e}(R) \tag{3.5}$$

by using the dipole moment given by

$$\mu_{\boldsymbol{k}_e}(R) \equiv \iint d\boldsymbol{r}_1 d\boldsymbol{r}_2 \phi_{1s}(\boldsymbol{r}_1; R)\psi_{\boldsymbol{k}_e}^*(\boldsymbol{r}_2; R)(z_1 + z_2)\phi_g(\boldsymbol{r}_1, \boldsymbol{r}_2; R), \tag{3.6}$$

where z_1 and z_2 represent the z coordinates of the electron bound to H_2^+ and the photo-electron, respectively. The reduced density matrix of H_2^+ is obtained as

$$(\rho_{\text{vib}})_{vv'} = \text{Tr}_e[|\Phi_S\rangle\langle\Phi_S|] = \int d\boldsymbol{k}_e a_{v\boldsymbol{k}_e}a_{v'\boldsymbol{k}_e}^*$$
$$= e^{-i\omega_{vv'}t}(\tilde{\rho}_{\text{vib}})_{vv'} \tag{3.7}$$

with $\omega_{vv'} = \omega_v - \omega_{v'}$. Because the factor $e^{-i\omega_{vv'}t}$ represents the field-free propagation, non-trivial information of the ionization process is expressed by $(\tilde{\rho}_{\text{vib}})_{vv'}$ defined as

$$(\tilde{\rho}_{\text{vib}})_{vv'} = \int d\boldsymbol{k}_e e^{i(\delta_{v\boldsymbol{k}_e}-\delta_{v'\boldsymbol{k}_e})}|M_{v\boldsymbol{k}_e}||M_{v'\boldsymbol{k}_e}^*|$$
$$\times \tilde{E}_1(\omega_v + \omega_{\boldsymbol{k}_e} - \omega_g)\tilde{E}_1^*(\omega_{v'} + \omega_{\boldsymbol{k}_e} - \omega_g), \tag{3.8}$$

where $\delta_{v\boldsymbol{k}_e} \equiv \arg[M_{v\boldsymbol{k}_e}]$. We define the phase of $(\tilde{\rho}_{\text{vib}})_{vv'}$,

$$\Delta_{vv'} \equiv \arg[(\tilde{\rho}_{\text{vib}})_{vv'}], \tag{3.9}$$

as the intrinsic phase between vth and v'th vibrational states. In the time domain, the phase is equivalent to an additional time delay [5] in the coherent motion of H_2^+ because

$$(\rho_{\text{vib}})_{vv'} = e^{-i\omega_{vv'}(t-\tau_{vv'})}|(\tilde{\rho}_{\text{vib}})_{vv'}|, \tag{3.10}$$

where $\tau_{vv'}$ represents the intrinsic time delay defined as

$$\tau_{vv'} \equiv \Delta_{vv'}/\omega_{vv'}. \tag{3.11}$$

Because we assume the pump pulse is Fourier limited, $\tilde{E}_1$ is a real-valued function. Therefore, the origin of the intrinsic phase resides in the phase of the transition moment,

$\delta_{v\boldsymbol{k}_{\mathrm{e}}} \equiv \arg[M_{v\boldsymbol{k}_{\mathrm{e}}}]$. It should be noted that, if we adopt the Franck–Condon approximation, the phase of $\mu_{\boldsymbol{k}_{\mathrm{e}}}$ does not depend on R, and consequently $\delta_{v\boldsymbol{k}_{\mathrm{e}}}$ can be calculated as

$$\begin{aligned}\delta_{v\boldsymbol{k}_{\mathrm{e}}} &= \arg\left[\mu_{\boldsymbol{k}_{\mathrm{e}}}(R_{\mathrm{e}}) \int dR \chi_v(R) \chi_0^{\mathrm{H}_2}(R)\right] \\ &= \arg[\mu_{\boldsymbol{k}_{\mathrm{e}}}(R_{\mathrm{e}})] \quad \text{for all } v,\end{aligned} \tag{3.12}$$

where R_{e} is the equilibrium distance of H_2, because χ_v and $\chi_0^{\mathrm{H}_2}$ are real-valued functions and the integral with respect to R does not contribute to the phase. Equation (3.12) shows that, if we adopt the Franck–Condon approximation, $\delta_{v\boldsymbol{k}_{\mathrm{e}}}$ does not depend on v and that the intrinsic phase $\Delta_{vv'}$ vanishes.

The photoelectron experiences a different Coulombic potential depending on the internuclear distance of H_2^+. The R-dependent phase shift of the photoelectron wave function $\arg[\psi_{\boldsymbol{k}_{\mathrm{e}}}]$ is integrated over R with $\chi_v(R)$ as shown in Eq. (3.5), resulting in the v-dependent phase $\delta_{v\boldsymbol{k}_{\mathrm{e}}}$ by which the intrinsic phase is given as defined in Eqs. (3.8) and (3.9). Although the intrinsic phase originates from the phase of the photoelectron wave function, it is correlated with the coherent motion of H_2^+. Therefore, in an experiment, the intrinsic phase can be retrieved only by the measurement of the vibrational motion of H_2^+ by a pump–probe method as shown below.

3.2.3 Probe process

After a certain time delay τ, the probe VUV pulse excites H_2^+ to the $2p\sigma_{\mathrm{u}}$ state and the kinetic energy ω^u of the photofragment H^+, produced via the dissociation, is measured. When the field-free Hamiltonian for H_2^+ is denoted as H_{ion}, the dissociating state satisfies the Schrödinger equation, $H_{\mathrm{ion}}|\chi^u\phi_{2\mathrm{p}}\rangle = \omega^u|\chi^u\phi_{2\mathrm{p}}\rangle$ and the probability of finding $|\chi^u\rangle$ at a certain time delay τ corresponds to the spectrogram of the kinetic energy release (KER) as a function of the time delay, called the delay–KER spectrogram in Ref. [71]. We have already derived the delay–KER spectrogram in Eq. (2.43) but we will give a slightly different derivation because we now consider a Gaussian for the envelope of the pump and the probe pulses, whose amplitude never vanishes in contrast to the cosine-squared pulse considered in Eq. (2.43). The propagator corresponding to the probe process is given by

$$U_{\mathrm{probe}} = e^{-\mathrm{i}H_{\mathrm{ion}}(T_f - t)} - \mathrm{i}\int_t^{T_f} dt_1 e^{-\mathrm{i}H_{\mathrm{ion}}(T_f - t_1)} z_1 E_2(t_1 - \tau) e^{-\mathrm{i}H_{\mathrm{ion}}(t_1 - t)}, \tag{3.13}$$

where $E_2(t)$ is the electric field of the probe pulse and z_1 is the z coordinate of the electron bound to H_2^+. The amplitude of $E_2(t)$ is assumed to be finite only for $t_1 \in [t, T_f]$ and negligibly small otherwise. The observation of $|\chi^u(\omega^u)\rangle$ is expressed using the projection operator $\Pi_u = |\chi^u\rangle\langle\chi^u|$ as

$$\begin{aligned}&\Pi_u U_{\mathrm{probe}} \rho_{\mathrm{vib}} U_{\mathrm{probe}}^{\dagger} \Pi_u \\ &= |\chi^u\rangle \sum_{v,v'=0}^{v_{\max}} (\rho_{\mathrm{vib}})_{vv'} p_v(\omega^u) p_{v'}^*(\omega^u) \langle\chi^u|,\end{aligned} \tag{3.14}$$

with

$$p_v(\omega^u) = \langle \chi^u | U_{\text{probe}} | \chi_v \rangle$$

$$= -\mathrm{i} \langle \chi^u | z_1 | \chi_v \rangle \int_t^{T_f} dt_1 E_2(t_1 - \tau) e^{-\mathrm{i}\omega^u(T_f - t_1)} e^{-\mathrm{i}\omega_v(t_1 - t)}$$

$$= -\mathrm{i} M_v(\omega^u) e^{-\mathrm{i}\omega^u(T_f - \tau)} e^{-\mathrm{i}\omega_v(\tau - t)} \int_{t-\tau}^{T_f - \tau} dt' E_2(t') e^{\mathrm{i}(\omega^u - \omega_v)t'}$$

$$= -\mathrm{i} M_v(\omega^u) e^{-\mathrm{i}\omega^u(T_f - \tau)} e^{-\mathrm{i}\omega_v(\tau - t)} \int_\infty^\infty dt' E_2(t') e^{\mathrm{i}(\omega^u - \omega_v)t'}$$

$$= -\mathrm{i} M_v(\omega^u) e^{-\mathrm{i}\omega^u(T_f - \tau)} e^{-\mathrm{i}\omega_v(\tau - t)} \tilde{E}_2(\omega^u - \omega_v), \tag{3.15}$$

where $M_v(\omega^u) = \langle \chi^u \phi_{2\mathrm{p}} | z_1 | \chi_v \phi_{1\mathrm{s}} \rangle$ is the transition moment for the transition induced by the probe process and $\tilde{E}_2(\Omega)$ is the Fourier transform of $E_2(t)$. From Eqs. (3.14) and (3.15), the delay–KER spectrogram can be obtained as

$$I(\tau; \omega^u) = \sum_{vv'=0}^{v_{\max}} (\rho_{\text{vib}})_{vv'} p_v(\omega^u) p_{v'}^*(\omega^u)$$

$$= \sum_{vv'=0}^{v_{\max}} e^{-\mathrm{i}\omega_{vv'}t} (\tilde{\rho}_{\text{vib}})_{vv'} M_v(\omega^u) M_{v'}^*(\omega^u) e^{-\mathrm{i}\omega_{vv'}(\tau - t)} \tilde{E}_2(\omega^u - \omega_v) \tilde{E}_2^*(\omega^u - \omega_{v'})$$

$$= \sum_{vv'=0}^{v_{\max}} e^{-\mathrm{i}\omega_{vv'}\tau} (\tilde{\rho}_{\text{vib}})_{vv'} M_v(\omega^u) M_{v'}^*(\omega^u) \tilde{E}_2(\omega^u - \omega_v) \tilde{E}_2^*(\omega^u - \omega_{v'})$$

$$= \sum_{vv'=0}^{v_{\max}} e^{-\mathrm{i}(\omega_{vv'}\tau - \Delta_{vv'})} |(\tilde{\rho}_{\text{vib}})_{vv'}| M_v(\omega^u) M_{v'}^*(\omega^u) \tilde{E}_2(\omega^u - \omega_v) \tilde{E}_2^*(\omega^u - \omega_{v'})$$

$$= \sum_{vv'=0}^{v_{\max}} e^{-\mathrm{i}\omega_{vv'}(\tau - \tau_{vv'})} |(\tilde{\rho}_{\text{vib}})_{vv'}| M_v(\omega^u) M_{v'}^*(\omega^u) \tilde{E}_2(\omega^u - \omega_v) \tilde{E}_2^*(\omega^u - \omega_{v'}). \tag{3.16}$$

As long as $M_v(\omega^u)$ and $\tilde{E}_2(\Omega)$ are known, $\tau_{vv'}$ can be extracted from the delay–KER spectrogram. In order to determine $\tau_{vv'}$, it is necessary to determine the time delay τ as precisely as possible so that the uncertainty in $\tau_{vv'}$ becomes as small as the magnitude of $\tau_{vv'}$.

3.2.4 Coincidence detection of e^-

By combining the pump–probe measurements with the coincidence detection of e^-, we can make the physical meaning of the intrinsic phase clearer. When the photoelectron momentum is determined to be $\overline{\boldsymbol{k}}_{\mathrm{e}}$, the intrinsic phase is given from Eq. (3.8) as

$$\Delta_{vv'} = \Delta_{vv'}(\overline{\boldsymbol{k}}_{\mathrm{e}}) = \delta_{v\overline{\boldsymbol{k}}_{\mathrm{e}}} - \delta_{v'\overline{\boldsymbol{k}}_{\mathrm{e}}}, \tag{3.17}$$

which shows explicitly that the intrinsic phase varies as a function of $\overline{\boldsymbol{k}}_{\mathrm{e}}$. From Eq. (3.17), the intrinsic phase can be understood as the relative phase between two photoelectrons having the same momentum but being exposed to different ionic potentials. It should be noted that the intrinsic time delay can only be interpreted as the time delay appearing in the vibrational motion of H_2^+ while the intrinsic phase can be interpreted as the phase originating from the photoelectron.

3.3 Results and discussion

3.3.1 Phase and time delay

First, we adopt an attosecond pulse train (APT) expressed as the sum of the Gaussian intensity distribution of the respective harmonics in the frequency domain. We assume that the three harmonics (11th, 13th, 15th) in the APT contribute to the ionization, that is, the Fourier transform of the pump pulse is given as

$$\tilde{E}_1(\Omega) = \sum_{n=11,13,15} \tilde{E}_1^{(n)} = \sum_{n=11,13,15} a_n e^{-b_n(\Omega - c_n)^2}, \tag{3.18}$$

where n represents the harmonic order. We choose the parameters so that they mimic the experimental conditions reported in Ref. [71]. The relative intensity of the harmonic components was set to be $a_{11} = a_{13} = 2a_{15}$. The widths b_n ($n = 11$, 13, and 15) were all set to $4.508 \, \text{fs}^2$, which is equivalent to a full width at half maximum (FWHM) of 0.516 eV. and the frequencies were set to $c_{11} = 17.3$ eV, $c_{13} = 20.5$ eV, and $c_{15} = 23.7$ eV, corresponding to 72, 60, and 52 nm, respectively. We also calculated the phase and the time delay by using the respective harmonic components $\tilde{E}_1^{(n)}$ ($n = 11$, 13, and 15). Because of the narrow bandwidths of the harmonic components in the APT, $|(\tilde{\rho}_{\text{vib}})_{v,v'}|$ is so small for $|v - v'| > 1$ that $\Delta_{vv'}$ could not be extracted from the delay–KER spectrogram with an acceptable uncertainty, and therefore we concentrate on the analysis of $\Delta_{v,v+1}$.
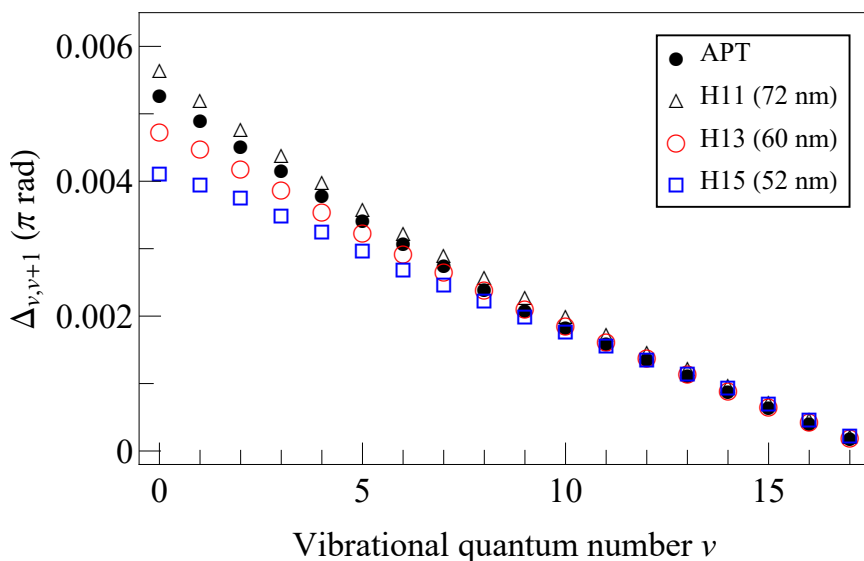
Figure 3.1: The intrinsic phase of the reduced density matrix between the vth state and the $(v + 1)$th state, $\Delta_{v,v+1}$.

As shown in Fig. 3.1, the intrinsic phase between the vth state and the $(v + 1)$th state decreases as v increases, which can be explained in terms of the variation of the vibrational wave functions, $\chi_v(R)$ and $\chi_{v+1}(R)$, of H_2^+. Because the vibrational wave function of neutral H_2, $\chi_0^{H_2}(R)$, almost vanishes for $R < 0.9$ a.u. or 2.2 a.u. $< R$, only the integrand in the range of 0.9 a.u. $\leq R \leq 2.2$ a.u. contributes in Eq. (3.5). As long as
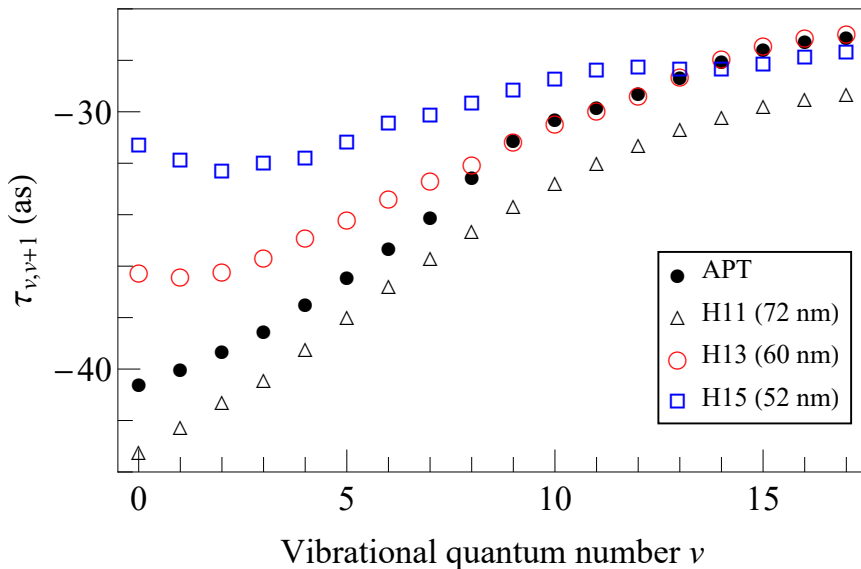
Figure 3.2: The intrinsic time delay between the vth state and the $(v+1)$th state, $\tau_{v,v+1}$.

v takes a sufficiently large value so that the shapes of the vibrational wave functions of H_2^+ of the adjacent levels, $\chi_v(R)$ and $\chi_{v+1}(R)$, become close to each other in the range of 0.9 a.u. $\leq R \leq 2.2$ a.u., the relative phase between M_{v,k_e} and $M_{(v+1),k_e}$, i.e., $\delta_{v,k_e} - \delta_{(v+1),k_e}$, becomes smaller as v increases, which results in the decrease in $\Delta_{v,v+1}$ as v increases.

In the intrinsic time delay for the APT in Fig. 3.2, the contribution from H15 is smaller than the contributions from the other two components, H11 and H13, not only because its peak amplitude is half of the other two, i.e., $a_{11} = a_{13} = 2a_{15}$, but because the amplitude of the transition moment $|M_{vk_e}|$ decreases as k_e increases. For example, when the angle is $\theta_e = 0.2\pi$ rad and the k_e's are chosen such as $k_e^2/2 = c_n - (\omega_v - \omega_0^{H_2})$ $(n = 11, 13, 15)$, the transition moment becomes $|M_{v=0,k_e}| = 0.772$, 0.406, and 0.266 a.u. for H11, H13, and H15, respectively.

As shown in Fig. 3.2, $\tau_{v,v+1}$ for the APT steeply increases at around $v = 8$. Because the central wavelength of H11 is almost resonant at $v = 8$, only a small fraction of H11 has a sufficiently high photon energy to populate the vibrational states in the range of $v \geq 9$. Therefore, $\tau_{v,v+1}$ $(v \geq 9)$ for the APT is dominantly composed of H13.

As shown in Fig. 3.2, the intrinsic time delay $\tau_{v,v+1}$ is in the range between -43 and -27 as. In Refs. [71], in which pump–probe measurements were performed using a pair of attosecond pulse trains, the uncertainty of the pump–probe time delay was about 80 as. We consider that the required uncertainty of 27 as is within the range of future experiments.

3.3.2 Phase and time delay: Coincidence detection of e^-

When the APT or one of its harmonic components is used as the pump pulse and the delay–KER spectrogram is obtained in coincidence with the photoelectron momentum measurement, only a few of $(\tilde{\rho}_{vib})_{v,v+1}$ can be extracted from the delay–KER spectrogram

because of the narrow bandwidth of the pump pulse. For example, when H13 is used as the pump pulse and the photoelectron energy is determined to be $\omega_{k_e} = k_e^2/2 = 4.082$ eV, $|(\tilde{\rho}_{vib})_{v,v+1}|$ almost vanishes except when $v = 2, 3, 4,$ and 5. In order that $(\tilde{\rho}_{vib})_{v,v+1}$ for all v are obtained, the bandwidth of the pump pulse should be larger than the largest energy gap, $\omega_{0,18} = 2.648$ eV, between $v = 0$ and $v = 18$. Therefore, we calculate the intrinsic phases of the reduced density matrices as well as the intrinsic time delays using an XUV pump pulse whose central frequency and bandwidth (FWHM) are c_{13} and $\omega_{0,18}$, respectively, as described below.
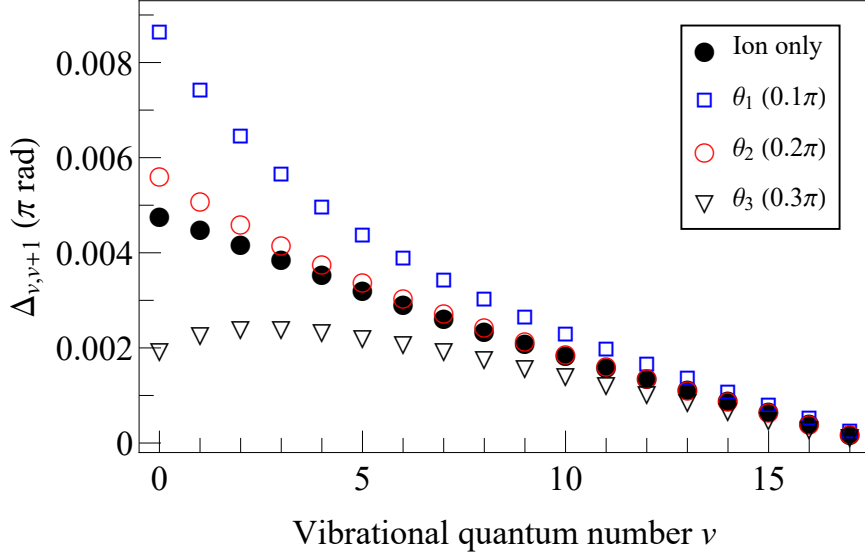
Figure 3.3: The intrinsic phase of the reduced density matrix between the vth and the $(v+1)$th state, $\Delta_{v,v+1}$ for the ultrashort XUV pulse whose central frequency and bandwidth (FWHM) are c_{13} and $\omega_{0,18}$, respectively. The intrinsic phase obtainable by the pump–probe (filled circle) is compared with that obtainable by the pump–probe with the coincidence detection of e^-. Three detection angles are examined; $\theta_1 = 0.1\pi$ rad (red circle), $\theta_2 = 0.2\pi$ rad (triangle), and $\theta_3 = 0.3\pi$ rad (blue square). The kinetic energy is $\omega_{max} = 4.354$ eV for all three cases.

In Fig. 3.3, the intrinsic phase defined by Eq. (3.9) is compared with that defined by Eq. (3.17) in which the photoelectron energy and its ejection angle are determined by the coincidence detection of e^-. When the ion is detected with no coincidence detection of e^-, the intrinsic phase is given by the integral in Eq. (3.8) while it is given by the integrand at a specific vector $\boldsymbol{k}_e$ when e^- is detected in coincidence. Because of the volume element in Eq. (3.8), $d\boldsymbol{k}_e = dk_e k_e^2 d\theta_e \sin\theta_e$, the integrand takes the largest value when $\omega_{k_e} = \omega_{max} = \overline{k}_e^2/2 = 4.354$ eV and $\overline{\theta}_e = \theta_2 = 0.2\pi$ rad. Indeed, as shown in Fig. 3.3, $\Delta_{v,v+1}$ obtained at (θ_2, ω_{max}) (red circle) is close to the one obtained when only the ion is detected (solid circle). When $\overline{\theta}_e = \theta_1 = 0.1\pi$ rad (blue square) and $\overline{\theta}_e = \theta_3 = 0.3\pi$ rad (triangle), the magnitude of the integrands is about 70% of that at $\overline{\theta}_e = \theta_2$. The intrinsic time delays for the three different $\overline{\theta}_e$ values are plotted as shown in Fig. 3.4.

As shown in Fig. 3.3, $\Delta_{v,v+1}$ obtained for θ_1 is larger than the "ion only" case while that obtained for θ_3 is smaller than the "ion only" case. We confirmed that, in the range
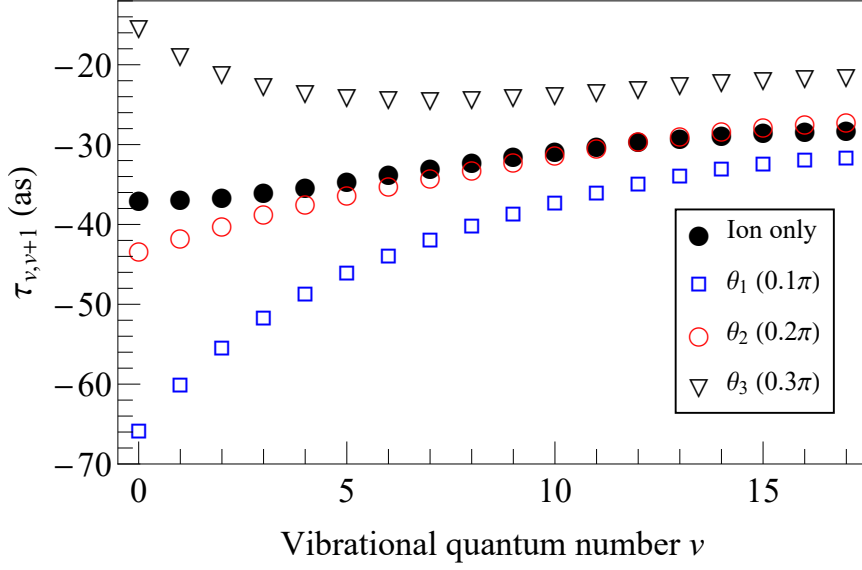
Figure 3.4: The intrinsic time delay derived from Fig. 3.3. Three detection angles are examined; $\theta_1 = 0.1\pi$ rad (red circle), $\theta_2 = 0.2\pi$ rad (triangle), and $\theta_3 = 0.3\pi$ rad (blue square). The kinetic energy is $\omega_{\max} = 4.354$ eV for all three cases.

of $0\,\text{rad} < \overline{\theta}_\text{e} < \pi/2\,\text{rad}$, $\Delta_{v,v+1}$ decreases monotonically as $\overline{\theta}_\text{e}$ increases. Therefore, in the integration over the photoelectron ejection angle, the amount of the increase in the range of $\overline{\theta}_\text{e} < \theta_2$ and that of the decrease in the range of $\theta_2 < \overline{\theta}_\text{e}$ cancel each other out, and $\Delta_{v,v+1}$ obtained after integration, represented by the "ion only" case, becomes very close to $\Delta_{v,v+1}$ obtained for $\overline{\theta}_\text{e} = \theta_2$.

In Fig. 3.5(a), we show the phase of the transition moment, $\delta_{v k_\text{e}} = \arg[M_{v k_\text{e}}]$, as a function of $\omega_{k_\text{e}} = k_\text{e}^2/2$ at $\overline{\theta}_\text{e} = \theta_2$ for two cases of $v = 2$ and 3, because we confirmed that $|(\rho_\text{vib})_{2,3}|$ takes the maximum value among the $|(\rho_\text{vib})_{v,v+1}|$ values. We find that $\delta_{v k_\text{e}}(v = 0, 1, ..., 18)$ increases rapidly as the kinetic energy of the photoelectron increases in the low kinetic energy region and tends to converge to about 0.4π in a similar manner as δ_{2,k_e} and δ_{3,k_e} shown in Fig. 3.5(a). However, the magnitude of the intrinsic phase between the vth and the $(v+1)$th states, $\delta_{v,k_\text{e}} - \delta_{v+1,k_\text{e}}$, is smaller than $10^{-2}\pi$ rad as shown in Fig. 3.3. For example, at $\overline{\theta}_\text{e} = \theta_2$, as the photoelectron kinetic energy increases from 1.088 to 2.993 eV, δ_{2,k_e} and δ_{3,k_e} increase by about 0.5π as shown in Fig. 3.5 (a) while the intrinsic phase, $\Delta_{2,3} = \delta_{2,k_\text{e}} - \delta_{3,k_\text{e}}$, decreases only by 0.000640π.

3.3.3 Effect of the chirp of the pump pulse

If a chirped pulse is used for the pump pulse, the intrinsic phase is given as $\Delta_{vv'} = \delta_{v\overline{k}_\text{e}} - \delta_{v'\overline{k}_\text{e}} + \delta_{v\overline{k}_\text{e}}^E - \delta_{v'\overline{k}_\text{e}}^E$, where $\delta_{v\overline{k}_\text{e}}^E = \arg[\tilde{E}_1(\omega_v + \omega_{\overline{k}_\text{e}} - \omega_g)]$. In the case of a linearly chirped pulse, the chirp rate, χ, is defined as $E_1(t) = f(t)\cos(\omega t + \chi t^2)$, where $f(t)$ is the Gaussian envelope. For $\chi = 42$ fs^{-2} chosen as a typical experimental value [81], the relative phase between $v = 2$ and $v + 1 = 3$ ascribed to the phase of the pump pulse, $\delta_{2,\overline{k}_\text{e}}^E - \delta_{3,\overline{k}_\text{e}}^E$, is 0.00145π, which is comparable to the intrinsic phase shown in Fig. 3.3.
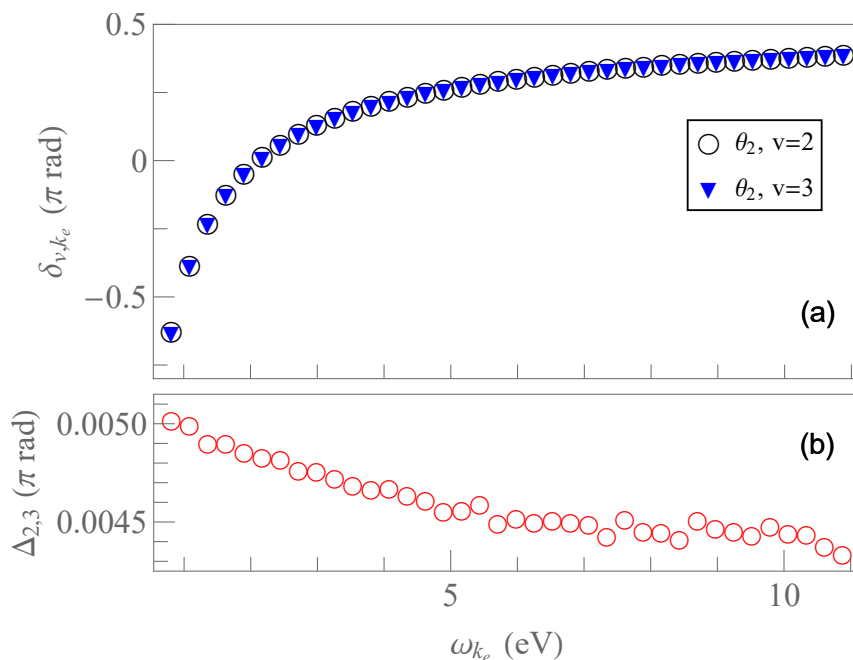
Figure 3.5: The phase of the transition amplitude for $v = 2$ and 3 for the detection angle $\overline{\theta}_{\mathrm{e}} = \theta_2$ (upper panel) and their difference, $\Delta_{2,3} = \delta_{2,k_{\mathrm{e}}} - \delta_{3,k_{\mathrm{e}}}$ (lower panel).

Therefore, it is crucial to use the Fourier-limited pulse or characterize the chirp rate of the pump pulse precisely.

3.3.4 Relation to Wigner delay

The effect of the different ionic potentials on the photoelectron dynamics was discussed in the investigation of the time delay in the photoionization of He [19] and H_2 [20]. With the attosecond streaking of photoelectrons or the RABBITT measurement of photoelectrons, the Wigner delay can be extracted as an intrinsic property of the ionization process after the effect of the probe field is properly subtracted. The Wigner delay $\tau_{vk_{\mathrm{e}}}^{\mathrm{W}}$ is defined using the phase of the transition moment $\delta_{vk_{\mathrm{e}}}$ as

$$\tau_{vk_{\mathrm{e}}}^{\mathrm{W}} = \left.\frac{d\delta_{vk_{\mathrm{e}}}}{d\omega_{k_{\mathrm{e}}}}\right|_{\omega_{\overline{k}_{\mathrm{e}}}}, \tag{3.19}$$

where $\omega_{k_{\mathrm{e}}} = k_{\mathrm{e}}^2/2$. While the difference in the Wigner delay between the vth state and the v'th state gives the difference in the phase derivative, the intrinsic phase defined in Eq. (3.17) gives the difference in the phase itself. In contrast to the Wigner delay, which is obtained by the measurement of the momentum of a photoelectron, the intrinsic time delay can be obtained by the measurement of the KER of the fragment ion. This means that the phase of the photoelectron can also be retrieved by the measurement of the remaining ion because of the non-locality of the total wave function of $H_2^+ + e^-$.

In the present study, we assume that two protons are located on the z axis and that the laser polarization direction is parallel to the z axis, that is, we neglect the

rotational motion of H_2^+. In order to discuss the effect of the molecular rotation, we need to consider all the alignment angles of the molecular axis with respect to the laser polarization direction. Consequently, the transition moment $\mu_{\boldsymbol{k}_e}$ depends on the alignment angle and the reduced density matrix depends not only on the vibrational quantum numbers but also on the rotational quantum numbers.

3.4 Conclusion

We have investigated theoretically the intrinsic phase of the reduced density matrix of the vibrational state of H_2^+ created through the ionization $\Delta_{vv'}$ and clarified the effect originating from the phase of the photoelectron wave function. We have proposed the pump–probe method by using the APT to obtain the reduced density matrix, whose phase appears as the time delay $\tau_{vv'}$ of the vibrational motion of H_2^+ in the delay–KER spectrogram. The intrinsic time delay $\tau_{vv'}$ is evaluated to be of the order of tens of attoseconds. Therefore, the phase of the photoelectron, which has not been considered before in the determination of the reduced density matrix, should be taken into account when the pump–probe time delay is determined with precision of the order of tens of attosseconds.

We have also proposed the pump–probe method by using an ultrashort XUV pulse with the coincidence detection of e^-. The intrinsic phase obtained by the coincidence detection gives the relative phase of the photoelectrons having the same momentum, but experiencing different ionic potentials.

Chapter 4

Molecule in a plasmonic nanocavity

Recent development in nanometer scale fabrication of metal enables us to make a nanocavity. If we place a molecule in the nanocavity and irradiate the nanocavity with light, the molecule starts to oscillate but in a different way from that without the cavity. This is because the electromagnetic field is confined in a very small volume so that the spontaneous emission rate is strongly modified, which is called Purcell enhancement.

The molecular dynamics for the nanocavity with low-loss rate has been investigated in the literature but less attention has been paid to that with high-loss rate, which can be the case in the experiment. In this chapter, I will present an analytical formula to describe the molecular dynamics in the high-loss cavity and show that the spontaneous emission rate depends not only on the population of the excited state but also on the coherence between ground and excited states.

4.1 Molecule–photon coupling in a nanocavity

4.1.1 Plasmonic nanocavity

A quantum emitter placed in an optical cavity resonant to the transition frequency experiences the enhancement of spontaneous emission called the Purcell enhancement due to the increase of the density of states of the electromagnetic field. Because the Purcell factor P, the ratio of the spontaneous emission rate in the cavity to that in the vacuum, is proportional to the cavity quality factor Q (a measure of photon storage time in the cavity) and the inverse of the mode volume V, one can make it large by either reducing the loss of photons or the cavity volume. For example, when a dye molecule is placed in an micrometer-scale optical cavity whose Q is as high as 10^5, the Purcell factor as high as 38 is realized [82].

On the other hand, recent experimental developments enable us to make nanoscale cavities [21–25] by placing a nanoparticle on metal surface, which is called the nanoparticle-on-mirror (NPoM) system. Because the surface plasmon-polariton mode is localized in the gap between the nanoparticle and the metal surface, the NPoM system realizes the plasmonic nanocavity, which can confine the electromagnetic field in the volume smaller than the diffraction limit. In Ref. [21], even though the Q is as small as 15.9, it has been shown that the cavity volume achieves less than $40\,\mathrm{nm}^3$ and the Purcell factor for a dye molecule is as high as 10^6. Considering the relation $\gamma_\mathrm{c} = \omega_\mathrm{c}/Q$, where ω_c is the mode frequency and γ_c is the cavity decay rate, the small Q of NPoM is a preferable property for making a high-repetition single-photon emitter [25], which can emit single photons before the decoherence proceeds in the quantum emitter. Such confinement of the electromagnetic field also leads to fast energy transfer between the molecule and the cavity mode and if its oscillation frequency Ω_0 (called the vacuum Rabi frequency) is larger than the cavity decay rate γ_c, the molecule and photon forms a polariton. In this so-called strong coupling regime, the potential energy surface (PES) of the molecule is strongly modified leading to the possibility of control of chemical reactions [83–85].

The rate of photon emission also depends on the nuclear motion because the resonant frequency of the electronic transition depends on the nuclear position and therefore the Purcell enhancement only occurs in the vicinity of a certain nuclear position where the cavity mode is resonant with the electronic transition. In a recent theoretical study [86], it has been shown that, after the cavity mode is pumped by a short laser pulse, the rate of photon emission from the cavity reflects the nuclear motion on the PES so that the nuclear motion can be monitored only by measuring the emitted photon instead of irradiating the molecule with a probe pulse.

Especially in the weak coupling regime, where $\Omega_0 < \gamma_\mathrm{c}$, the cavity mode is dumped rapidly so that we can eliminate the fast evolution and describe the molecular dynamics only by considering the Hilbert space for the slower evolution, which reduces the size of the problem as well as gives insight into the evolution of the molecule. Ref. [87] derived effective operators describing such slow dynamics in the absence of internal degrees of freedom, e.g., nuclear vibration, which is relevant in our case. In this chapter, we derive the effective operators describing the slow dynamics of the molecule in the plasmonic nanocavity and give an analytical expression for the rate of photon emission by eliminating a fast-evolving state. We solve the master equation by the Monte Carlo wave packet

(MCWP) method [27,88], which can reduce the computational cost compared with solving the master equation for the full density matrix. In the MCWP method, we first describe the evolution of a wave packet in the absence of decay by adding a non-Hermitian term to the Hamiltonian and then introduce quantum jumps at random times to account for the decay process. For example, in a recent theoretical study, the MCWP method has been successfully applied to simulate the photon emission signal from a fluorophore [89]. Atomic units (a.u.) are used unless otherwise indicated.

4.1.2 Master equation for a cavity–molecule system

We consider a single-mode nanocavity containing a molecule with two electronic states, i.e., the ground X and the first excited A states. The Hamiltonian describing the system pumped by the laser field $E_0(t) \cos \omega_{\mathrm{L}} t$ reads [86]

$$
\begin{aligned}
H = {} & T + \omega_{\mathrm{XA}} + \omega_{\mathrm{v}} \frac{R^2}{2} - \lambda_{\mathrm{v}} \sqrt{2\omega_{\mathrm{v}}} \sigma^+ \sigma^- R \\
& + \omega_{\mathrm{c}} a^\dagger a + \frac{\Omega_0}{2} \left(a^\dagger \sigma^- + a \sigma^+ \right) + \mu_{\mathrm{c}} E_0(t) \cos \omega_{\mathrm{L}} t \left(a^\dagger + a \right),
\end{aligned}
\tag{4.1}
$$

where σ^+ (σ^-) is the creation (annihilation) operator for the electronic state whose excitation frequency is ω_{XA}, R is the mass-weighted nuclear position for the vibrational mode with the frequency ω_{v} and the electron–phonon coupling λ_{v}, and T is the nuclear kinetic energy operator. The cavity mode is described by the photon annihilation (creation) operator a ($a^\dagger$) and pumped by the laser field through the coupling constant μ_{c}. The cavity mode frequency is chosen as resonant with the electronic excitation, i.e., $\omega_{\mathrm{c}} = \omega_{\mathrm{XA}}$. The cavity–molecule coupling is described by the vacuum Rabi frequency Ω_0 within the rotating wave approximation. Here, Ω_0 is assumed to be independent on R because the nuclear motion on the electronic ground state is localized around $R = 0$ in the present study. In order to concentrate on analysing the molecular dynamics induced by the cavity, we neglect the laser–molecule coupling.

By expressing the nuclear degree of freedom using the position basis, $|R\rangle$, the Hamiltonian in a frame rotating at the laser frequency ω_{L} is given as

$$
\begin{aligned}
H - T = {} & \int dR \Big[V_{\mathrm{X}} \, |\mathrm{X}0, R\rangle \, \langle \mathrm{X}0, R| + (V_{\mathrm{A}} - \omega_{\mathrm{L}}) \, |\mathrm{A}0, R\rangle \, \langle \mathrm{A}0, R| \\
& + (V_{\mathrm{X}} + \omega_{\mathrm{c}} - \omega_{\mathrm{L}}) \, |\mathrm{X}1, R\rangle \, \langle \mathrm{X}1, R| \\
& + \frac{\mu_{\mathrm{c}} E_0(t)}{2} \left(|\mathrm{X}1, R\rangle \, \langle \mathrm{X}0, R| + |\mathrm{X}0, R\rangle \, \langle \mathrm{X}1, R| \right) \\
& + \frac{\Omega_0}{2} \left(|\mathrm{X}1, R\rangle \, \langle \mathrm{A}0, R| + |\mathrm{A}0, R\rangle \, \langle \mathrm{X}1, R| \right) \Big],
\end{aligned}
\tag{4.2}
$$

where the rotating wave approximation is employed. The PESs for the electronic ground and the excited states are given by

$$
V_{\mathrm{X}} = \omega_{\mathrm{v}} \frac{R^2}{2}, \quad V_{\mathrm{A}} = \frac{\omega_{\mathrm{v}}^2}{2} \left(R - \frac{\lambda_{\mathrm{v}} \sqrt{2\omega_{\mathrm{v}}}}{\omega_{\mathrm{v}}^2} \right)^2 - \frac{\lambda_{\mathrm{v}}^2}{\omega_{\mathrm{v}}}.
\tag{4.3}
$$

The basis sets explicitly depend on the internuclear distance such as $|\mathrm{X}0, R\rangle$, and we call them "the continuous bases". The nuclear degree of freedom can also be expressed by the vibrational eigenfunctions $\{|\chi_v^{\mathrm{X}}\rangle, |\chi_v^{\mathrm{A}}\rangle\}$ so that the Hamiltonian is given by

$$
\begin{aligned}
H = &\sum_v \omega_v^{\mathrm{X}} |\mathrm{X}0, v\rangle \langle \mathrm{X}0, v| + \sum_v (\omega_v^{\mathrm{A}} - \omega_{\mathrm{L}}) |\mathrm{A}0, v\rangle \langle \mathrm{A}0, v| \\
&+ \sum_v (\omega_v^{\mathrm{X}} + \omega_{\mathrm{c}} - \omega_{\mathrm{L}}) |\mathrm{X}1, v\rangle \langle \mathrm{X}1, v| \\
&+ \frac{\mu_{\mathrm{c}} E_0(t)}{2} \sum_v (|\mathrm{X}1, v\rangle \langle \mathrm{X}0, v| + |\mathrm{X}0, v\rangle \langle \mathrm{X}1, v|) \\
&+ \frac{\Omega_0}{2} \sum_{v,v'} S_{vv'}(|\mathrm{X}1, v\rangle \langle \mathrm{A}0, v'| + |\mathrm{A}0, v'\rangle \langle \mathrm{X}1, v|),
\end{aligned}
\tag{4.4}
$$

where $S_{vv'} = \langle \chi_v^{\mathrm{X}}|\chi_{v'}^{\mathrm{A}}\rangle$ are the Frank–Condon factors and $|\mathrm{X}0, v\rangle$ is the shorthand for $|\mathrm{X}0\rangle |\chi_v^{\mathrm{X}}\rangle$, which we call "the discrete bases".

The dissipation is characterized by the cavity decay rate γ_{c}, which is chosen large so that the spontaneous emission from the molecule can be neglected. Then, the master equation of Lindblad form is given in the Schrödinger picture as

$$
\dot{\rho}^S = -\mathrm{i}[H, \rho^S] - \frac{1}{2}\left(L^\dagger L \rho^S + \rho^S L^\dagger L\right) + L\rho^S L^\dagger, \quad L = \sqrt{\gamma_{\mathrm{c}}}a.
\tag{4.5}
$$

The Lindbladian L is given in the continuous basis as

$$
L = \sqrt{\gamma_{\mathrm{c}}} \int dR |\mathrm{X}0, R\rangle \langle \mathrm{X}1, R|,
\tag{4.6}
$$

while in the discrete basis as

$$
L = \sqrt{\gamma_{\mathrm{c}}} \sum_v |\mathrm{X}0, v\rangle \langle \mathrm{X}1, v|.
\tag{4.7}
$$

The parameters characterizing the molecule and the cavity are chosen the same as Ref. [86], i.e., $\omega_{\mathrm{XA}} = \omega_{\mathrm{c}} = 3.5\,\mathrm{eV}$, $\omega_{\mathrm{v}} = 0.182\,\mathrm{eV}$, $\lambda_{\mathrm{v}} = 0.192\,\mathrm{eV}$, while the coupling strength and the decay rate is chosen to describe the weak-coupling regime, i.e., $\Omega_0 < \gamma_{\mathrm{c}}$.

Because of the fast cavity decay, the number of photon in the cavity is only one at most so that we can describe the coupled molecule–cavity system by three states, i.e., $|\mathrm{X}0\rangle$, $|\mathrm{A}0\rangle$, and $|\mathrm{X}1\rangle$, where X and A denote the electronic ground and the excited states, respectively, 0 and 1 the number of photon. Because we consider only one vibrational mode on each electronic state, the time-evolution of the system can be fully described by the nuclear motion on the three PESs shown in Fig. 4.1.

4.1.3   Effective master equation

As long as the cavity decay is faster than the vacuum Rabi oscillation, we can eliminate the fast-evolving state, $|\mathrm{X}1\rangle$, as a good approximation and describe the system only using the comparably slow-evolving states, $|\mathrm{X}0\rangle$ and $|\mathrm{A}0\rangle$. In order to derive the effective
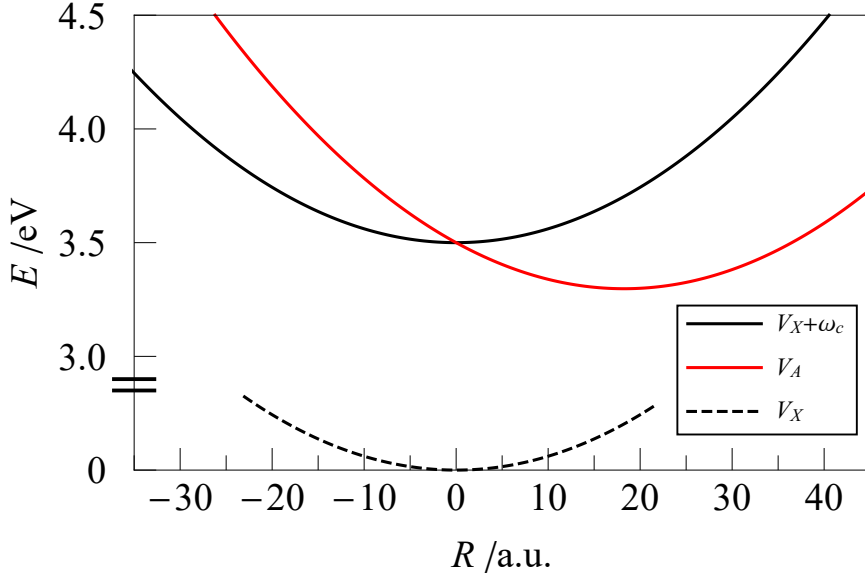
Figure 4.1: The potential energy surfaces (PESs) for the electronic ground state $|X0\rangle$ (black dashed), the excited state $|A0\rangle$ (red solid), and the electronic ground state with a single excitation of the cavity mode $|X1\rangle$ (black solid). The PESs are characterized by the parameters ω_{XA}, ω_c, ω_v, and λ_v given in the text.

master equation describing the slow dynamics, we employ the effective operator method developed in Ref. [87], which is based on the second order perturbation theory.

First, the total system is divided into two subspaces, the fast-evolving states denoted as the excited states and the slow-evolving states denoted as ground states. In the present case, the excited state and the ground states are composed of $|X1\rangle$ and of $\{|X0\rangle, |A0\rangle\}$, respectively, by which the projection operators, $P_e = |X1\rangle \langle X1|$ and $P_g = |X0\rangle \langle X0| + |A0\rangle \langle A0|$ are defined. By treating the laser–cavity ($\mu_c E(t)$) and the molecule–cavity (Ω_0) couplings up to the second order, we can derive an effective master equation for the ground state density operator, $\rho_g^S = P_g \rho^S P_g$. Details of the derivation are given in Appendices B.1 and B.2.

The effective master equation is given as

$$\dot{\rho}_g^S = -\mathrm{i} \left\{ H_{\mathrm{eff}}^{\mathrm{NH}} \rho_g^S - \rho_g^S (H_{\mathrm{eff}}^{\mathrm{NH}})^\dagger \right\} + L_{\mathrm{eff}}^S \rho_g^S (L_{\mathrm{eff}}^S)^\dagger, \tag{4.8}$$

where the effective non-Hermitian Hamiltonian and the effective Lindbladian are given in

the continuous basis as

$$
\begin{aligned}
H_{\text{eff}}^{\text{NH}} = T + \int dR \Bigg[& \left(V_X - \frac{(\mu_c E_0)^2}{4} \frac{1 - e^{-i(\omega_c - \omega_L - i\gamma_c/2)(t-t_0)}}{\omega_c - \omega_L - i\gamma_c/2} \right) |X0, R\rangle \langle X0, R| \\
& + \left(V_A - \omega_L - \frac{\Omega_0^2}{4} \frac{1 - e^{-i(V_X + \omega_c - V_A - i\gamma_c/2)(t-t_0)}}{V_X + \omega_c - V_A - i\gamma_c/2} \right) |A0, R\rangle \langle A0, R| \\
& - \frac{\Omega_0 \mu_c E_0}{4} \Bigg\{ \frac{1 - e^{-i(\omega_c - \omega_L - i\gamma_c/2)(t-t_0)}}{\omega_c - \omega_L - i\gamma_c/2} |A0, R\rangle \langle X0, R| \\
& + \frac{1 - e^{-i(V_X + \omega_c - V_A - i\gamma_c/2)(t-t_0)}}{V_X + \omega_c - V_A - i\gamma_c/2} |X0, R\rangle \langle A0, R| \Bigg\} \Bigg]
\end{aligned}
\tag{4.9}
$$

$$
\begin{aligned}
L_{\text{eff}}^S = -i\sqrt{\gamma_c} e^{i(\omega_c - \omega_L)t} \int dR \Bigg[& \frac{\mu_c E_0}{2} \frac{1 - e^{-i(\omega_c - \omega_L - i\gamma_c/2)(t-t_0)}}{\omega_c - \omega_L - i\gamma_c/2} |X0, R\rangle \langle X0, R| \\
& + \frac{\Omega_0}{2} \frac{1 - e^{-i(V_X + \omega_c - V_A - i\gamma_c/2)(t-t_0)}}{V_X + \omega_c - V_A - i\gamma_c/2} |X0, R\rangle \langle A0, R| \Bigg],
\end{aligned}
\tag{4.10}
$$

where the initial state is given at t_0. In the continuous basis, it is clear that the decay rate is R dependent. The R-dependent denominator in Eq. (4.10), $V_X + \omega_c - V_A - i\gamma_c/2$, means that the decay rate becomes large when the internuclear distance R is close to the minimum point of the detuning $V_X + \omega_c - V_A$, which corresponds to the position-dependent Purcell enhancement of decay rate discussed in [86].

It has been known from the study of the adiabatic elimination [90] that, as a good approximation, we can neglect the kinetic energy operator in deriving the effective master equation for the slow-evolving states. Here, we have employed the same procedure: First, the kinetic energy operator is neglected and only the RHS of Eq. (4.2) is considered in deriving the effective master equation, and then, the kinetic energy operator is added as Eq. (4.8).

In the discrete basis, the effective master equation is given with the following effective

operators

$$
\begin{aligned}
H_{\text{eff}}^{\text{NH}} = {} & \left(\sum_v \omega_v^{\text{X}} - \frac{(\mu_{\text{c}} E_0)^2}{4} \frac{1 - e^{-\mathrm{i}(\omega_{\text{c}} - \omega_{\text{L}} - \mathrm{i}\gamma_{\text{c}}/2)(t-t_0)}}{\omega_{\text{c}} - \omega_{\text{L}} - \mathrm{i}\gamma_{\text{c}}/2} \right) |\text{X0}, v\rangle \langle \text{X0}, v| \\
& + \sum_{u'v'} \left\{ (\omega_{u'}^{\text{A}} - \omega_{\text{L}})\delta_{u'v'} \right. \\
& \qquad \left. - \frac{\Omega_0^2}{4} \sum_v S_{vu'} S_{vv'} \frac{1 - e^{-\mathrm{i}(\omega_v^{\text{X}} + \omega_{\text{c}} - \omega_{v'}^{\text{A}} - \mathrm{i}\gamma_{\text{c}}/2)(t-t_0)}}{\omega_v^{\text{X}} + \omega_{\text{c}} - \omega_{v'}^{\text{A}} - \mathrm{i}\gamma_{\text{c}}/2} \right\} |\text{A0}, u'\rangle \langle \text{A0}, v'| \\
& - \frac{\Omega_0 \mu_{\text{c}} E_0}{4} \sum_{vv'} S_{vv'} \left\{ \frac{1 - e^{-\mathrm{i}(\omega_{\text{c}} - \omega_{\text{L}} - \mathrm{i}\gamma_{\text{c}}/2)(t-t_0)}}{\omega_{\text{c}} - \omega_{\text{L}} - \mathrm{i}\gamma_{\text{c}}/2} |\text{A0}, v'\rangle \langle \text{X0}, v| \right. \\
& \qquad \left. + \frac{1 - e^{-\mathrm{i}(\omega_v^{\text{X}} + \omega_{\text{c}} - \omega_{v'}^{\text{A}} - \mathrm{i}\gamma_{\text{c}}/2)(t-t_0)}}{\omega_v^{\text{X}} + \omega_{\text{c}} - \omega_{v'}^{\text{A}} - \mathrm{i}\gamma_{\text{c}}/2} |\text{X0}, v\rangle \langle \text{A0}, v'| \right\},
\end{aligned}
\tag{4.11}
$$

$$
\begin{aligned}
L_{\text{eff}}^S = {} & -\mathrm{i}\sqrt{\gamma_{\text{c}}} e^{\mathrm{i}(\omega_{\text{c}} - \omega_{\text{L}})t} \left[\sum_v \frac{\mu_{\text{c}} E_0}{2} \frac{1 - e^{-\mathrm{i}(\omega_{\text{c}} - \omega_{\text{L}} - \mathrm{i}\gamma_{\text{c}}/2)(t-t_0)}}{\omega_{\text{c}} - \omega_{\text{L}} - \mathrm{i}\gamma_{\text{c}}/2} |\text{X0}, v\rangle \langle \text{X0}, v| \right. \\
& \left. + \sum_{vv'} \frac{\Omega_0}{2} S_{vv'} \frac{1 - e^{-\mathrm{i}(\omega_v^{\text{X}} + \omega_{\text{c}} - \omega_{v'}^{\text{A}} - \mathrm{i}\gamma_{\text{c}}/2)(t-t_0)}}{\omega_v^{\text{X}} + \omega_{\text{c}} - \omega_{v'}^{\text{A}} - \mathrm{i}\gamma_{\text{c}}/2} |\text{X0}, v\rangle \langle \text{A0}, v'| \right].
\end{aligned}
\tag{4.12}
$$

4.1.4 Monte Carlo wave packet method

In solving the master equation Eq. (4.5), we apply the Monte Carlo wave packet (MCWP) method [27], with which we can express the system by the state vector instead of the density matrix, so that we can reduce the computational cost significantly. In the MCWP method, the state vector of the system,

$$
\begin{aligned}
|\Psi(t)\rangle &= |\psi_{\text{X0}}(t)\rangle + |\psi_{\text{A0}}(t)\rangle + |\psi_{\text{X1}}(t)\rangle \\
&= \int dR \{ C_{\text{X0},R}(t) |\text{X0}, R\rangle + C_{\text{A0},R}(t) |\text{A0}, R\rangle + C_{\text{X1},R}(t) |\text{X1}, R\rangle \} \tag{4.13} \\
&= \sum_v \{ C_{\text{X0},v}(t) |\text{X0}, v\rangle + C_{\text{A0},v}(t) |\text{A0}, v\rangle + C_{\text{X1},v}(t) |\text{X1}, v\rangle \}, \tag{4.14}
\end{aligned}
$$

is propagated under the non-Hermitian Hamiltonian,

$$
\begin{aligned}
H^{\mathrm{NH}} &= H - \mathrm{i}L^{\dagger}L/2 \\
&= T + \int dR\,[V_{\mathrm{X}}\,|\mathrm{X0},R\rangle\langle\mathrm{X0},R| + (V_{\mathrm{A}} - \omega_{\mathrm{L}})\,|\mathrm{A0},R\rangle\langle\mathrm{A0},R| \\
&\quad + (V_{\mathrm{X}} + \omega_{\mathrm{c}} - \omega_{\mathrm{L}})\,|\mathrm{X1},R\rangle\langle\mathrm{X1},R| \\
&\quad + \frac{\mu_{\mathrm{c}}E_0(t)}{2}\left(|\mathrm{X1},R\rangle\langle\mathrm{X0},R| + |\mathrm{X0},R\rangle\langle\mathrm{X1},R|\right) \\
&\quad + \frac{\Omega_0}{2}(|\mathrm{X1},R\rangle\langle\mathrm{A0},R| + |\mathrm{A0},R\rangle\langle\mathrm{X1},R|) \\
&\quad + \gamma_{\mathrm{c}}\,|\mathrm{X1},R\rangle\langle\mathrm{X1},R|] \qquad\qquad\qquad (4.15) \\
&= \sum_{v}\omega_v^{\mathrm{X}}\,|\mathrm{X0},v\rangle\langle\mathrm{X0},v| + \sum_{v}(\omega_v^{\mathrm{A}} - \omega_{\mathrm{L}})\,|\mathrm{A0},v\rangle\langle\mathrm{A0},v| \\
&\quad + \sum_{v}(\omega_v^{\mathrm{X}} + \omega_{\mathrm{c}} - \omega_{\mathrm{L}})\,|\mathrm{X1},v\rangle\langle\mathrm{X1},v| \\
&\quad + \frac{\mu_{\mathrm{c}}E_0(t)}{2}\sum_{v}(|\mathrm{X1},v\rangle\langle\mathrm{X0},v| + |\mathrm{X0},v\rangle\langle\mathrm{X1},v|) \\
&\quad + \frac{\Omega_0}{2}\sum_{v,v'}S_{vv'}(|\mathrm{X1},v\rangle\langle\mathrm{A0},v'| + |\mathrm{A0},v'\rangle\langle\mathrm{X1},v|) \\
&\quad + \gamma_{\mathrm{c}}\sum_{v}|\mathrm{X1},v\rangle\langle\mathrm{X1},v| \qquad\qquad\qquad\qquad (4.16)
\end{aligned}
$$

and then, the decrease of the norm, $dp \equiv 1 - \langle\Psi(t+dt)|\Psi(t+dt)\rangle$, during the time propagation from t to $t+dt$, is calculated. Finally, in order to mimic the randomness of the photon detection (or quantum jump in general) in the experiment, a random number ϵ is chosen at each time step. If $\epsilon < dp$ is satisfied at t, the Lindbladian L is applied to the state vector, $L\,|\Psi(t)\rangle$, which means the photon is detected (quantum jump occurs) at t, and if not, $|\Psi(t+dt)\rangle$ is normalized. In the MCWP method, the quantum jump becomes more probable to occur as dp increases, we call dp the jump probability. We call each state vector $|\Psi\rangle$ the trajectory and, by averaging over a large number N of trajectories, we can obtain the density matrix $\rho = 1/N\sum_j^N |\Psi_j\rangle\langle\Psi_j|$ equivalent to that obtained by the numerical integration of Eq. (4.5).

As shown in Fig. 4.2, the results obtained by the numerical integration of Eq. (4.5) is well reproduced by the MCWP method after averaging over 4000 trajectories, and so we call the MCWP method applied to Eq. (4.5) "the exact" method, while we call that applied to Eq. (4.8) "the effective" method. In order to analyse how precisely the effective master equation describes the slow-evolving dynamics, we compare "no-jump dynamics", that is, the time-propagation under the non-Hermitian Hamiltonians, H^{NH} and $H_{\mathrm{eff}}^{\mathrm{NH}}$, while we neglect the quantum jump by fixing the random number ϵ at 1 so that the condition $\epsilon < dp$ never holds.

Because dt is chosen so that the decrease of the norm dp can be described within the
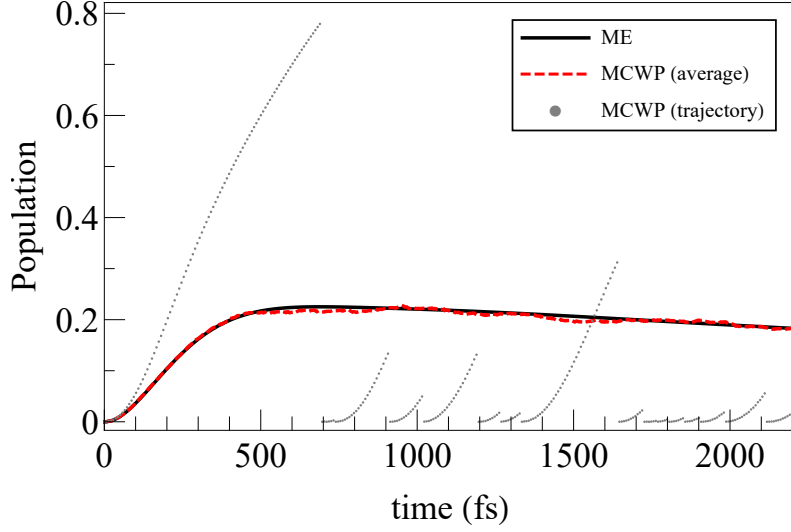
Figure 4.2: The population of the electronic excited state $|A0\rangle$ calculated by the numerical integration of the master equation (ME, solid line) and by the MCWP method (MCWP(average), dashed line). A trajectory (dots) shows abrupt damping at random times, which corresponds to the detection of the photon emitted from the cavity. The parameters for the cavity, the pump laser, and the Rabi frequency is the same as those specified in 4.2.1

first-order term, i.e.,

$$
dp = 1 - \left| \left(1 - \mathrm{i}dt H^{\mathrm{NH}}\right) |\Psi(t)\rangle \right|^2 = \mathrm{i}dt \langle \Psi(t)| \left(H^{\mathrm{NH}} - (H^{\mathrm{NH}})^{\dagger}\right) |\Psi(t)\rangle
$$
$$
= dt \langle \Psi(t)| L^{\dagger}L |\Psi(t)\rangle, \tag{4.17}
$$

which is simplified for the exact method as,

$$
dp = dt\gamma_{\mathrm{c}} \int dR |\langle \mathrm{X}1, R|\Psi(t)\rangle|^2 = dt\gamma_{\mathrm{c}} \int dR |C_{\mathrm{X}1,R}(t)|^2 \,(\text{continuous basis}) \tag{4.18}
$$
$$
= dt\gamma_{\mathrm{c}} \sum_{v} |\langle \mathrm{X}1, v|\Psi(t)\rangle|^2 = dt\gamma_{\mathrm{c}} \sum_{v} |C_{\mathrm{X}1,v}(t)|^2 \,(\text{discrete basis}). \tag{4.19}
$$

The explicit form of dp for the effective method is given in the continuous basis as

$$
dp = \mathrm{i}dt \langle \Psi(t)| \left(H_{\mathrm{eff}}^{\mathrm{NH}} - (H_{\mathrm{eff}}^{\mathrm{NH}})^{\dagger}\right) |\Psi(t)\rangle
$$
$$
= dt \int dR \Bigg[\frac{(\mu_{\mathrm{c}}E_0)^2}{4} \frac{\gamma_{\mathrm{c}}}{|\omega_{\mathrm{c}} - \omega_{\mathrm{L}} - \mathrm{i}\gamma_{\mathrm{c}}/2|^2} |C_{\mathrm{X}0,R}|^2
$$
$$
+ \frac{\Omega_0^2}{4} \frac{\gamma_{\mathrm{c}}}{|V_{\mathrm{X}} + \omega_{\mathrm{c}} - V_{\mathrm{A}} - \mathrm{i}\gamma_{\mathrm{c}}/2|^2} |C_{\mathrm{A}0,R}|^2
$$
$$
+ \frac{\Omega_0 \mu_{\mathrm{c}} E_0}{4} \left\{ \frac{\mathcal{R} - \mathrm{i}\mathcal{I}}{|(\omega_{\mathrm{c}} - \omega_{\mathrm{L}} - \mathrm{i}\gamma_{\mathrm{c}}/2)(V_{\mathrm{X}} + \omega_{\mathrm{c}} - V_{\mathrm{A}} + \mathrm{i}\gamma_{\mathrm{c}}/2)|^2} C_{\mathrm{A}0,R}^* C_{\mathrm{X}0,R} + \text{c.c.} \right\} \Bigg],
$$
$$
\tag{4.20}
$$

60

where $\mathcal{R}$ and $\mathcal{I}$ are defined as

$$\mathcal{R} = \gamma_c \left\{ (\omega_c - \omega_L)(V_X + \omega_c - V_A) + (\gamma_c/2)^2 + (V_X - V_A + \omega_L)^2/2 \right\} \tag{4.21}$$

$$\mathcal{I} = \left\{ (\omega_c - \omega_L)(V_X + \omega_c - V_A) - (\gamma_c/2)^2 \right\} (V_X - V_A + \omega_L), \tag{4.22}$$

while in the discrete basis, dp is given as

$$
\begin{aligned}
dp/dt = & \left(\frac{(\mu_c E_0)^2}{4} \sum_v \frac{\gamma_c}{|\omega_c - \omega_L - i\gamma_c/2|^2} \right) |C_{X0,v}|^2 \\
& + \frac{\Omega_0^2}{4} \sum_v \Bigg\{ \sum_{v'} |S_{vv'}|^2 \frac{\gamma_c}{|\omega_v^X + \omega_c - \omega_{v'}^A - i\gamma_c/2|^2} |C_{A0,v'}|^2 \\
& + \sum_{v' \neq u'} S_{vu'} S_{vv'} \frac{\mathcal{R}_{v'u'}^{AA} - i\mathcal{I}_{v'u'}^{AA}}{|(\omega_v^X + \omega_c - \omega_{v'}^A - i\gamma_c/2)(\omega_v^X + \omega_c - \omega_{u'}^A + i\gamma_c/2)|^2} C_{A0,u'}^* C_{A0,v'} \Bigg\} \\
& + \frac{\Omega_0 \mu_c E_0}{4} \sum_{vv'} S_{vv'} \Bigg\{ \frac{\mathcal{R}_{vv'}^{AX} - i\mathcal{I}_{vv'}^{AX}}{|(\omega_c - \omega_L - i\gamma_c/2)(\omega_v^X + \omega_c - \omega_{v'}^A + i\gamma_c/2)|^2} C_{A0,v'}^* C_{X0,v} \\
& \qquad\qquad + \text{c.c.} \Bigg\},
\end{aligned}
\tag{4.23}
$$

with

$$\mathcal{R}_{v'u'}^{AA} = \gamma_c \left\{ (\omega_v^X + \omega_c - \omega_{v'}^A)(\omega_v^X + \omega_c - \omega_{u'}^A) + (\gamma_c/2)^2 + (\omega_{v'}^A - \omega_{u'}^A)^2/2 \right\}, \tag{4.24}$$

$$\mathcal{I}_{v'u'}^{AA} = \left\{ (\omega_v^X + \omega_c - \omega_{v'}^A)(\omega_v^X + \omega_c - \omega_{u'}^A) - (\gamma_c/2)^2 \right\} (\omega_{v'}^A - \omega_{u'}^A), \tag{4.25}$$

$$\mathcal{R}_{vv'}^{AX} = \gamma_c \left\{ (\omega_c - \omega_L)(\omega_v^X + \omega_c - \omega_{v'}^A) + (\gamma_c/2)^2 + (\omega_v^X - \omega_{v'}^A + \omega_L)^2/2 \right\}, \tag{4.26}$$

$$\mathcal{I}_{vv'}^{AX} = \left\{ (\omega_c - \omega_L)(\omega_v^X + \omega_c - \omega_{v'}^A) - (\gamma_c/2)^2 \right\} (\omega_v^X - \omega_{v'}^A + \omega_L). \tag{4.27}$$

Details of the derivation are given in Appendix B.3.

4.2 Results and discussion

4.2.1 Validity of the effective operator method
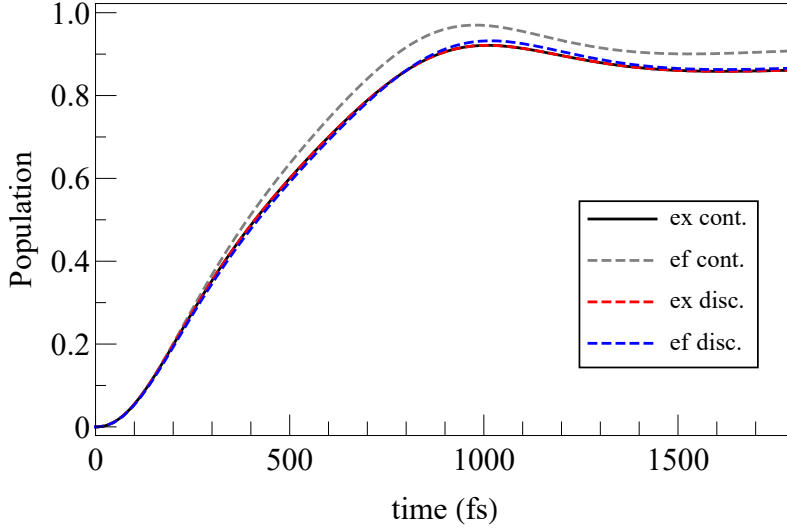
Figure 4.3: The population in $|A0\rangle$ obtained by the exact method is compared with that obtained by the effective method. For the exact method, Eq. (4.5) is solved with H^{NH} in the continuous basis Eq. (4.2) (black solid) and in the discrete basis Eq. (4.4) (red dashed), while for the effective mehod, Eq. (4.8) is solved with $H_{\mathrm{eff}}^{\mathrm{NH}}$ in the continuous basis Eq. (4.9) (gray dashed) and in the discrete basis Eq. (4.11) (blue dashed). The vibrational period and the plasmon lifetime are $2\pi/\omega_{\mathrm{v}} = 23\,\mathrm{fs}$ and $2\pi/\gamma_{\mathrm{c}} = 8\,\mathrm{fs}$, respectively.

First, we examine the validity of the effective operator method. In the following, we compare the no-jump dynamics with "the exact" method and with "the effective" method, which we defined in 4.1.4, by showing the population of the electronic excited state $|A0\rangle$ and the normalized expectation value of R. The latter is defined as

$$\langle R \rangle = \frac{\langle \psi_{\mathrm{A0}}|\, R \,|\psi_{\mathrm{A0}}\rangle}{\langle \psi_{\mathrm{A0}}|\psi_{\mathrm{A0}}\rangle}. \tag{4.28}$$

Some parameters are chosen the same as Ref. [86] as we explained in the paragraph after Eq. (4.5), while the parameters characterizing the coupling are chosen as $\gamma_{\mathrm{c}} = 0.5\,\mathrm{eV}$, $\Omega_0 = 0.05\,\mathrm{eV}$, $\mu_{\mathrm{c}} E_0 = \Omega_0$, $\omega_{\mathrm{c}} - \omega_{\mathrm{L}} = \Omega_0/2$, $t_0 = 0$. Because the decay rate γ_{c} is larger than the cavity–molecule coupling and the laser–cavity coupling, i.e., $\gamma_{\mathrm{c}} > \Omega_0, \mu_{\mathrm{c}} E_0$, the population in $|X1\rangle$ is kept low and consequently, the effective master equation is expected to work.

As shown in Fig. 4.3, the population in $|A0\rangle$ increases until around 1000 fs and it reaches the steady state around 1800 fs. The discrete basis is composed of $v = 0 - 7$ eigenstates for both electronic states X and A. For the exact method, the population obtained using the discrete basis (red dashed) overlaps with that obtained using the continuous basis (black solid). For the effective method, the population obtained using
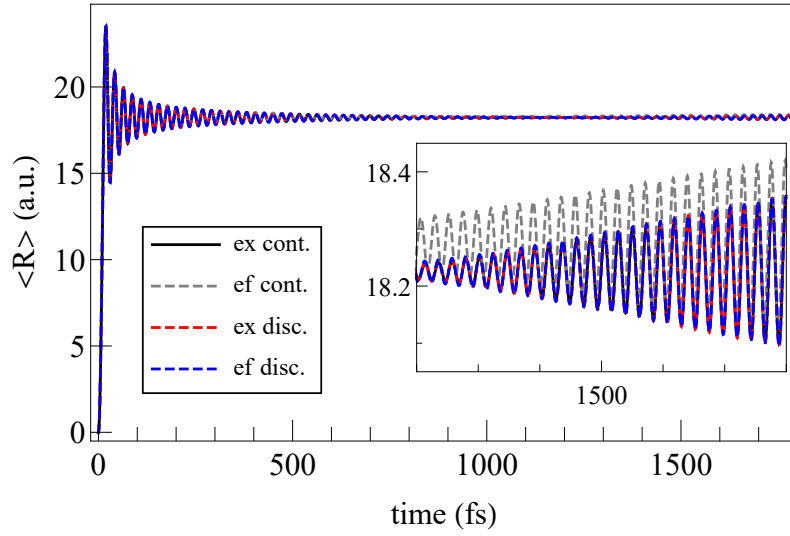
Figure 4.4: The normalized expectation value $\langle R \rangle$ defined by Eq. (4.28). For the exact method, Eq. (4.5) is solved with H^{NH} in the continuous basis Eq. (4.2) (black solid) and in the discrete basis Eq. (4.4) (red dashed), while for the effective mehod, Eq. (4.8) is solved with $H_{\text{eff}}^{\text{NH}}$ in the continuous basis Eq. (4.9) (gray dashed) and in the discrete basis Eq. (4.11) (blue dashed). The vibrational period and the plasmon lifetime are $2\pi/\omega_{\text{v}} = 23\,\text{fs}$ and $2\pi/\gamma_{\text{c}} = 8\,\text{fs}$, respectively. The inset shows the expansion between $t = 1200$ fs and 1800 fs where the deviation of the result obtained by the effective method using the continuous basis becomes clear.

the discrete basis (blue dashed) almost overlaps with that for the exact method, while that obtained using the continuous basis deviates from the others.

In Fig. 4.4, the normalized expectation value $\langle R \rangle$ oscillates with the vibrational period of $2\pi/\omega_v = 23$ fs and the oscillation amplitude becomes smaller as the population in $|A0\rangle$ converges to the stationary value. As can be seen from the inset of Fig. 4.4, $\langle R \rangle$ obtained by the effective method using the continuous basis also deviates from the others.

The deviation observed in Fig. 4.3 and 4.4 can be ascribed to the invalidity of applying the effective operator method by neglecting the kinetic energy operator as we have done in Eq. (4.9). Despite this neglect of the kinetic energy operator, the effective method with the continuous basis still catches the important feature of the dynamics, and therefore we can get a physical interpretation using the effective operators in the continuous basis, Eqs. (4.9) and (4.10), because they are directly related with the nuclear motion as we will show in the following.

4.2.2 Position dependent decay rate
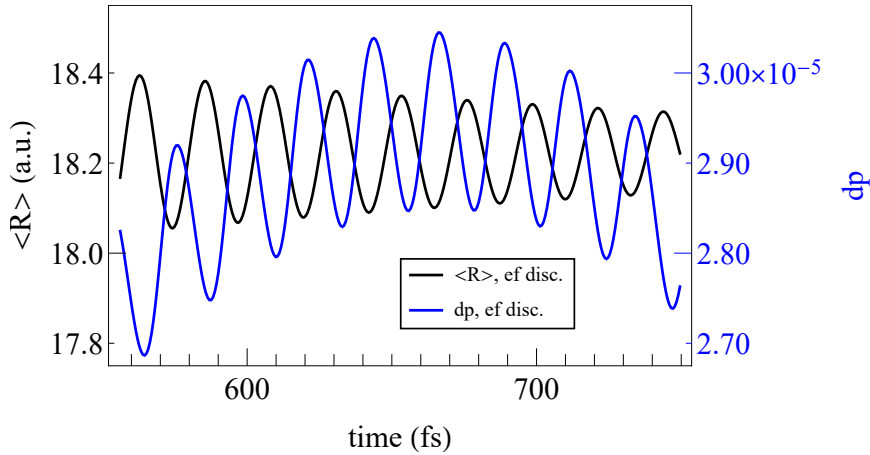
Figure 4.5: The normalized expectation value of R (black) and the jump probability dp (blue) between 556 fs and 749 fs. The vibrational period and the plasmon lifetime are $2\pi/\omega_v = 23$ fs and $2\pi/\gamma_c = 8$ fs, respectively. The calculation is done by the effective method using the discrete basis.

Although the effective method using the continuous basis does not reproduce the results of exact method, it is still useful for interpretation as shown below. Because the cavity mode is resonant with the electronic transition at $R = 0$, i.e. $\omega_c = \omega_{e^-}$, one can expect that the norm of $|\Psi(t)\rangle$ decreases the most when the internuclear distance is close to $R = 0$, where the two PESs, $V_X + \omega_c$ and V_A, cross with each other. This intuition can be partially validated from Eq. (4.20): The diagonal terms of Eq. (4.20) are proportional
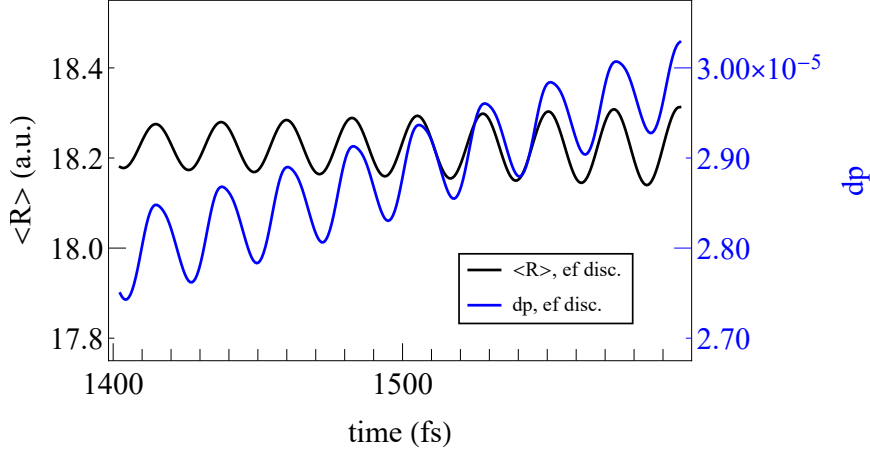
Figure 4.6: The expectation value of R (black) and the jump probability (blue) between 1402 fs and 1596 fs. The vibrational period and the plasmon lifetime are $2\pi/\omega_{\mathrm{v}} = 23\,\mathrm{fs}$ and $2\pi/\gamma_{\mathrm{c}} = 8\,\mathrm{fs}$, respectively. The calculation is done by the effective method using the discrete basis.

to γ_{c} such as

$$\frac{(\mu_{\mathrm{c}}E_0)^2}{4} \frac{\gamma_{\mathrm{c}}}{|\omega_{\mathrm{c}} - \omega_{\mathrm{L}} - \mathrm{i}\gamma_{\mathrm{c}}/2|^2} |C_{\mathrm{X}0,R}|^2, \tag{4.29}$$

$$\frac{\Omega_0^2}{4} \frac{\gamma_{\mathrm{c}}}{|V_{\mathrm{X}} + \omega_{\mathrm{c}} - V_{\mathrm{A}} - \mathrm{i}\gamma_{\mathrm{c}}/2|^2} |C_{\mathrm{A}0,R}|^2, \tag{4.30}$$

which cause the decrease of the diagonal terms of the density matrix, i.e., $(\rho_{\mathrm{g}})_{\mathrm{X}0,\mathrm{X}0} = |C_{\mathrm{X}0,R}|^2$ and $(\rho_{\mathrm{g}})_{\mathrm{A}0,\mathrm{A}0} = |C_{\mathrm{A}0,R}|^2$. The denominator of Eq. (4.29) is R-independent so that dp increases when the population $(\rho_{\mathrm{g}})_{\mathrm{X}0,\mathrm{X}0}$ becomes large. On the other hand, as R becomes close to $R = 0$, the denominator of Eq. (4.30) decreases and so $(\rho_{\mathrm{g}})_{\mathrm{A}0,\mathrm{A}0}$ decays more. Consequently, the jump probability dp is expected to be large as R becomes closer to $R = 0$. This seems to explain Fig. 4.5, where dp increases as R decreases.

In Fig. 4.6, however, dp oscillates in the opposite manner. This is explained from the off-diagonal terms of Eq. (4.20) and that of the density matrix such as $(\rho_{\mathrm{g}})_{\mathrm{X}0\mathrm{A}0} = C_{\mathrm{A}0,R}^* C_{\mathrm{X}0,R}$, i.e., the coherence of the molecule. The numerator of the off-diagonal terms of dp and the coherence $(\rho_{\mathrm{g}})_{\mathrm{X}0,\mathrm{A}0}$ are complex in contrast to the diagonal terms, which is always positive real, they do not always cause the decrease of dp but can contribute to the increase of it. Therefore, the jump probability dp does not merely depend on R and the population but also on the coherence.

When the pulsed laser is applied to pump the cavity mode, Eq. (4.29) and the off-diagonal terms of $H_{\mathrm{eff}}^{\mathrm{NH}}$ vanishes after the laser field vanishes, which one can confirm by setting $E_0 = 0$. Therefore, the jump probability dp only depends on R in the absence of the laser field. This corresponds to the "polaritonic clock" proposed by Silva *et al.* [86], in which the photon emission probability from the cavity completely reflects the internuclear distance.

65

4.3 Conclusion

We have derived the effective master equation describing the dynamics of the molecule placed in the plasmonic nanocavity in the weak coupling regime. We have modified the effective operator formulation given in Ref. [87] so that it becomes applicable to the system including internal degrees of freedom besides the electronic ones.

Although we have derived the effective master equation exactly within the second order perturbation, which we denote as the discrete basis, we have also tested a widely adopted approximation in which the kinetic energy operator for the vibration is neglected in eliminating the fast-evolving state and then it is added to the effective non-Hermitian Hamiltonian, which we denote as the continuous basis. While the effective master equation with the continuous basis has deviated from the numerical integration of the master equation, it still has caught the qualitative behaviour of the exact results. Because the continuous basis is directly connected with the nuclear motion, we have also utilized it to give straightforward physical interpretation.

By applying the MCWP method, the probability of photon emission has been given as the jump probability, which explicitly depends on the nuclear position. This agrees with the "polaritonic clock" situation in Ref. [86], i.e., the jump probability is enhanced when the vibrational wave packet is in the vicinity of the nuclear position where the electronic transition is resonant with the cavity mode. In addition, we have shown that, during the laser field pumping the cavity mode, the jump probability depends also on the coherence between the electronic ground and the excited state so that the photon emission probability reflects not only the nuclear motion but also the vibronic coherence.

Chapter 5

Summary and outlook

(i) Understanding interparticle correlation has been the important issue in multipartite problems. In atomic and molecular physics, the correlation has been evaluated in terms of the energy difference between correlated and uncorrelated systems but in recent years entanglement is employed as an alternative tool for quantifying the correlation.

In Chapter 2, I have investigated the photoionization process of H_2 induced by the irradiation of an ultrashort XUV laser pulse and analyzed the entanglement between H_2^+ and the photoelectron and the coherence in the vibrational states of H_2^+. By quantifying the entanglement by the purity of the reduced density matrix of H_2^+, I have demonstrated how the purity depends on the amount of the coherence in H_2^+, which is controlled by changing the pulse duration. I have also shown that, when the laser intensity becomes large enough to induce the Raman-type transitions among the vibrational states of H_2^+, the purity and the coherence start depending on the intensity.

The entanglement between the photoelectron and the ion should also depend on the initial neutral state. For molecules, because the initial state can be seen as an entangled proton–electron system, it is a non-trivial question whether and how the initial state entanglement is reflected in the entanglement between the photoelectron and the molecular ion. In order to evaluate the entanglement in the initial and the final state using the same basis set, we should use the grid basis and therefore, the grid method developed in Chapter 2 is appropriate also for this direction of the study.

(ii) Furthermore, the coherent motion of the ion created by an ultrashort laser pulse has been investigated and the time delay in the motion has been related to the property of the laser pulse. However, the effect of the correlation between the ion and the photoelectron on the coherent motion has attracted less attention.

In Chapter 3, I have investigated the intrinsic phase $\Delta_{vv'}$ of the reduced density matrix of the vibrational state of H_2^+ created through the ionization and clarified the effect originating from the phase of the photoelectron wave function. Because the intrinsic phase appears as the time delay $\tau_{vv'}$ of the vibrational motion of H_2^+, the effect of the correlation can be extracted from the delay–KER spectrogram obtained

by the pump–probe experiment. The intrinsic time delay $\tau_{vv'}$ is evaluated to be of the order of tens of attoseconds. Therefore, the phase of the photoelectron, which has not been considered before in the determination of the reduced density matrix, should be taken into account when the pump–probe time delay is determined with precision of the order of tens of attoseconds.

The intrinsic time delay can also be investigated in other systems. Specifically, because the phase of the photoelectron wave function can be significantly different for different electronic states of the ion, the coherent superposition of several electronic states is expected to give the large intrinsic time delay. For this purpose, atomic systems such Kr [5] and Xe [12] can be used since their coherent motion has been already investigated using the attosecond transient absorption. For molecular systems such as H_2, the intrinsic time delay can also depend on the molecular rotation as well as the vibration. When the rotation is taken into account, the intrinsic phase of the rhovibrational state of the molecule, $\Delta_{vj,v'j'}$ with j the rotational quantum number, should be determined by the pump–probe experiment.

(iii) By placing the molecule in a cavity, we can further include the quantum correlation with photons which is not taken into account in the preceding chapters on the photoionization of H_2. Such a molecule–cavity system has been attracting attention because of its application to the quantum information and to the control of the chemical reaction.

In Chapter 4, I have derived the effective master equation describing the dynamics of the molecule placed in the plasmonic nanocavity in the weak coupling regime. By applying the MCWP method, the probability of photon emission has been given as the jump probability, which explicitly depends on the nuclear position. In addition, the jump probability is shown to depend also on the coherence between the electronic ground and the excited state and so the photon emission probability reflects not only the nuclear motion but also the vibronic coherence.

Because the photon emitted from the cavity can be continuously monitored, we can consider the effect of the measurement on the molecule, namely, the back-action of the measurement [91]. Due to the randomness of the quantum jump, the dynamics conditioned by the measurement results cannot be simulated by the master equation but stochastic method should be employed [92, 93], which means the continuous measurement of the molecule–cavity system can be simulated in the similar manner as the MCWP formulation employed in Chapter 4.

Appendix A

Calculation of the transition moment

The calculation of the transition dipole moment $\mu_{\boldsymbol{k}_{\mathrm{e}}}$ defined by Eq. (3.6) is detailed. The numerical procedure to obtain the two-center Coulomb wave function defined by Eq. (3.2) is given based on Refs. [80, 94].

A.1 Coulomb wave function

The continuous eigenfunction of a single charged particle for the Coulomb potential is known as the Coulomb wave function given in terms of confluent hypergeometric functions [73]. The Schrödinger equation in the spherical coordinate $\boldsymbol{r} = (r, \theta, \varphi)$ for an electron having the momentum $\boldsymbol{k}_e = (k_e, \theta_e, \varphi_e)$ in a Coulomb potential of a charge Z is given in atomic units as

$$\left(-\frac{1}{2}\Delta_{\mathbf{r}} - \frac{Z}{r} - \frac{k_e^2}{2} \right) \psi_{\boldsymbol{k}_e} = 0. \tag{A.1}$$

By using the parabolic coordinate, the analytical solution of Eq. (A.1) is given by

$$\psi_{\boldsymbol{k}_e}^{(\pm)} = e^{\pi/2k_e}\Gamma\left(1 \mp \frac{i}{k_e} \right) e^{ik_e\boldsymbol{r}} {}_1F_1\left(\pm\frac{i}{k_e}, 1, \pm(k_e r - k_e\boldsymbol{r}) \right), \tag{A.2}$$

where $\psi_{\boldsymbol{k}_e}^{(+)}$ and $\psi_{\boldsymbol{k}_e}^{(-)}$ are called the outgoing and incoming wave, respectively, because their asymptotic forms

$$\psi_{\boldsymbol{k}_e}^{(\pm)} \longrightarrow e^{ik_e\boldsymbol{r}\mp ik_e^{-1}\ln(k_e r\mp k_e\boldsymbol{r})} + f(\theta)\frac{e^{\pm i\{k_e r + k_e^{-1}\ln(2k_e r)\}}}{r}, \tag{A.3}$$

include the outgoing and the incoming spherical waves, respectively, in the second term, where $f(\theta)$ is the scattering amplitude. They are related by

$$\psi_{\boldsymbol{k}_e}^{(-)} = (\psi_{-\boldsymbol{k}_e}^{(+)})^*. \tag{A.4}$$

Since the Coulomb potential is the central force field, the eigenfunction can be expanded in terms of partial waves as

$$\psi_{\boldsymbol{k}_e} = \sum_{l=0}^{\infty} A_l R_{k_e l}(r) P_l\left(\frac{\boldsymbol{k}_e\boldsymbol{r}}{k_e r} \right), \tag{A.5}$$

where $R_{k_e l}$ is the radial wave function and P_l is the Legendre function. By using the relation between the Legendre function and the spherical harmonics Y_{lm},

$$P_l(\cos\gamma) = \frac{4\pi}{2l+1}\sum_{m=-l}^{l} Y_{lm}^*(\theta_e, \varphi_e)Y_{lm}(\theta, \varphi), \tag{A.6}$$

where γ is the angle between $\boldsymbol{r}$ and $\boldsymbol{k}_e$ satisfying $\cos\gamma = \cos\theta\cos\theta_e + \sin\theta\sin\theta_e\cos(\varphi - \varphi_e)$, the Coulomb wave function can be further expanded as

$$\psi_{\boldsymbol{k}_e} = 4\pi\sum_{l=0}^{\infty}\sum_{m=-l}^{l} \frac{A_l}{2l+1} Y_{lm}^*(\theta_e, \varphi_e)Y_{lm}(\theta, \varphi)R_{k_e l}(r). \tag{A.7}$$

The radial wave function is a solution of the following equation

$$\left[\frac{d}{dr}\left(r^2\frac{d}{dr} \right) + 2Zr + k_e^2 r^2 - l(l+1) \right] R_{k_e l} = 0. \tag{A.8}$$

The solution can be given analytically as

$$R_{k_e l} = \frac{1}{k_e r} \frac{e^{\pi/2k_e} |\Gamma(l+1-\mathrm{i}/k_e)| (2k_e r)^{l+1} e^{\mathrm{i}k_e r}}{2(2l+1)!} \, {}_1F_1\left(l+1-\frac{\mathrm{i}}{k_e}, 2l+2, -2\mathrm{i}k_e r\right), \quad (A.9)$$

and its asymptotic form is given as

$$R_{k_e l} \longrightarrow \frac{1}{k_e r} \sin\left(k_e r - \frac{l\pi}{2} + \sigma_l + \frac{1}{k_e}\ln(2k_e r)\right), \quad (A.10)$$

where σ_l called the phase shift is defined as

$$\sigma_l = \arg\Gamma\left(l+1-\frac{\mathrm{i}}{k_e}\right). \quad (A.11)$$

The expansion coefficient A_l is determined by comparing Eq. (A.7) with Eq. (A.2) so that it satisfies the outgoing or the incoming boundary condition and we obtain

$$A_l = (2l+1)\mathrm{i}^l e^{\pm\mathrm{i}\sigma_l}. \quad (A.12)$$

Finally, by imposing the normalization condition

$$\int d\boldsymbol{r}\, \psi_{\boldsymbol{k}_e'}^*(\boldsymbol{r}) \psi_{\boldsymbol{k}_e}(\boldsymbol{r}) = \delta(\boldsymbol{k}_e' - \boldsymbol{k}_e), \quad (A.13)$$

the partial wave expansion (A.7) is obtained as

$$\psi_{\boldsymbol{k}_e}^{(\pm)} = (2\pi)^{-3/2} 4\pi \sum_{l=0}^{\infty} \sum_{m=-l}^{l} \mathrm{i}^l e^{\pm\mathrm{i}\sigma_l} Y_{lm}^*(\theta_e, \varphi_e) Y_{lm}(\theta, \varphi) R_{k_e l}(r). \quad (A.14)$$

A.2 Two-center Coulomb wave function

Because the final state of the ionization is known to satisfy the incoming wave boundary condition [73, 95, 96], we will focus on the incoming wave in the following. In the two-center Coulomb potential, where two charges Z_a and Z_b are separated by a distance R, the continuous eigenfunction is given in a similar form as the one-center Coulomb wave function. The two-center Coulomb wave function is defined as the eigenfunction of the Schrödinger equation,

$$\left(-\frac{1}{2}\Delta_{\mathbf{r}} - \frac{Z_a}{|\mathbf{r} - \mathbf{R}/2|} - \frac{Z_b}{|\mathbf{r} + \mathbf{R}/2|} - \frac{k_e^2}{2}\right)\psi_{\mathbf{k}_e} = 0. \tag{A.15}$$

The eigenfunction satisfying the incoming boundary condition can be expanded as

$$\psi_{\mathbf{k}_e}(\mathbf{r}; R) = (2\pi)^{-3/2} 4\pi \sum_{l=0}^{\infty} \sum_{m=-l}^{l} i^l e^{-i\delta_{lm}}$$
$$\times \Upsilon_{lm}^*(c_e, \theta_e, \varphi_e)\Upsilon_{lm}(c_e, \theta, \varphi)T_{lm}(c_e, \xi; R), \tag{A.16}$$

$$\Upsilon_{lm}(c_e, \theta, \varphi) = S_{lm}(c_e, \cos\theta)\frac{\exp(im\varphi)}{\sqrt{2\pi}}, \tag{A.17}$$

in the prolate spheroidal coordinate system, $\xi = (|\mathbf{r} - \mathbf{R}/2| + |\mathbf{r} + \mathbf{R}/2|)/R \in [1, \infty)$, $\eta = (|\mathbf{r} - \mathbf{R}/2| - |\mathbf{r} + \mathbf{R}/2|)/R \in [-1, 1]$, and $\varphi \in [0, 2\pi]$. The angles θ, θ_e, φ and φ_e are defined with respect to the molecular axis and so the prolate spheroical coordinate and the spherical coordinate are related as

$$\xi = \left[\frac{1}{2}\left\{1 + \frac{4r^2}{R^2} + \sqrt{1 + \frac{16r^4}{R^4} + \frac{8r^2}{R^2}(1 - 2\cos^2\theta)}\right\}\right]^{1/2}, \tag{A.18}$$

$$\eta = \frac{2r\cos\theta}{R\xi}. \tag{A.19}$$

The quasiradial and the quasiangular functions, $T_{lm}(c_e, \xi)$ and $S_{lm}(c_e, \eta)$ respectively, satisfy the following equations,

$$\left[\frac{d}{d\xi}(\xi^2 - 1)\frac{d}{d\xi} + a\xi - \frac{m^2}{\xi^2 - 1} + c_e^2(\xi^2 - 1) - \lambda_{lm}\right]T_{lm} = 0, \tag{A.20}$$

$$\left[\frac{d}{d\eta}(1 - \eta^2)\frac{d}{d\eta} + b\eta - \frac{m^2}{1 - \eta^2} + c_e^2(1 - \eta^2) + \lambda_{lm}\right]S_{lm} = 0, \tag{A.21}$$

where $a = R(Z_b + Z_a)$, $b = R(Z_b - Z_a)$, $c_e = k_e R/2$, and λ_{lm} is the eigenvalue of Eq. (A.21). The eigenvalue λ_{lm} can be obtained as the root of a equation $y(\lambda) = 0$, where the left hand side is expanded as an infinite chain fraction [94],

$$y(\lambda) = \kappa_0 - \cfrac{\rho_0\delta_1}{\kappa_1 - \cfrac{\rho_1\delta_2}{\kappa_2 - \cdots}}, \tag{A.22}$$

with

$$\rho_s = (s + 2m + 1)\frac{b - 2ic_e(s + m + 1)}{2(s + m) + 3} \tag{A.23}$$

$$\kappa_s = -\lambda + (s + m)(s + m + 1) \tag{A.24}$$

$$\delta_s = s\frac{b + 2ic_e(s + m)}{2(s + m) - 1}. \tag{A.25}$$

We have confirmed the convergence of Eq. (A.22) by including $s = 0 - 50$.

In order to solve the Schrödinger equations (A.20) and (A.21) by numerical integration, we apply the following transformation

$$X_{lm}(\xi) = (\xi - 1)T_{lm}(c_e, \xi), \tag{A.26}$$
$$Y_{lm}(\eta) = (1 - \eta^2)S_{lm}(c_e, \eta), \tag{A.27}$$

with which we can rewrite Eqs. (A.20) and (A.21) as

$$\left[(\xi^2 - 1)\frac{d^2}{d\xi^2} - 2\xi\frac{d}{d\xi} + \frac{2}{\xi - 1} + a\xi - \frac{m^2}{\xi^2 - 1} + c_e^2(\xi^2 - 1) - \lambda_{lm}\right]X_{lm} = 0, \tag{A.28}$$

$$\left[(1 - \eta^2)\frac{d^2}{d\eta^2} + 2\eta\frac{d}{d\eta} + \frac{2(1 + \eta^2)}{1 - \eta^2} + b\eta - \frac{m^2}{1 - \eta^2} + c_e^2(1 - \eta^2) + \lambda_{lm}\right]Y_{lm} = 0, \tag{A.29}$$

with the boundary conditions

$$X(1) = 0, \tag{A.30}$$
$$Y(-1) = Y(1) = 0. \tag{A.31}$$

In numerically integrating Eqs. (A.28) and (A.29), the boundary values Eqs. (A.30) and (A.31) cannot be used because some terms in Eqs. (A.28) and (A.29) are singular at $\xi = 1$ and $\eta = \pm 1$, respectively. For Y_{lm}, we instead solve the boundary value problem with the following condition

$$Y_{lm}(-1 + \delta\eta) = (-1)^l Y_{lm}(1 - \delta\eta) = \epsilon_Y, \tag{A.32}$$

where we utilized the fact that Y_{lm} is the even (odd) function for even (odd) l. The parameters $\delta\eta$ and ϵ_Y can be arbitrarily chosen and we set to $\delta\eta = \cos(10^{-3})$ and $\epsilon_Y = 10^{-3}$. Finally, we normalize Y_{lm} by

$$\int_{-1}^{1} d\eta Y_{lm}^2(\eta) = 1. \tag{A.33}$$

On the other hand, in order to obtain X_{lm}, we solve (A.28) with the initial values $\epsilon_X = X_{lm}(1 + \delta\xi)$ and $d\epsilon_X/d\xi$ at $\xi = 1 + \delta\xi$ calculated from the following expansion,

$$X_{lm} = (\xi^2 - 1)^{m/2} \sum_{s=0}^{s_{max}} g_s(\xi - 1)^{s+1} \text{ (valid in } 1 \leq \xi < 2), \tag{A.34}$$

73

where g_s is obtained from the four-term recurrent relation

$$\alpha_1 g_{s+1} + \alpha_2 g_s + \alpha_3 g_{s-1} + \alpha_4 g_{s-2} = 0, \tag{A.35}$$
$$g_{-2} = g_{-1} = 0, \ g_0 = 1,$$
$$\alpha_1 = 2(s+1)(s+m+1),$$
$$\alpha_2 = s(s+2m+1) - \lambda + a + m(m+1),$$
$$\alpha_3 = 2c_{\mathrm{e}}^2 + a,$$
$$\alpha_4 = c_{\mathrm{e}}^2.$$

The choice of $d\xi$ is explained in Sec. A.3. In the asymptotic region $\xi \longrightarrow \infty$, X_{lm} behaves as

$$X_{lm}(\xi) \longrightarrow \frac{1}{c_{\mathrm{e}}} \sin\left(c_{\mathrm{e}}\xi + \frac{a}{2c_{\mathrm{e}}} \ln(2c_{\mathrm{e}}\xi) - \frac{l\pi}{2} + \delta_{lm} \right). \tag{A.36}$$

The phase shift δ_{lm} is determined by comparing X_{lm} obtained by numerical integration of Eq. (A.28) with the analytical expression (A.36).

A.3 Transition moment

In calculating the transition moment $\mu_{\boldsymbol{k}_{\mathrm{e}}}$ (defined by Eq. (3.6))

$$\mu_{\boldsymbol{k}_{\mathrm{e}}}(R) = \iint d\boldsymbol{r}_1 d\boldsymbol{r}_2 \phi_{1\mathrm{s}}(\boldsymbol{r}_1; R)\psi_{\boldsymbol{k}_{\mathrm{e}}}^*(\boldsymbol{r}_2; R)(z_1 + z_2)\phi_g(\boldsymbol{r}_1, \boldsymbol{r}_2; R), \qquad (A.37)$$

we numerically integrate using the grid space in the spherical coordinate $\boldsymbol{r} = (r, \theta, \varphi)$ and so we need to convert the spheroidal coordinate appeared in Eq. (A.16) to the spherical coordinate by using the relation Eq. (A.18). The grid space for the radial coordinate is taken as $r = [0.1, 40]$ a.u. with $dr = 0.1$ a.u.. The grid space for the angle is taken as $\theta = [0, \pi]$ rad with $d\theta = \pi/40$ rad and then, $\theta = 0$ rad and π rad are replaced by 0.001 rad and $\pi - 0.001$ rad, respectively, since $\theta = 0 \,\mathrm{or}\, \pi$ does not contribute to the transition moment due to the factor $\sin\theta_1 \sin\theta_2$ of the volume element in the integral Eq. (A.37).

Because ξ depends not only on r but also on θ and R, we use Eq. (A.18) to define the grid space for ξ at each θ and R so that it corresponds to the grid space for r and then solve Eq. (A.28) by Runge–Kutta method. The initial value is defined by Eq. (A.34) and its derivative at $\xi = 1 + \delta\xi$. As explained above, $1 + \delta\xi$ corresponds to $r = 0.1$ a.u. but depends on θ and R. On the other hand, the grid space for η can be taken the same as the grid space for $\cos\theta$ because the argument of S_{lm} in Eq. (A.17) is written in terms of $\cos\theta$ instead of η.

The ground state of H_2, ϕ_g, is obtained by the full configuration interaction (CI) method with the aug-cc-pVQZ basis set and can be expressed explicitly in terms of molecular orbitals Ψ_i as

$$\phi_g(\boldsymbol{r}_1, \boldsymbol{r}_2) = N \left\{ \Psi_0(\boldsymbol{r}_1)\Psi_0(\boldsymbol{r}_2) + \frac{1}{\sqrt{2}}\sum_{i \neq j} C_{ij}\Psi_i(\boldsymbol{r}_1)\Psi_j(\boldsymbol{r}_2) + \sum_i C_{ii}\Psi_i(\boldsymbol{r}_1)\Psi_i(\boldsymbol{r}_2) \right\}, \qquad (A.38)$$

where N is the normalization constant and $C_{ij} = C_{ji}$. Although the two-center Coulomb wave function $\psi_{\boldsymbol{k}_{\mathrm{e}}}$ includes the infinite sum, only a few terms satisfying the following conditions contributes to the integral Eq. (A.37).

(a) Only $m = 0$ is allowed
Because the $1\mathrm{s}\sigma_{\mathrm{g}}$ state of H_2^+, $\phi_{1\mathrm{s}}(\boldsymbol{r}_1) \propto R(r_1)\Theta(\theta_1)e^{im'\varphi_1}$, is homogeneous around the molecular axis, $m' = 0$. Therefore, the integration about the azimuthal angle in Eq. (A.37) can be written as

$$I_\varphi = \int d\varphi_2 e^{-im\varphi_2} \int d\varphi_1 \phi_g(\boldsymbol{r}_1, \boldsymbol{r}_2), \qquad (A.39)$$

where $e^{-im\varphi_2}$ is the azimuthal function of the photoelectron wave function $\psi_{\boldsymbol{k}_{\mathrm{e}}}^*$. By denoting the azimuthal function of the orbitals $\Psi_i(\boldsymbol{r}_1)$ as $e^{im_i\varphi_1}$, the φ_1-integral is composed of the following terms

$$\int d\varphi_1 e^{im_i\varphi_1}, \qquad (A.40)$$

which is nonzero only when $m_i = 0$. Because ϕ_g is symmetric about the center of mass, i.e., $\phi_g(\boldsymbol{r}_1, \boldsymbol{r}_2) = \phi_g(-\boldsymbol{r}_1, -\boldsymbol{r}_2)$, the orbitals for the second electron $\Psi_j(\boldsymbol{r}_2)$ multiplied with $\Psi_i(\boldsymbol{r}_1)$ with $m_i = 0$ should also be homogeneous about the azimuthal angle, i.e., $m_j = 0$. Therefore, the integral Eq. (A.39) reduces as

$$I_\varphi = 2\pi \int d\varphi_2 e^{-im\varphi_2}, \tag{A.41}$$

which is nonzero only when $m = 0$, verifying the statement below Eq. (3.2), and we obtain $I_\varphi = (2\pi)^2$.

(b) Only odd l's are allowed

Because of the symmetry condition $\phi_g(\boldsymbol{r}_1, \boldsymbol{r}_2) = \phi_g(-\boldsymbol{r}_1, -\boldsymbol{r}_2)$, two orbitals $\Psi_i \Psi_j$ in the CI expansion Eq. (A.38) should have the same symmetry, g or u. We rewrite Eq. (A.38) by denoting the symmetry explicitly as

$$\phi_g(\boldsymbol{r}_1, \boldsymbol{r}_2) = \sum_{ij} A_{ij}^{(\mathrm{g})} \Psi_i^{(\mathrm{g})}(\boldsymbol{r}_1) \Psi_j^{(\mathrm{g})}(\boldsymbol{r}_2) + \sum_{ij} A_{ij}^{(\mathrm{u})} \Psi_i^{(\mathrm{u})}(\boldsymbol{r}_1) \Psi_j^{(\mathrm{u})}(\boldsymbol{r}_2), \tag{A.42}$$

where the coefficients in Eq. (A.38) are incorporated into $A_{ij}^{(\mathrm{g,u})}$. We insert Eq. (A.42) into Eq. (A.37) and we divide the integral into two contributions as

$$I_1 = \iint d\boldsymbol{r}_1 d\boldsymbol{r}_2 \phi_{1\mathrm{s}}(\boldsymbol{r}_1) \psi_{\boldsymbol{k}_\mathrm{e}}^*(\boldsymbol{r}_2) z_1$$
$$\times \left\{ \sum_{ij} A_{ij}^{(\mathrm{g})} \Psi_i^{(\mathrm{g})}(\boldsymbol{r}_1) \Psi_j^{(\mathrm{g})}(\boldsymbol{r}_2) + \sum_{ij} A_{ij}^{(\mathrm{u})} \Psi_i^{(\mathrm{u})}(\boldsymbol{r}_1) \Psi_j^{(\mathrm{u})}(\boldsymbol{r}_2) \right\}, \tag{A.43}$$

$$I_2 = \iint d\boldsymbol{r}_1 d\boldsymbol{r}_2 \phi_{1\mathrm{s}}(\boldsymbol{r}_1) \psi_{\boldsymbol{k}_\mathrm{e}}^*(\boldsymbol{r}_2) z_2$$
$$\times \left\{ \sum_{ij} A_{ij}^{(\mathrm{g})} \Psi_i^{(\mathrm{g})}(\boldsymbol{r}_1) \Psi_j^{(\mathrm{g})}(\boldsymbol{r}_2) + \sum_{ij} A_{ij}^{(\mathrm{u})} \Psi_i^{(\mathrm{u})}(\boldsymbol{r}_1) \Psi_j^{(\mathrm{u})}(\boldsymbol{r}_2) \right\}. \tag{A.44}$$

For I_1, because $\phi_{1\mathrm{s}}$ is even and z_1 is odd function, only the ungerade orbital, $\Psi_i^{(\mathrm{u})}$, can contribute, and because its pair, $\Psi_j^{(\mathrm{u})}$, is odd function, $\psi_{\boldsymbol{k}_\mathrm{e}}^*$ should be odd, i.e., the quasiangular quantum number l should be odd. Similarly, for I_2, because $\phi_{1\mathrm{s}}$ is even function, only the gerade orbital, $\Psi_i^{(\mathrm{g})}$ can contribute, and because its pair, $\Psi_j^{(\mathrm{g})}$ is even and z_2 is odd function, $\psi_{\boldsymbol{k}_\mathrm{e}}^*$ should be odd function.

Appendix B

Derivation of the effective operators

The effective non-Hermitian Hamiltonian and the effective Lindbladian given in 4.1.3 are derived by modifying the effective operator method of Ref. [87] and then, the jump probability given in 4.1.4 are derived.

B.1   General formulation

First, the total system is divided into the fast-evolving and the slow-evolving states, which are denoted as the excited states and the ground states, respectively. The excited states decay to the ground states and the ground states do not decay. In this appendix, we include the coupling between different slow-evolving states, which is neglected in the main text, so that we can apply the present formulation to the more general case where the laser directly excites the molecule. After the general formulation is obtained, the effective master equation in the main text Eq. (4.8) is obtained as a special case by neglecting the laser–molecule coupling. The Hamiltonian in the Schrödinger picture is given as

$$H_S = H_0 + V_S(t) = H_\mathrm{g} + H_\mathrm{e} + V_\mathrm{gg}^S(t) + V_+^S(t) + V_-^S(t), \tag{B.1}$$

where $V_\mathrm{gg}^S(t) = P_\mathrm{g} V_S(t) P_\mathrm{g}$, $V_+^S(t) = P_\mathrm{e} V_S(t) P_\mathrm{g}$, and $V_-^S(t) = P_\mathrm{g} V_S(t) P_\mathrm{e}$, with P_e and P_g the projection operators for the excited states and the ground states, respectively. Here, we also include the interaction between different ground states, V_gg^S. The master equation in the interaction picture is written as

$$\dot{\rho} = -\mathrm{i}[V(t), \rho] - \frac{1}{2} \sum_k (L_k^\dagger L_k \rho + \rho L_k^\dagger L_k) + \sum_k L_k \rho L_k^\dagger, \tag{B.2}$$

where L_k is the Lindbladian for the kth dissipation path and the interaction Hamiltonian $V(t)$ is given as

$$V(t) = e^{\mathrm{i}H_0 t} V_S(t) e^{-\mathrm{i}H_0 t}. \tag{B.3}$$

In the following, we consider only one excited state $|\mathrm{e}\rangle$ interacting with sevral ground states $|\mathrm{g}_l\rangle$ ($l = 1, 2, \dots$), and one dissipation path described by a Lindbladian $L = \sqrt{\gamma_\mathrm{c}}\, |\mathrm{g}_1\rangle \langle \mathrm{e}|$. We assume the couplings between the excited state and the ground states are weak so that we can treat them as perturbations. By introducing

$$O = \exp\left(\mathrm{i} \left(-\frac{\mathrm{i}}{2} L^\dagger L \right) t \right) = \exp\left(\frac{\gamma_\mathrm{c}}{2} t P_\mathrm{e} \right), \tag{B.4}$$

the master equation for $\tilde{\rho} = O\rho O$ is given by

$$\dot{\tilde{\rho}} = -\mathrm{i}(\tilde{V}\tilde{\rho} - \tilde{\rho}\tilde{V}^\mathrm{c}) + \tilde{L}\tilde{\rho}\tilde{L}^\dagger, \tag{B.5}$$

where $\tilde{V} = OVO^{-1}$, $\tilde{V}^\mathrm{c} = O^{-1}VO$, $\tilde{L} = OLO^{-1}$, and $\tilde{L}^\dagger = O^{-1}L^\dagger O$ are introduced and a relation $OL^\dagger L O^{-1} = \exp(\gamma_\mathrm{c} t/2) L^\dagger L \exp(-\gamma_\mathrm{c} t/2) = L^\dagger L$ is utilized. First, we implicitly solve the master equation as

$$\tilde{\rho}(t) = \tilde{\rho}(t_0) - \mathrm{i} \int^t dt' \left(\tilde{V}(t')\tilde{\rho}(t') - \tilde{\rho}(t')\tilde{V}^\mathrm{c}(t') \right) + \int^t dt' \tilde{L}(t')\tilde{\rho}(t')\tilde{L}^\dagger(t'), \tag{B.6}$$

where the initial state is given at t_0. Inserting this into Eq. (B.5), the master equation is

rewritten as

$$\dot{\rho} = -i\tilde{V}(t)\tilde{\rho}(t_0) - \tilde{V}(t)\int^t dt'\left(\tilde{V}(t')\tilde{\rho}(t') - \tilde{\rho}(t')\tilde{V}^c(t')\right) - i\tilde{V}(t)\int^t dt'\tilde{L}(t')\tilde{\rho}(t')\tilde{L}^\dagger(t')$$
$$+ \text{H.c.}$$
$$+ \tilde{L}(t)\tilde{\rho}(t_0)\tilde{L}^\dagger(t) - i\tilde{L}(t)\int^t dt'\left(\tilde{V}(t')\tilde{\rho}(t') - \tilde{\rho}(t')\tilde{V}^c(t')\right)\tilde{L}^\dagger(t)$$
$$+ \tilde{L}(t)\int^t dt'\tilde{L}(t')\tilde{\rho}(t')\tilde{L}^\dagger(t')\tilde{L}^\dagger(t). \tag{B.7}$$

In order to describe a master equation for the ground state subspace, we introduce a ground state density matrix $\tilde{\rho}_\text{g} = P_\text{g}\tilde{\rho}P_\text{g}$. By using the fact that $\tilde{L} = P_\text{g}\tilde{L}P_\text{e}$, $\tilde{L}^\dagger = P_\text{e}\tilde{L}^\dagger P_\text{g}$, and $\tilde{V} = P_\text{e}\tilde{V}_+P_\text{g} + P_\text{g}\tilde{V}_-P_\text{e} + P_\text{g}\tilde{V}_\text{gg}P_\text{g}$, and assuming the initial state is in the ground state manifold, i.e., $\tilde{\rho}(t_0) = P_\text{g}\tilde{\rho}(t_0)P_\text{g}$, the master equation for $\tilde{\rho}_\text{g}$ is given as

$$\dot{\tilde{\rho}}_\text{g} = -i\tilde{V}_\text{gg}(t)\tilde{\rho}_\text{g}(t_0) - \tilde{V}_-(t)\int^t dt'\left(\tilde{V}_+(t')\tilde{\rho}_\text{g}(t') - \tilde{\rho}_\text{e}(t')\tilde{V}_+^c(t')\right)$$
$$- \int^t dt'\left\{\tilde{V}_\text{gg}(t)\left(\tilde{V}_\text{gg}(t')\tilde{\rho}_\text{g}(t') + \tilde{V}_-(t')\tilde{\rho}_\text{eg}(t')\right)\right\}$$
$$+ \int^t dt'\left\{\left(\tilde{V}_\text{gg}(t)\tilde{\rho}_\text{g}(t') + \tilde{V}_-(t)\tilde{\rho}_\text{eg}(t')\right)\tilde{V}_\text{gg}^c(t')\right\}$$
$$- i\tilde{V}_\text{gg}(t)\int^t dt'\tilde{L}(t')\tilde{\rho}_\text{e}(t')\tilde{L}^\dagger(t') + \text{H.c.}$$
$$- i\tilde{L}(t)\int^t dt'\left(\tilde{V}_+(t')\tilde{\rho}_\text{ge}(t') - \tilde{\rho}_\text{eg}(t')\tilde{V}_-^c(t')\right)\tilde{L}^\dagger(t). \tag{B.8}$$

where $\tilde{\rho}_\text{e}(t') = P_\text{e}\tilde{\rho}(t')P_\text{e}$, $\tilde{\rho}_\text{eg}(t') = P_\text{e}\tilde{\rho}(t')P_\text{g}$, and $\tilde{\rho}_\text{ge}(t') = P_\text{g}\tilde{\rho}(t')P_\text{e}$. By using Eq. (B.6), $\tilde{\rho}_\text{eg}$ and $\tilde{\rho}_\text{ge}$ in Eq. (B.8) can be further expanded as,

$$\tilde{\rho}_\text{ge}(t') = i\int^{t'} dt''\tilde{\rho}_\text{g}(t'')\tilde{V}_-^c(t''), \tag{B.9}$$

$$\tilde{\rho}_\text{eg}(t') = -i\int^{t'} dt''\tilde{V}_+(t'')\tilde{\rho}_\text{g}(t''), \tag{B.10}$$

where the terms higher than the first order in $\tilde{V}$ are omitted. Although we can also expand $\tilde{\rho}_\text{e}$ in the same manner as

$$\tilde{\rho}_\text{e}(t') = -i\int^{t'} dt''\left(\tilde{V}_+(t'')\tilde{\rho}_\text{ge}(t'') - \tilde{\rho}_\text{eg}(t'')\tilde{V}_-^c(t'')\right), \tag{B.11}$$

considering the fact that $\tilde{\rho}_\text{ge}$ and $\tilde{\rho}_\text{eg}$ are as small as the first order in $\tilde{V}$, $\tilde{\rho}_\text{e}$ is as small as the second order in $\tilde{V}$ and so we neglect $\tilde{\rho}_\text{e}$ in Eq. (B.8).

By inserting Eqs. (B.9) and (B.10) into Eq. (B.8), the master equation of the second

order in $\tilde{V}$ is given as

$$\dot{\tilde{\rho}}_g = -i\tilde{V}_{gg}(t)\tilde{\rho}_g(t_0) - \tilde{V}_-(t)\int^t dt'\tilde{V}_+(t')\tilde{\rho}_g(t')$$

$$- \tilde{V}_{gg}(t)\int^t dt'\left(\tilde{V}_{gg}(t')\tilde{\rho}_g(t') - \tilde{\rho}_g(t')\tilde{V}^c_{gg}(t')\right) + \text{H.c.}$$

$$+ \tilde{L}(t)\int^t dt'\int^{t'} dt''\left(\tilde{V}_+(t')\tilde{\rho}_g(t'')\tilde{V}^c_-(t'') + \text{H.c.}\right)\tilde{L}^\dagger(t). \quad (B.12)$$

In order to obtain a linear equation, we replace $\tilde{\rho}_g$ in the integral by $\tilde{\rho}_g(t)$

$$\dot{\tilde{\rho}}_g = -i\tilde{V}_{gg}(t)\tilde{\rho}_g(t_0) - \tilde{V}_-(t)\int^t dt'\tilde{V}_+(t')\tilde{\rho}_g(t)$$

$$- \tilde{V}_{gg}(t)\int^t dt'\left(\tilde{V}_{gg}(t')\tilde{\rho}_g(t) - \tilde{\rho}_g(t)\tilde{V}^c_{gg}(t')\right) + \text{H.c.}$$

$$+ \tilde{L}(t)\int^t dt'\int^{t'} dt''\left(\tilde{V}_+(t')\tilde{\rho}_g(t)\tilde{V}^c_-(t'') + \text{H.c.}\right)\tilde{L}^\dagger(t). \quad (B.13)$$

This replacement of $\tilde{\rho}_g(t')$ by $\tilde{\rho}_g(t)$ can be validated when $\tilde{\rho}_g(t')$ changes slowly compared to $\tilde{V}(t')$. From Eq. (B.5), when the interaction V is small, the no-jump dynamics is slow, i.e., $\tilde{\rho}_g$ changes slowly. On the other hand, from Eq. (B.12), $P_e\tilde{V}(t')P_g = e^{\gamma_c t/2}P_e V(t')P_g$ rapidly increases when γ_c is large. Thus, it is necessary to keep V small and γ large in order for Eq. (B.13) to be valid.

By using the relation $P_g O = OP_g = P_g$, some terms in Eq. (B.13) can be replaced as $\tilde{\rho}_g = \rho_g$, $\tilde{V}_{gg} = V_{gg}$, $\tilde{V}_- = V_- O^{-1}$, $\tilde{V}_+ = OV_+$, $\tilde{L} = LO^{-1}$, $\tilde{L}^\dagger = O^{-1}L^\dagger$, and, therefore, Eq. (B.13) can be simplified as

$$\dot{\rho}_g = -ie^{iH_g t}V^S_{gg}(t)e^{-iH_g t}\rho_g(t_0)$$

$$- e^{iH_g t}V^S_-(t)e^{-iH_e t}O^{-1}(t)I\rho_g(t)$$

$$- e^{iH_g t}V^S_{gg}(t)e^{-iH_g t}I_g\rho_g(t) + \text{H.c.}$$

$$+ LO^{-1}(t)I\rho_g(t)I^\dagger O^{-1}(t)L^\dagger$$

$$= I_0 + I_1 + I_2 + (I_0 + I_1 + I_2)^\dagger + I_3. \quad (B.14)$$

where I and I_g are defined as

$$I = \int^t dt' O(t')e^{iH_e t'}V^S_+(t')e^{-iH_g t'}, \quad (B.15)$$

$$I_g = \int^t dt' e^{iH_g t'}V^S_{gg}(t')e^{-iH_g t'}. \quad (B.16)$$

B.2 Time-independent interaction

After calculating the integrals I and I_{g}, we can solve the master equation Eq. (B.14). Here, we consider the time-independent interaction, $V_{\pm}^{S}$ and V_{gg}^{S}. In addition, we denote an internal degree of freedom for each electronic state by a quantum number v, i.e., $\{|\mathrm{g}_{l}, v\rangle, |\mathrm{e}, v\rangle\}$. Then, the operators appeared in Eq. (B.14) are given explicitly as

$$
\begin{aligned}
H_{\mathrm{g}} &= \sum_{lv} E_{\mathrm{g}_l,v} |\mathrm{g}_l, v\rangle \langle \mathrm{g}_l, v|, \, H_{\mathrm{e}} = \sum_v E_{\mathrm{e},v} |\mathrm{e}, v\rangle \langle \mathrm{e}, v|, \\
V_{\mathrm{gg}}^{S} &= \sum_{l \neq l', vv'} V_{\mathrm{gg}}^{(lv,l'v')} = \sum_{l \neq l', vv'} g_{lv,l'v'} |\mathrm{g}_l, v\rangle \langle \mathrm{g}_{l'}, v'|, \\
V_{+}^{S} &= \sum_{lvv'} V_{+}^{(v,lv')} = \sum_{lvv'} f_{v,lv'} |\mathrm{e}, v\rangle \langle \mathrm{g}_l, v'|, \\
V_{-}^{S} &= \sum_{lvv'} V_{-}^{(lv',v)} = \sum_{lvv'} f_{v,lv'} |\mathrm{g}_l, v'\rangle \langle \mathrm{e}, v|, \\
L &= \sum_v L_v = \sqrt{\gamma_c} \sum_v |\mathrm{g}_1, v\rangle \langle \mathrm{e}, v|.
\end{aligned}
\tag{B.17}
$$

The integrals Eqs. (B.15) and (B.16) can be calculated as

$$
\begin{aligned}
I &= -\mathrm{i} \sum_{lvv'} \frac{O(t)e^{\mathrm{i}(E_{\mathrm{e},v} - E_{\mathrm{g}_l,v'})t} - O(t_0)e^{\mathrm{i}(E_{\mathrm{e},v} - E_{\mathrm{g}_l,v'})t_0}}{E_{\mathrm{e},v} - E_{\mathrm{g}_l,v'} - \mathrm{i}\gamma_{\mathrm{c}}/2} V_{+}^{(v,lv')}, \\
I_{\mathrm{g}} &= -\mathrm{i} \sum_{l \neq l', vv'} \frac{e^{\mathrm{i}(E_{\mathrm{g}_l,v} - E_{\mathrm{g}_{l'},v'})t} - e^{\mathrm{i}(E_{\mathrm{g}_l,v} - E_{\mathrm{g}_{l'},v'})t_0}}{E_{\mathrm{g}_l,v} - E_{\mathrm{g}_{l'},v'}} V_{\mathrm{gg}}^{(lv,l'v')}.
\end{aligned}
\tag{B.18}
$$

and I_0, I_1, I_2 are given as

$$
I_0 = -\mathrm{i} \sum_{l \neq l', vv'} e^{\mathrm{i}(E_{\mathrm{g}_l,v} - E_{\mathrm{g}_{l'},v'})t} V_{\mathrm{gg}}^{(lv,l'v')} \rho_{\mathrm{g}}(t_0),
\tag{B.19}
$$

$$
I_1 = \mathrm{i} \sum_{\substack{lvv' \\ l'u'}} V_{-}^{(l'u',v)} e^{\mathrm{i}(E_{\mathrm{g}_{l'},u'} - E_{\mathrm{g}_{l'},v'})t} \frac{1 - e^{-\mathrm{i}(E_{\mathrm{e},v} - E_{\mathrm{g}_l,v'} - \mathrm{i}\gamma_{\mathrm{c}}/2)(t-t_0)}}{E_{\mathrm{e},v} - E_{\mathrm{g}_l,v'} - \mathrm{i}\gamma_{\mathrm{c}}/2} V_{+}^{(v,lv')} \rho_{\mathrm{g}}(t),
\tag{B.20}
$$

$$
I_2 = \mathrm{i} \sum_{\substack{l \neq l', vv' \\ l' \neq m', u'}} V_{\mathrm{gg}}^{(lv,l'v')} e^{\mathrm{i}(E_{\mathrm{g}_l,v} - E_{\mathrm{g}_{m'},u'})t} \frac{1 - e^{-\mathrm{i}(E_{\mathrm{g}_{l'},v'} - E_{\mathrm{g}_{m'},u'})(t-t_0)}}{E_{\mathrm{g}_{l'},v'} - E_{\mathrm{g}_{m'},u'}} V_{\mathrm{gg}}^{(l'v',m'u')} \rho_{\mathrm{g}}(t),
$$

$$
I_3 = L_{\mathrm{eff}} \rho_{\mathrm{g}} L_{\mathrm{eff}}^{\dagger},
\tag{B.21}
$$

where the effective Lindbladian is defined as

$$
\begin{aligned}
L_{\mathrm{eff}} &= LO^{-1}(t)I \\
&= -\mathrm{i} \sum_{lvv'} L_v e^{\mathrm{i}(E_{\mathrm{e},v} - E_{\mathrm{g}_l,v'})t} \frac{1 - e^{-\mathrm{i}(E_{\mathrm{e},v} - E_{\mathrm{g}_l,v'} - \mathrm{i}\gamma_{\mathrm{c}}/2)(t-t_0)}}{E_{\mathrm{e},v} - E_{\mathrm{g}_l,v'} - \mathrm{i}\gamma_{\mathrm{c}}/2} V_{+}^{(v,lv')}.
\end{aligned}
\tag{B.22}
$$

To transform into the Schrödinger picture, $\dot{\rho}_{\mathrm{g}}^S = e^{-\mathrm{i}H_{\mathrm{g}}t}\dot{\rho}_{\mathrm{g}}e^{\mathrm{i}H_{\mathrm{g}}t} - \mathrm{i}[H_{\mathrm{g}}, \rho_{\mathrm{g}}^S]$, above integrals are rewritten as

$$I_0^S = e^{-\mathrm{i}H_{\mathrm{g}}t} I_0 e^{\mathrm{i}H_{\mathrm{g}}t} = -\mathrm{i}V_{\mathrm{gg}}^S \rho_{\mathrm{g}}^S(t_0), \tag{B.23}$$

$$I_1^S = \mathrm{i}\sum_{\substack{lvv' \\ l'u'}} V_-^{(l'u',v)} \frac{1 - e^{-\mathrm{i}(E_{\mathrm{e},v} - E_{\mathrm{g}_l,v'} - \mathrm{i}\gamma_{\mathrm{c}}/2)(t-t_0)}}{E_{\mathrm{e},v} - E_{\mathrm{g}_l,v'} - \mathrm{i}\gamma_{\mathrm{c}}/2} V_+^{(v,lv')} \rho_{\mathrm{g}}^S(t), \tag{B.24}$$

$$I_2^S = \mathrm{i}\sum_{\substack{l\neq l',vv' \\ l'\neq m',u'}} V_{\mathrm{gg}}^{(lv,l'v')} \frac{1 - e^{-\mathrm{i}(E_{\mathrm{g}_{l'},v'} - E_{\mathrm{g}_{m'},u'})(t-t_0)}}{E_{\mathrm{g}_{l'},v'} - E_{\mathrm{g}_{m'},u'}} V_{\mathrm{gg}}^{(l'v',m'u')}, \tag{B.25}$$

$$I_3^S = L_{\mathrm{eff}}^S \rho_{\mathrm{g}}^S (L_{\mathrm{eff}}^S)^\dagger, \tag{B.26}$$

where

$$L_{\mathrm{eff}}^S = -\mathrm{i}\sum_{lvv'} L_v e^{\mathrm{i}(E_{\mathrm{e},v} - E_{\mathrm{g}_1,v})t} \frac{1 - e^{-\mathrm{i}(E_{\mathrm{e},v} - E_{\mathrm{g}_l,v'} - \mathrm{i}\gamma_{\mathrm{c}}/2)t}}{E_{\mathrm{e},v} - E_{\mathrm{g}_l,v'} - \mathrm{i}\gamma_{\mathrm{c}}/2} V_+^{(v,lv')}, \tag{B.27}$$

and the master equation is given in the Schrödinger picture as

$$\dot{\rho}_{\mathrm{g}}^S = -\mathrm{i}[H_{\mathrm{g}}, \rho_{\mathrm{g}}^S] + I_0^S + I_1^S + I_2^S + (I_0^S + I_1^S + I_2^S)^\dagger + I_3^S. \tag{B.28}$$

In the case of a plasmonic nanocavity containing a molecule, we consider two electronic states for the molecule denoted as X and A. The external laser can excite the cavity mode or the electronic state so that we only consider the three states, $\{|X0\rangle, |A0\rangle, |X1\rangle\}$, where 0 and 1 represents the photon number of the cavity mode. Here, we consider only the discrete basis, where the internal degree of freedom represents the vibration, we can derive the master equation for the continuous basis in the same manner. By denoting the vibrational eigenfunctions as $|\chi_v^{\mathrm{X}}\rangle$ and $|\chi_v^{\mathrm{A}}\rangle$, the Hamiltonian and the Lindbladian are given as

$$\begin{aligned}
H = &\sum_v \omega_v^{\mathrm{X}} |X0, v\rangle \langle X0, v| + \sum_v (\omega_v^{\mathrm{A}} - \omega_L) |A0, v\rangle \langle A0, v| \\
&+ \sum_v (\omega_v^{\mathrm{X}} + \omega_{\mathrm{c}} - \omega_L) |X1, v\rangle \langle X1, v| \\
&+ \frac{\mu_{\mathrm{c}} E_0(t)}{2} \sum_v (|X1, v\rangle \langle X0, v| + |X0, v\rangle \langle X1, v|) \\
&+ \frac{\mu_{\mathrm{eg}} E_0(t)}{2} \sum_{vv'} S_{vv'} (|A0, v'\rangle \langle X0, v| + |X0, v\rangle \langle A0, v'|) \\
&+ \frac{\Omega_0}{2} \sum_{v,v'} S_{vv'} (|X1, v\rangle \langle A0, v'| + |A0, v'\rangle \langle X1, v|), \tag{B.29}
\end{aligned}$$

$$L = \sqrt{\gamma_{\mathrm{c}}} \sum_v |X0, v\rangle \langle X1, v|, \tag{B.30}$$

where $S_{vv'} = \langle \chi_v^{\mathrm{X}} | \chi_{v'}^{\mathrm{A}} \rangle$, $|X0, v\rangle = |X0\rangle |\chi_v^{\mathrm{X}}\rangle$, and $E_0(t) = E_0$ is a constant in time.

We insert $|g_1, v\rangle = |X0, v\rangle$, $|g_2, v\rangle = |A0, v\rangle$, $|e, v\rangle = |X1, v\rangle$, $E_{g_1,v} = \omega_v^X$, $E_{g_2,v} = \omega_v^A - \omega_L$, $E_{e,v} = \omega_v^X + \omega_c - \omega_L$, $g_{1v,2v'} = \mu_{eg} S_{vv'} E_0/2$, $f_{v,1v'} = \delta_{vv'} \mu_c E_0/2$, and $f_{v,2v'} = \Omega_0 S_{vv'}/2$ into Eq. (B.17), and obtain the integrals defined from Eq. (B.23) to Eq. (B.25) as

$$I_0^S = -i \frac{\mu_{eg} E_0}{2} \sum_{vv'} S_{vv'} (|X0, v\rangle \langle A0, v'| + |A0, v'\rangle \langle X0, v|) \rho_g^S(t_0), \tag{B.31}$$

$$
\begin{aligned}
I_1^S = i \Bigg[& \frac{(\mu_c E_0)^2}{4} \sum_v \frac{1 - e^{-i(\omega_c - \omega_L - i\gamma_c/2)(t-t_0)}}{\omega_c - \omega_L - i\gamma_c/2} |X0, v\rangle \langle X0, v| \\
& + \frac{\Omega_0^2}{4} \sum_{vv'u'} S_{vu'} S_{vv'} \frac{1 - e^{-i(\omega_v^X + \omega_c - \omega_{v'}^A - i\gamma_c/2)(t-t_0)}}{\omega_v^X + \omega_c - \omega_{v'}^A - i\gamma_c/2} |A0, u'\rangle \langle A0, v'| \\
& + \frac{\Omega_0 \mu_c E_0}{4} \sum_{vv'} S_{vv'} \Bigg\{ \frac{1 - e^{-i(\omega_c - \omega_L - i\gamma_c/2)(t-t_0)}}{\omega_c - \omega_L - i\gamma_c/2} |A0, v'\rangle \langle X0, v| \\
& \qquad + \frac{1 - e^{-i(\omega_v^X + \omega_c - \omega_{v'}^A - i\gamma_c/2)(t-t_0)}}{\omega_v^X + \omega_c - \omega_{v'}^A - i\gamma_c/2} |X0, v\rangle \langle A0, v'| \Bigg\} \Bigg] \rho_g^S(t), \tag{B.32}
\end{aligned}
$$

$$
\begin{aligned}
I_2^S = i \frac{\mu_{eg} E_0}{2} \sum_{vv'u'} \Bigg\{ & S_{vv'} S_{u'v'} \frac{1 - e^{-i(\omega_{v'}^A - \omega_{u'}^X - \omega_L)(t-t_0)}}{\omega_{v'}^A - \omega_{u'}^X - \omega_L} |X0, v\rangle \langle X0, u'| \\
& - S_{u'v} S_{u'v'} \frac{1 - e^{i(\omega_{v'}^A - \omega_{u'}^X - \omega_L)(t-t_0)}}{\omega_{v'}^A - \omega_{u'}^X - \omega_L} |A0, v\rangle \langle A0, v'| \Bigg\} \rho_g^S(t) \tag{B.33}
\end{aligned}
$$

and the effective Lindbladian is obtained as

$$
\begin{aligned}
L_{\text{eff}}^S = -i \sqrt{\gamma_c} e^{i(\omega_c - \omega_L)t} \Bigg[& \sum_v \frac{\mu_c E_0}{2} \frac{1 - e^{-i(\omega_c - \omega_L - i\gamma_c/2)(t-t_0)}}{\omega_c - \omega_L - i\gamma_c/2} |X0, v\rangle \langle X0, v| \\
& + \sum_{vv'} \frac{\Omega_0}{2} S_{vv'} \frac{1 - e^{-i(\omega_v^X + \omega_c - \omega_{v'}^A - i\gamma_c/2)(t-t_0)}}{\omega_v^X + \omega_c - \omega_{v'}^A - i\gamma_c/2} |X0, v\rangle \langle A0, v'| \Bigg]. \tag{B.34}
\end{aligned}
$$

The master equation in the main text Eq. (4.8) is obtained by neglecting I_0^S and I_2^S.

B.3 Derivation of the jump probability dp

Here, we give the derivation of Eqs. (4.20) and (4.23). In the continuous basis, dp can be expanded using Eq. (4.9) as

$$
dp = \mathrm{i}dt \, \langle \Psi(t)| \, (H_{\mathrm{eff}}^{\mathrm{NH}} - (H_{\mathrm{eff}}^{\mathrm{NH}})^{\dagger}) \, |\Psi(t)\rangle
$$

$$
= \mathrm{i}dt \, \langle \Psi(t)| \int dR \left[-\frac{(\mu_{\mathrm{c}} E_0)^2}{4} \left(\frac{\mathrm{i}\gamma_{\mathrm{c}} - (\omega_{\mathrm{c}} - \omega_{\mathrm{L}} + \mathrm{i}\gamma_{\mathrm{c}}/2)e^{-\mathrm{i}(\omega_{\mathrm{c}} - \omega_{\mathrm{L}} - \mathrm{i}\gamma_{\mathrm{c}}/2)(t-t_0)}}{|\omega_{\mathrm{c}} - \omega_{\mathrm{L}} - \mathrm{i}\gamma_{\mathrm{c}}/2|^2} \right. \right.
$$

$$
\left. + \frac{(\omega_{\mathrm{c}} - \omega_{\mathrm{L}} - \mathrm{i}\gamma_{\mathrm{c}}/2)e^{\mathrm{i}(\omega_{\mathrm{c}} - \omega_{\mathrm{L}} + \mathrm{i}\gamma_{\mathrm{c}}/2)(t-t_0)}}{\phantom{|\omega_{\mathrm{c}} - \omega_{\mathrm{L}} - \mathrm{i}\gamma_{\mathrm{c}}/2|^2}} \right) |\mathrm{X0}, R\rangle \langle \mathrm{X0}, R|
$$

$$
- \frac{\Omega_0^2}{4} \left(\frac{\mathrm{i}\gamma_{\mathrm{c}} - (V_{\mathrm{X}} + \omega_{\mathrm{c}} - V_{\mathrm{A}} + \mathrm{i}\gamma_{\mathrm{c}}/2)e^{-\mathrm{i}(V_{\mathrm{X}} + \omega_{\mathrm{c}} - V_{\mathrm{A}} - \mathrm{i}\gamma_{\mathrm{c}}/2)(t-t_0)}}{|V_{\mathrm{X}} + \omega_{\mathrm{c}} - V_{\mathrm{A}} - \mathrm{i}\gamma_{\mathrm{c}}/2|^2} \right.
$$

$$
\left. + \frac{(V_{\mathrm{X}} + \omega_{\mathrm{c}} - V_{\mathrm{A}} - \mathrm{i}\gamma_{\mathrm{c}}/2)e^{\mathrm{i}(V_{\mathrm{X}} + \omega_{\mathrm{c}} - V_{\mathrm{A}} + \mathrm{i}\gamma_{\mathrm{c}}/2)(t-t_0)}}{\phantom{|V_{\mathrm{X}} + \omega_{\mathrm{c}} - V_{\mathrm{A}} - \mathrm{i}\gamma_{\mathrm{c}}/2|^2}} \right) |\mathrm{A0}, R\rangle \langle \mathrm{A0}, R|
$$

$$
- \frac{\Omega_0 \mu_{\mathrm{c}} E_0}{4} \left\{ \left(\frac{V_{\mathrm{X}} - V_{\mathrm{A}} + \omega_{\mathrm{L}} + \mathrm{i}\gamma_{\mathrm{c}}}{(\omega_{\mathrm{c}} - \omega_{\mathrm{L}} - \mathrm{i}\gamma_{\mathrm{c}}/2)(V_{\mathrm{X}} + \omega_{\mathrm{c}} - V_{\mathrm{A}} + \mathrm{i}\gamma_{\mathrm{c}}/2)} \right. \right.
$$

$$
\frac{- (V_{\mathrm{X}} + \omega_{\mathrm{c}} - V_{\mathrm{A}} + \mathrm{i}\gamma_{\mathrm{c}}/2)e^{-\mathrm{i}(\omega_{\mathrm{c}} - \omega_{\mathrm{L}} - \mathrm{i}\gamma_{\mathrm{c}}/2)(t-t_0)}}{}
$$

$$
\left. + \frac{(\omega_{\mathrm{c}} - \omega_{\mathrm{L}} - \mathrm{i}\gamma_{\mathrm{c}}/2)e^{\mathrm{i}(V_{\mathrm{X}} + \omega_{\mathrm{c}} - V_{\mathrm{A}} + \mathrm{i}\gamma_{\mathrm{c}}/2)(t-t_0)}}{} \right) |\mathrm{A0}, R\rangle \langle \mathrm{X0}, R|
$$

$$
+ \left(\frac{-(V_{\mathrm{X}} - V_{\mathrm{A}} + \omega_{\mathrm{L}}) + \mathrm{i}\gamma_{\mathrm{c}}}{(\omega_{\mathrm{c}} - \omega_{\mathrm{L}} + \mathrm{i}\gamma_{\mathrm{c}}/2)(V_{\mathrm{X}} + \omega_{\mathrm{c}} - V_{\mathrm{A}} - \mathrm{i}\gamma_{\mathrm{c}}/2)} \right.
$$

$$
\frac{(V_{\mathrm{X}} + \omega_{\mathrm{c}} - V_{\mathrm{A}} - \mathrm{i}\gamma_{\mathrm{c}}/2)e^{\mathrm{i}(\omega_{\mathrm{c}} - \omega_{\mathrm{L}} + \mathrm{i}\gamma_{\mathrm{c}}/2)(t-t_0)}}{}
$$

$$
\left. \left. \left. \frac{- (\omega_{\mathrm{c}} - \omega_{\mathrm{L}} + \mathrm{i}\gamma_{\mathrm{c}}/2)e^{-\mathrm{i}(V_{\mathrm{X}} + \omega_{\mathrm{c}} - V_{\mathrm{A}} - \mathrm{i}\gamma_{\mathrm{c}}/2)(t-t_0)}}{} \right) |\mathrm{X0}, R\rangle \langle \mathrm{A0}, R| \right\} \right] |\Psi(t)\rangle .
$$

$$
\tag{B.35}
$$

All the exponential terms contain $e^{-\gamma_c(t-t_0)/2}$ and so they become negligibly small when $t - t_0 \gg 1/\gamma_c$. By omitting those terms, Eq. (B.35) becomes

$$
\begin{aligned}
dp = \mathrm{i}dt \left\langle \Psi(t) \right| \int dR &\left[-\frac{(\mu_c E_0)^2}{4} \frac{\mathrm{i}\gamma_c}{|\omega_c - \omega_L - \mathrm{i}\gamma_c/2|^2} \left| \mathrm{X0}, R \right\rangle \left\langle \mathrm{X0}, R \right| \right. \\
&- \frac{\Omega_0^2}{4} \frac{\mathrm{i}\gamma_c}{|V_X + \omega_c - V_A - \mathrm{i}\gamma_c/2|^2} \left| \mathrm{A0}, R \right\rangle \left\langle \mathrm{A0}, R \right| \\
&- \frac{\Omega_0 \mu_c E_0}{4} \left\{ \frac{V_X - V_A + \omega_L + \mathrm{i}\gamma_c}{(\omega_c - \omega_L - \mathrm{i}\gamma_c/2)(V_X + \omega_c - V_A + \mathrm{i}\gamma_c/2)} \left| \mathrm{A0}, R \right\rangle \left\langle \mathrm{X0}, R \right| \right. \\
&\left. \left. + \frac{-(V_X - V_A + \omega_L) + \mathrm{i}\gamma_c}{(\omega_c - \omega_L + \mathrm{i}\gamma_c/2)(V_X + \omega_c - V_A - \mathrm{i}\gamma_c/2)} \left| \mathrm{X0}, R \right\rangle \left\langle \mathrm{A0}, R \right| \right\} \right] \left| \Psi(t) \right\rangle \\
= dt \left\langle \Psi(t) \right| \int dR &\left[\frac{(\mu_c E_0)^2}{4} \frac{\gamma_c}{|\omega_c - \omega_L - \mathrm{i}\gamma_c/2|^2} \left| \mathrm{X0}, R \right\rangle \left\langle \mathrm{X0}, R \right| \right. \\
&\frac{\Omega_0^2}{4} \frac{\gamma_c}{|V_X + \omega_c - V_A - \mathrm{i}\gamma_c/2|^2} \left| \mathrm{A0}, R \right\rangle \left\langle \mathrm{A0}, R \right| \\
&\frac{\Omega_0 \mu_c E_0}{4} \left\{ \frac{-\mathrm{i}(V_X - V_A + \omega_L) + \gamma_c}{(\omega_c - \omega_L - \mathrm{i}\gamma_c/2)(V_X + \omega_c - V_A + \mathrm{i}\gamma_c/2)} \left| \mathrm{A0}, R \right\rangle \left\langle \mathrm{X0}, R \right| \right. \\
&\left. \left. + \frac{\mathrm{i}(V_X - V_A + \omega_L) + \gamma_c}{(\omega_c - \omega_L + \mathrm{i}\gamma_c/2)(V_X + \omega_c - V_A - \mathrm{i}\gamma_c/2)} \left| \mathrm{X0}, R \right\rangle \left\langle \mathrm{A0}, R \right| \right\} \right] \left| \Psi(t) \right\rangle .
\end{aligned}
$$
(B.36)

Finally, we insert Eq. (4.13) to obtain

$$
\begin{aligned}
dp = dt \int dR &\left[\frac{(\mu_c E_0)^2}{4} \frac{\gamma_c}{|\omega_c - \omega_L - \mathrm{i}\gamma_c/2|^2} |C_{\mathrm{X0},R}|^2 \right. \\
&+ \frac{\Omega_0^2}{4} \frac{\gamma_c}{|V_X + \omega_c - V_A - \mathrm{i}\gamma_c/2|^2} |C_{\mathrm{A0},R}|^2 \\
&\left. + \frac{\Omega_0 \mu_c E_0}{4} \left\{ \frac{-\mathrm{i}(V_X - V_A + \omega_L) + \gamma_c}{(\omega_c - \omega_L - \mathrm{i}\gamma_c/2)(V_X + \omega_c - V_A + \mathrm{i}\gamma_c/2)} C^*_{\mathrm{A0},R} C_{\mathrm{X0},R} + \mathrm{c.c.} \right\} \right] \\
= dt \int dR &\left[\frac{(\mu_c E_0)^2}{4} \frac{\gamma_c}{|\omega_c - \omega_L - \mathrm{i}\gamma_c/2|^2} |C_{\mathrm{X0},R}|^2 \right. \\
&+ \frac{\Omega_0^2}{4} \frac{\gamma_c}{|V_X + \omega_c - V_A - \mathrm{i}\gamma_c/2|^2} |C_{\mathrm{A0},R}|^2 \\
&\left. + \frac{\Omega_0 \mu_c E_0}{4} \left\{ \frac{\mathcal{R} - \mathrm{i}\mathcal{I}}{|(\omega_c - \omega_L - \mathrm{i}\gamma_c/2)(V_X + \omega_c - V_A + \mathrm{i}\gamma_c/2)|^2} C^*_{\mathrm{A0},R} C_{\mathrm{X0},R} + \mathrm{c.c.} \right\} \right] ,
\end{aligned}
$$
(B.37)

where $\mathcal{R}$ and $\mathcal{I}$ are defined as

$$
\mathcal{R} = \gamma_c \left\{ (\omega_c - \omega_L)(V_X + \omega_c - V_A) + (\gamma_c/2)^2 + (V_X - V_A + \omega_L)^2/2 \right\} \tag{B.38}
$$
$$
\mathcal{I} = \left\{ (\omega_c - \omega_L)(V_X + \omega_c - V_A) - (\gamma_c/2)^2 \right\} (V_X - V_A + \omega_L). \tag{B.39}
$$

In the discrete basis, dp is obtained in the same manner as

$$
\begin{aligned}
dp/dt =& \left(\frac{(\mu_{\mathrm{c}} E_0)^2}{4} \sum_v \frac{\gamma_{\mathrm{c}}}{|\omega_{\mathrm{c}} - \omega_{\mathrm{L}} - \mathrm{i}\gamma_{\mathrm{c}}/2|^2} \right) |C_{\mathrm{X}0,v}|^2 \\
&+ \frac{\Omega_0^2}{4} \sum_v \Bigg\{ \sum_{v'} |S_{vv'}|^2 \frac{\gamma_{\mathrm{c}}}{|\omega_v^{\mathrm{X}} + \omega_{\mathrm{c}} - \omega_{v'}^{\mathrm{A}} - \mathrm{i}\gamma_{\mathrm{c}}/2|^2} |C_{\mathrm{A}0,v'}|^2 \\
&\quad + \sum_{v' \neq u'} S_{vu'} S_{vv'} \frac{\gamma_{\mathrm{c}} - \mathrm{i}(\omega_{v'}^{\mathrm{A}} - \omega_{u'}^{\mathrm{A}})}{(\omega_v^{\mathrm{X}} + \omega_{\mathrm{c}} - \omega_{v'}^{\mathrm{A}} - \mathrm{i}\gamma_{\mathrm{c}}/2)(\omega_v^{\mathrm{X}} + \omega_{\mathrm{c}} - \omega_{u'}^{\mathrm{A}} + \mathrm{i}\gamma_{\mathrm{c}}/2)} C_{\mathrm{A}0,u'}^* C_{\mathrm{A}0,v'} \Bigg\} \\
&+ \frac{\Omega_0 \mu_{\mathrm{c}} E_0}{4} \sum_{vv'} S_{vv'} \Bigg\{ \frac{\gamma_{\mathrm{c}} - \mathrm{i}(\omega_v^{\mathrm{X}} - \omega_{v'}^{\mathrm{A}} + \omega_{\mathrm{L}})}{(\omega_{\mathrm{c}} - \omega_{\mathrm{L}} - \mathrm{i}\gamma_{\mathrm{c}}/2)(\omega_v^{\mathrm{X}} + \omega_{\mathrm{c}} - \omega_{v'}^{\mathrm{A}} + \mathrm{i}\gamma_{\mathrm{c}}/2)} C_{\mathrm{A}0,v'}^* C_{\mathrm{X}0,v} \\
&\qquad + \mathrm{c.c.} \Bigg\} \\
=& \left(\frac{(\mu_{\mathrm{c}} E_0)^2}{4} \sum_v \frac{\gamma_{\mathrm{c}}}{|\omega_{\mathrm{c}} - \omega_{\mathrm{L}} - \mathrm{i}\gamma_{\mathrm{c}}/2|^2} \right) |C_{\mathrm{X}0,v}|^2 \\
&+ \frac{\Omega_0^2}{4} \sum_v \Bigg\{ \sum_{v'} |S_{vv'}|^2 \frac{\gamma_{\mathrm{c}}}{|\omega_v^{\mathrm{X}} + \omega_{\mathrm{c}} - \omega_{v'}^{\mathrm{A}} - \mathrm{i}\gamma_{\mathrm{c}}/2|^2} |C_{\mathrm{A}0,v'}|^2 \\
&\quad + \sum_{v' \neq u'} S_{vu'} S_{vv'} \frac{\mathcal{R}_{v'u'}^{\mathrm{AA}} - \mathrm{i}\mathcal{I}_{v'u'}^{\mathrm{AA}}}{|(\omega_v^{\mathrm{X}} + \omega_{\mathrm{c}} - \omega_{v'}^{\mathrm{A}} - \mathrm{i}\gamma_{\mathrm{c}}/2)(\omega_v^{\mathrm{X}} + \omega_{\mathrm{c}} - \omega_{u'}^{\mathrm{A}} + \mathrm{i}\gamma_{\mathrm{c}}/2)|^2} C_{\mathrm{A}0,u'}^* C_{\mathrm{A}0,v'} \Bigg\} \\
&+ \frac{\Omega_0 \mu_{\mathrm{c}} E_0}{4} \sum_{vv'} S_{vv'} \Bigg\{ \frac{\mathcal{R}_{vv'}^{\mathrm{AX}} - \mathrm{i}\mathcal{I}_{vv'}^{\mathrm{AX}}}{|(\omega_{\mathrm{c}} - \omega_{\mathrm{L}} - \mathrm{i}\gamma_{\mathrm{c}}/2)(\omega_v^{\mathrm{X}} + \omega_{\mathrm{c}} - \omega_{v'}^{\mathrm{A}} + \mathrm{i}\gamma_{\mathrm{c}}/2)|^2} C_{\mathrm{A}0,v'}^* C_{\mathrm{X}0,v} \\
&\qquad + \mathrm{c.c.} \Bigg\}, \quad\quad\quad (B.40)
\end{aligned}
$$

with

$$
\mathcal{R}_{v'u'}^{\mathrm{AA}} = \gamma_{\mathrm{c}} \left\{ (\omega_v^{\mathrm{X}} + \omega_{\mathrm{c}} - \omega_{v'}^{\mathrm{A}})(\omega_v^{\mathrm{X}} + \omega_{\mathrm{c}} - \omega_{u'}^{\mathrm{A}}) + (\gamma_{\mathrm{c}}/2)^2 + (\omega_{v'}^{\mathrm{A}} - \omega_{u'}^{\mathrm{A}})^2/2 \right\}, \quad\quad (B.41)
$$

$$
\mathcal{I}_{v'u'}^{\mathrm{AA}} = \left\{ (\omega_v^{\mathrm{X}} + \omega_{\mathrm{c}} - \omega_{v'}^{\mathrm{A}})(\omega_v^{\mathrm{X}} + \omega_{\mathrm{c}} - \omega_{u'}^{\mathrm{A}}) - (\gamma_{\mathrm{c}}/2)^2 \right\} (\omega_{v'}^{\mathrm{A}} - \omega_{u'}^{\mathrm{A}}), \quad\quad (B.42)
$$

$$
\mathcal{R}_{vv'}^{\mathrm{AX}} = \gamma_{\mathrm{c}} \left\{ (\omega_{\mathrm{c}} - \omega_{\mathrm{L}})(\omega_v^{\mathrm{X}} + \omega_{\mathrm{c}} - \omega_{v'}^{\mathrm{A}}) + (\gamma_{\mathrm{c}}/2)^2 + (\omega_v^{\mathrm{X}} - \omega_{v'}^{\mathrm{A}} + \omega_{\mathrm{L}})^2/2 \right\}, \quad\quad (B.43)
$$

$$
\mathcal{I}_{vv'}^{\mathrm{AX}} = \left\{ (\omega_{\mathrm{c}} - \omega_{\mathrm{L}})(\omega_v^{\mathrm{X}} + \omega_{\mathrm{c}} - \omega_{v'}^{\mathrm{A}}) - (\gamma_{\mathrm{c}}/2)^2 \right\} (\omega_v^{\mathrm{X}} - \omega_{v'}^{\mathrm{A}} + \omega_{\mathrm{L}}). \quad\quad (B.44)
$$

Bibliography

[1] Malte C Tichy, Florian Mintert, and Andreas Buchleitner. Essential entanglement for atomic and molecular physics. *Journal of Physics B: Atomic, Molecular and Optical Physics*, 44(19):192001, oct 2011.

[2] Paolo Tommasini, Eddy Timmermans, and A. F. R. de Toledo Piza. The hydrogen atom as an entangled electron–proton system. *American Journal of Physics*, 66(10):881, dec 1998.

[3] M. V. Fedorov, M. A. Efremov, A. E. Kazakov, K. W. Chan, C. K. Law, and J. H. Eberly. Packet narrowing and quantum entanglement in photoionization and photodissociation. *Physical Review A*, 69(5):052117, may 2004.

[4] Artur F. Izmaylov and Ignacio Franco. Entanglement in the Born–Oppenheimer Approximation. *Journal of Chemical Theory and Computation*, 13(1):20–28, jan 2017.

[5] Eleftherios Goulielmakis, Zhi-Heng Loh, Adrian Wirth, Robin Santra, Nina Rohringer, Vladislav S. Yakovlev, Sergey Zherebtsov, Thomas Pfeifer, Abdallah M. Azzeer, Matthias F. Kling, Stephen R. Leone, and Ferenc Krausz. Real-time observation of valence electron motion. *Nature*, 466(7307):739–743, aug 2010.

[6] P M Kraus, B Mignolet, D Baykusheva, A Rupenyan, L Horný, E F Penka, G Grassi, O I Tolstikhin, J Schneider, F Jensen, L B Madsen, A D Bandrauk, F Remacle, and H J Wörner. Measurement and laser control of attosecond charge migration in ionized iodoacetylene. *Science (New York, N.Y.)*, 350(6262):790–5, nov 2015.

[7] Renate Pazourek, Maurizio Reduzzi, Paolo A. Carpeggiani, Giuseppe Sansone, Mette Gaarde, and Kenneth Schafer. Ionization delays in few-cycle-pulse multiphoton quantum-beat spectroscopy in helium. *Physical Review A*, 93(2):023420, feb 2016.

[8] Y. Hikosaka, T. Kaneyasu, M. Fujimoto, H. Iwayama, and M. Katoh. Coherent control in the extreme ultraviolet and attosecond regime by synchrotron radiation. *Nature Communications*, 10(1):1–5, dec 2019.

[9] Wei Chao Jiang, Xiao Min Tong, Renate Pazourek, Stefan Nagele, and Joachim Burgdörfer. Theory of bound-state coherences generated and probed by optical attosecond pulses. *Physical Review A*, 101(5):053435, may 2020.

[10] Wei Cao, Erika R. Warrick, Ashley Fidler, Stephen R. Leone, and Daniel M. Neumark. Excited-state vibronic wave-packet dynamics in H_2 probed by XUV transient four-wave mixing. *Physical Review A*, 97(2):023401, feb 2018.

[11] A Wirth, M Th Hassan, I Grguras, J Gagnon, A Moulet, T T Luu, S Pabst, R Santra, Z A Alahmed, A M Azzeer, V S Yakovlev, V Pervak, F Krausz, and E Goulielmakis. Synthesized light transients. *Science (New York, N.Y.)*, 334(6053):195–200, oct 2011.

[12] Yuki Kobayashi, Maurizio Reduzzi, Kristina F. Chang, Henry Timmers, Daniel M. Neumark, and Stephen R. Leone. Selectivity of Electronic Coherence and Attosecond Ionization Delays in Strong-Field Double Ionization. *Physical Review Letters*, 120(23):233201, jun 2018.

[13] Markus Kowalewski, Kochise Bennett, Jérémy R. Rouxel, and Shaul Mukamel. Monitoring Nonadiabatic Electron-Nuclear Dynamics in Molecules by Attosecond Streaking of Photoelectrons. *Physical Review Letters*, 117(4):043201, jul 2016.

[14] Yizhu Zhang, Tian-Min Yan, and Y.H. Jiang. Ultrafast Mapping of Coherent Dynamics and Density Matrix Reconstruction in a Terahertz-Assisted Laser Field. *Physical Review Letters*, 121(11):113201, sep 2018.

[15] Eugene P. Wigner. Lower Limit for the Energy Derivative of the Scattering Phase Shift. *Physical Review*, 98(1):145–147, apr 1955.

[16] Felix T. Smith. Lifetime Matrix in Collision Theory. *Physical Review*, 118(1):349–356, apr 1960.

[17] Renate Pazourek, Stefan Nagele, and Joachim Burgdörfer. Attosecond chronoscopy of photoemission. *Reviews of Modern Physics*, 87(3):765–802, aug 2015.

[18] J M Dahlström, A L'Huillier, and A Maquet. Introduction to attosecond delays in photoionization. *Journal of Physics B: Atomic, Molecular and Optical Physics*, 45(18):183001, sep 2012.

[19] M. Ossiander, F. Siegrist, V. Shirvanyan, R. Pazourek, A. Sommer, T. Latka, A. Guggenmos, S. Nagele, J. Feist, J. Burgdörfer, R. Kienberger, and M. Schultze. Attosecond correlation dynamics. *Nature Physics*, 13(3):280–285, nov 2016.

[20] L. Cattaneo, J. Vos, R. Y. Bello, A. Palacios, S. Heuser, L. Pedrelli, M. Lucchini, C. Cirelli, F. Martín, and U. Keller. Attosecond coupled electron and nuclear dynamics in dissociative ionization of H2. *Nature Physics*, 14:733, apr 2018.

[21] Rohit Chikkaraddy, Bart de Nijs, Felix Benz, Steven J. Barrow, Oren A. Scherman, Edina Rosta, Angela Demetriadou, Peter Fox, Ortwin Hess, and Jeremy J. Baumberg. Single-molecule strong coupling at room temperature in plasmonic nanocavities. *Nature*, 535(7610):127–130, jul 2016.

[22] Rohit Chikkaraddy, V. A. Turek, Nuttawut Kongsuwan, Felix Benz, Cloudy Carnegie, Tim van de Goor, Bart de Nijs, Angela Demetriadou, Ortwin Hess, Ulrich F. Keyser, and Jeremy J. Baumberg. Mapping Nanoscale Hotspots with Single-Molecule Emitters Assembled into Plasmonic Nanocavities Using DNA Origami. *Nano Letters*, 18(1):405–411, jan 2018.

[23] Simeon I. Bogdanov, Mikhail Y. Shalaginov, Alexei S. Lagutchev, Chin Cheng Chiang, Deesha Shah, Alexandr S. Baburin, Ilya A. Ryzhikov, Ilya A. Rodionov, Alexander V. Kildishev, Alexandra Boltasseva, and Vladimir M. Shalaev. Ultrabright Room-Temperature Sub-Nanosecond Emission from Single Nitrogen-Vacancy Centers Coupled to Nanopatch Antennas. *Nano Letters*, 18(8):4837–4844, aug 2018.

[24] Oluwafemi S. Ojambati, Rohit Chikkaraddy, William D. Deacon, Matthew Horton, Dean Kos, Vladimir A. Turek, Ulrich F. Keyser, and Jeremy J. Baumberg. Quantum electrodynamics at room temperature coupling a single vibrating molecule with a plasmonic nanocavity. *Nature Communications*, 10(1):1049, dec 2019.

[25] Simeon I. Bogdanov, Alexandra Boltasseva, and Vladimir M. Shalaev. Overcoming quantum decoherence with plasmonics, may 2019.

[26] Gilbert Grynberg, Alain Aspect, Claude Fabre, and Claude Cohen-Tannoudji. *Introduction to Quantum Optics*. 2010.

[27] Jean Dalibard, Yvan Castin, and Klaus Mølmer. Wave-function approach to dissipative processes in quantum optics. *Physical Review Letters*, 68(5):580–583, feb 1992.

[28] Takanori Nishi, Erik Lötstedt, and Kaoru Yamanouchi. Entanglement and coherence in photoionization of H_2 by an ultrashort XUV laser pulse. *Physical Review A*, 100(1):013421, jul 2019.

[29] Takanori Nishi, Erik Lötstedt, and Kaoru Yamanouchi. Time delay in the coherent vibrational motion of H_2^+ created by ionization of H_2. *Physical Review A*, 102(5):051101, nov 2020.

[30] Per-Olov Löwdin. Quantum Theory of Many-Particle Systems. I. Physical Interpretations by Means of Density Matrices, Natural Spin-Orbitals, and Convergence Problems in the Method of Configurational Interaction. *Physical Review*, 97(6):1474–1489, mar 1955.

[31] W. Kohn and L. J. Sham. Self-Consistent Equations Including Exchange and Correlation Effects. *Physical Review*, 140(4A):A1133–A1138, nov 1965.

[32] R. Car and M. Parrinello. Unified Approach for Molecular Dynamics and Density-Functional Theory. *Physical Review Letters*, 55(22):2471–2474, nov 1985.

[33] John C. Tully. Molecular dynamics with electronic transitions. *The Journal of Chemical Physics*, 93(2):1061–1071, jul 1990.

[34] E. Schrödinger. Discussion of Probability Relations between Separated Systems. *Mathematical Proceedings of the Cambridge Philosophical Society*, 31(4):555–563, oct 1935.

[35] Reinhard F. Werner. Quantum states with Einstein-Podolsky-Rosen correlations admitting a hidden-variable model. *Physical Review A*, 40(8):4277–4281, oct 1989.

[36] Asher Peres. Separability Criterion for Density Matrices. *Physical Review Letters*, 77(8):1413–1415, aug 1996.

[37] Michał Horodecki, Paweł Horodecki, and Ryszard Horodecki. Separability of mixed states: necessary and sufficient conditions. *Physics Letters A*, 223(1-2):1–8, nov 1996.

[38] C.H. Bennett, A.W. Harrow, D.W. Leung, and J.A. Smolin. On the capacities of bipartite hamiltonians and unitary gates. *IEEE Transactions on Information Theory*, 49(8):1895–1911, aug 2003.

[39] Stefan Bäuml, Siddhartha Das, and Mark M. Wilde. Fundamental Limits on the Capacities of Bipartite Quantum Interactions. *Physical Review Letters*, 121(25):250504, dec 2018.

[40] Artur Ekert and Peter L. Knight. Entangled quantum systems and the Schmidt decomposition. *American Journal of Physics*, 63(5):415–423, may 1995.

[41] Szilárd Majorosi, Mihály G. Benedict, and Attila Czirják. Quantum entanglement in strong-field ionization. *Physical Review A*, 96(4):043412, oct 2017.

[42] Zhen Huang and Sabre Kais. Entanglement as measure of electron–electron correlation in quantum chemistry calculations. *Chemical Physics Letters*, 413(1-3):1–5, sep 2005.

[43] Z. Huang, H. Wang, and S. Kais. Entanglement and electron correlation in quantum chemistry calculations. *Journal of Modern Optics*, 53(16-17):2543–2558, nov 2006.

[44] Laura K McKemmish, Ross H McKenzie, Noel S Hush, and Jeffrey R Reimers. Quantum entanglement between electronic and vibrational degrees of freedom in molecules. *The Journal of chemical physics*, 135(24):244110, dec 2011.

[45] José Luis Sanz-Vicario, Jhon Fredy Pérez-Torres, and Germán Moreno-Polo. Electronic-nuclear entanglement in H_2^+: Schmidt decomposition of non-Born-Oppenheimer wave functions expanded in nonorthogonal basis sets. *Physical Review A*, 96(2):022503, aug 2017.

[46] Yuanyuan Cheng and Liangjun Zhai. Dynamics of bipartite vibrational entanglement under the inherent decoherence process in H_2O. *J. At. Mol. Sci*, 7(4):213–224, 2016.

[47] Nina Rohringer and Robin Santra. Multichannel coherence in strong-field ionization. *Physical Review A*, 79(5):053402, may 2009.

[48] Stefanos Carlström, Johan Mauritsson, Kenneth J Schafer, Anne L'Huillier, and Mathieu Gisselbrecht. Quantum coherence in photo-ionisation with tailored XUV pulses. *Journal of Physics B: Atomic, Molecular and Optical Physics*, 51(1):015201, jan 2018.

[49] Mihaela Vatasescu. Entanglement between electronic and vibrational degrees of freedom in a laser-driven molecular system. *Physical Review A*, 88(6):063415, dec 2013.

[50] Mihaela Vatasescu. Measures of electronic-vibrational entanglement and quantum coherence in a molecular system. *Physical Review A*, 92(4):042323, oct 2015.

[51] John Schliemann, J. Ignacio Cirac, Marek Kuś, Maciej Lewenstein, and Daniel Loss. Quantum correlations in two-fermion systems. *Physical Review A*, 64(2):022303, jul 2001.

[52] G. C Ghirardi and L. Marinatto. Entanglement and properties. *Fortschritte der Physik*, 51(45):379–387, may 2003.

[53] Gian Carlo Ghirardi and Luca Marinatto. General criterion for the entanglement of two indistinguishable particles. *Physical Review A*, 70(1):012109, jul 2004.

[54] Paolo Zanardi. Virtual Quantum Subsystems. *Physical Review Letters*, 87(7):077901, jul 2001.

[55] F Herbut and M Vujičić. Irrelevance of the Pauli principle in distant correlations between identical fermions. *Journal of Physics A: Mathematical and General*, 20(16):5555–5563, nov 1987.

[56] Fedor Herbut. How to distinguish identical particles. *American Journal of Physics*, 69(2):207–217, feb 2001.

[57] Toshihiko Sasaki, Tsubasa Ichikawa, and Izumi Tsutsui. Entanglement of indistinguishable particles. *Physical Review A*, 83(1):012113, jan 2011.

[58] V. Vedral and M. B. Plenio. Entanglement measures and purification procedures. *Physical Review A*, 57(3):1619–1633, mar 1998.

[59] Guifré Vidal. Entanglement monotones. *Journal of Modern Optics*, 47-2(3):355–376, 2000.

[60] Gregg. Jaeger. *Quantum Information.* Springer, New York, NY, 2007.

[61] Charles H. Bennett, Herbert J. Bernstein, Sandu Popescu, and Benjamin Schumacher. Concentrating partial entanglement by local operations. *Physical Review A*, 53(4):2046–2052, apr 1996.

[62] Shunlong Luo. Using measurement-induced disturbance to characterize correlations as classical or quantum. *Physical Review A*, 77(2):022301, feb 2008.

[63] Manfred Lein, Thomas Kreibich, E. K. U. Gross, and Volker Engel. Strong-field ionization dynamics of a model H_2 molecule. *Physical Review A*, 65(3):033403, feb 2002.

[64] T E Sharp. Potential-energy curves for molecular hydrogen and its ions. *Atomic Data and Nuclear Data Tables*, 2:119–169, 1970.

[65] J. Rapp and D. Bauer. Effects of inner electrons on atomic strong-field-ionization dynamics. *Physical Review A*, 89(3):033401, mar 2014.

[66] R. Kosloff and H. Tal-Ezer. A direct relaxation method for calculating eigenfunctions and eigenvalues of the Schrödinger equation on a grid. *Chemical Physics Letters*, 127(3):223–230, jun 1986.

[67] R. Kosloff and D. Kosloff. Absorbing boundaries for wave propagation problems. *Journal of Computational Physics*, 63(2):363–376, apr 1986.

[68] J. A. Fleck, J. R. Morris, and M. D. Feit. Time-dependent propagation of high energy laser beams through the atmosphere. *Applied Physics*, 10(2):129–160, jun 1976.

[69] M.D. Feit, J.A. Fleck, and A. Steiger. Solution of the Schrödinger equation by a spectral method. *Journal of Computational Physics*, 47(3):412–433, sep 1982.

[70] D Kosloff and R Kosloff. A Fourier method solution for the time dependent Schrödinger equation as a tool in molecular dynamics. *Journal of Computational Physics*, 52(1):35–53, oct 1983.

[71] Yasuo Nabekawa, Yusuke Furukawa, Tomoya Okino, A Amani Eilanlou, Eiji J Takahashi, Kaoru Yamanouchi, and Katsumi Midorikawa. Settling time of a vibrational wavepacket in ionization. *Nature communications*, 6:8197, sep 2015.

[72] Yasuo Nabekawa, Yusuke Furukawa, Tomoya Okino, A Amani. Eilanlou, Eiji J. Takahashi, Kaoru Yamanouchi, and Katsumi Midorikawa. Frequency-resolved optical gating technique for retrieving the amplitude of a vibrational wavepacket. *Scientific Reports*, 5(1):11366, sep 2015.

[73] L. D. Landau and E. M. Lifshitz. *Quantum Mechanics : Non-Relativistic Theory.* Elsevier Science, 1977.

[74] Stefan Pabst, Loren Greenman, Phay J. Ho, David A. Mazziotti, and Robin Santra. Decoherence in Attosecond Photoionization. *Physical Review Letters*, 106(5):053003, feb 2011.

[75] Caroline Arnold, Oriol Vendrell, and Robin Santra. Electronic decoherence following photoionization: Full quantum-dynamical treatment of the influence of nuclear motion. *Physical Review A*, 95(3):033425, mar 2017.

[76] M Schultze, M Fiess, N Karpowicz, J Gagnon, M Korbman, M Hofstetter, S Neppl, A L Cavalieri, Y Komninos, Th Mercouris, C A Nicolaides, R Pazourek, S Nagele, J Feist, J Burgdörfer, A M Azzeer, R Ernstorfer, R Kienberger, U Kleineberg, E Goulielmakis, F Krausz, and V S Yakovlev. Delay in photoemission. *Science (New York, N.Y.)*, 328(5986):1658–62, jun 2010.

[77] K. Klünder, J. M. Dahlström, M. Gisselbrecht, T. Fordell, M. Swoboda, D. Guénot, P. Johnsson, J. Caillat, J. Mauritsson, A. Maquet, R. Taïeb, and A. L'Huillier. Probing Single-Photon Ionization on the Attosecond Time Scale. *Physical Review Letters*, 106(14):143002, apr 2011.

[78] M Isinger, R J Squibb, D Busto, S Zhong, A Harth, D Kroon, S Nandi, C L Arnold, M Miranda, J M Dahlström, E Lindroth, R Feifel, M Gisselbrecht, and A L'Huillier. Photoionization in the time and frequency domain. *Science (New York, N.Y.)*, 358(6365):893–896, nov 2017.

[79] J Vos, L Cattaneo, S Patchkovskii, T Zimmermann, C Cirelli, M Lucchini, A Kheifets, A S Landsman, and U Keller. Orientation-dependent stereo Wigner time delay and electron localization in a small molecule. *Science (New York, N.Y.)*, 360(6395):1326–1330, jun 2018.

[80] Vladislav V. Serov, Boghos B. Joulakian, Dmitry V. Pavlov, Igor V. Puzynin, and Sergue I. Vinitsky. (e, 2e) ionization of H_2^+ by fast electron impact: Application of the exact nonrelativistic two-center continuum wave. *Physical Review A*, 65(6):062708, jun 2002.

[81] G Sansone, E Benedetti, F Calegari, C Vozzi, L Avaldi, R Flammini, L Poletto, P Villoresi, C Altucci, R Velotta, S Stagira, S De Silvestri, and M Nisoli. Isolated single-cycle attosecond pulses. *Science (New York, N.Y.)*, 314(5798):443–6, oct 2006.

[82] Daqing Wang, Hrishikesh Kelkar, Diego Martin-Cano, Dominik Rattenbacher, Alexey Shkarin, Tobias Utikal, Stephan Götzinger, and Vahid Sandoghdar. Turning a molecule into a coherent two-level quantum system. *Nature Physics*, 15(5), 2019.

[83] Christian Schäfer, Michael Ruggenthaler, and Angel Rubio. *Ab initio* nonrelativistic quantum electrodynamics: Bridging quantum chemistry and quantum optics from weak to strong coupling. *Physical Review A*, 98(4):043801, oct 2018.

[84] David M. Coles, Niccolo Somaschi, Paolo Michetti, Caspar Clark, Pavlos G. Lagoudakis, Pavlos G. Savvidis, and David G. Lidzey. Polariton-mediated energy transfer between organic dyes in a strongly coupled optical microcavity. *Nature Materials*, 13(7):712–719, jul 2014.

[85] Oriol Vendrell. Collective Jahn-Teller Interactions through Light-Matter Coupling in a Cavity. *Physical Review Letters*, 121(25):253001, dec 2018.

[86] R. E. F. Silva, Javier del Pino, Francisco J. García-Vidal, and Johannes Feist. Polaritonic molecular clock for all-optical ultrafast imaging of wavepacket dynamics without probe pulses. *Nature Communications*, 11(1):1423, dec 2020.

[87] Florentin Reiter and Anders S. Sørensen. Effective operator formalism for open quantum systems. *Physical Review A*, 85(3):032111, mar 2012.

[88] Henriette Astrup Leth, Lars Bojer Madsen, and Klaus Mølmer. Monte Carlo Wave Packet Theory of Dissociative Double Ionization. *Physical Review Letters*, 103(18):183601, oct 2009.

[89] Giulia Dall'Osto, Emanuele Coccia, Ciro A. Guido, and Stefano Corni. Investigating ultrafast two-pulse experiments on single DNQDI fluorophores: A stochastic quantum approach. *Physical Chemistry Chemical Physics*, 22(29):16734–16746, aug 2020.

[90] Yvan Castin and Klaus Mølmer. Monte Carlo Wave-Function Analysis of 3D Optical Molasses. *Physical Review Letters*, 74(19):3772–3775, may 1995.

[91] M Hatridge, S Shankar, M Mirrahimi, F Schackert, K Geerlings, T Brecht, K M Sliwa, B Abdo, L Frunzio, S M Girvin, R J Schoelkopf, and M H Devoret. Quantum back-action of an individual variable-strength measurement. *Science (New York, N.Y.)*, 339(6116):178–81, jan 2013.

[92] C. W. Gardiner, A. S. Parkins, and P. Zoller. Wave-function quantum stochastic differential equations and quantum-jump simulation methods. *Physical Review A*, 46(7), 1992.

[93] P. Haikka and K. Mølmer. Dissipative Landau-Zener level crossing subject to continuous measurement: Excitation despite decay. *Physical Review A*, 89(5):052114, may 2014.

[94] L.I. Ponomarev and L.N. Somov. The wave functions of continuum for the two-center problem in quantum mechanics. *Journal of Computational Physics*, 20(2):183–195, feb 1976.

[95] G. Breit and H. A. Bethe. Ingoing Waves in Final State of Scattering Problems. *Physical Review*, 93(4):888–890, feb 1954.

[96] S. Altshuler. Ingoing waves in the final state of ionization problems. *Il Nuovo Cimento*, 3(2):246–251, feb 1956.